December 2018

In Silico Analysis of Advanced Processing Methods for Light-weight Alloys Powders

Marjan Nezafati
University of Wisconsin-Milwaukee

In silico analysis of advanced processing methods for light-weight alloys powders

by

Marjan Nezafati

A Dissertation Submitted in

Partial Fulfillment of the

Requirements for the Degree of

Doctor of Philosophy

in Engineering

at

The University of Wisconsin–Milwaukee

December 2018

Abstract

In silico analysis of advanced processing methods for light-weight alloys powders

by
Marjan Nezafati

The University of Wisconsin–Milwaukee, 2018
Under the Supervision of Doctor Benjamin Church

Light-weight Al and Mg-based metal-matrix nanocomposites (MMNCs) are lauded as one of the most promising structural materials for vehicle, military, and construction applications. These MMNCs are often synthesized using the powder metallurgy (PM) process under liquid nitrogen cryogenic environments to control the grain sizes. It is believed that proper incorporation of the nitrogen species into the bulk lattice during processing could strongly enhance the mechanical properties of MMNCs by forming N-rich dispersoids. In this work, using the density-functional theory (DFT), the adsorption, absorption and diffusion behavior of nitrogen molecule/atoms have been studied and related to t Al and Mg MMNC PM processing. The study includes the impacts of binding sites, alloying elements (Al, Zn, and Y in Mg and Mg, Mn and Fe for Al), and surface crystallographic planes on the nitrogen molecule adsorption energies. The transition state (TS) behaviors for the bond breaking and lattice diffusion of nitrogen were examined. The results show that in presence of Mg (0001) or Al (111) surfaces, dissociation of N_2 to N atoms requires 1/9 to 1/5 of the isolated state energy , respectively.

As a critical issue limiting the application of Mg-based MMNCs, the degradation (corrosion) of Mg alloys in aqueous media was modeled in this work. It is known that both the internal crystal structures and the impurity compositions/contents in the Mg alloys can affect the degradation rates. Density-functional theory (DFT) computation was utilized to understand the surface degradation behaviors with different crystallographic orientations and impurity elements from an atomistic standpoint. The adsorption response of the Mg alloy surface to the water molecule and the dissolution of surface atoms were studied to describe the degradation behavior of Mg and Mg

alloys. The tendency for water molecule adsorption was quantified for Mg-based slab systems with low-index surface planes and various alloying elements including Al, Zn, Ca, and Y. The trends for surface degradation from these systems were examined using surface energy analysis and electrode potential shift analysis. The results showed that adding Ca and/or Y increases the propensity to attract a water molecule to the alloy surface. Also, it was generally found that the relative electrode potential shift of Mg-Y alloys is positive while those of all other alloys are negative. After having a comprehensive understanding about the atomistic behavior of metal powder in contact with the cryomilling media, the consolidation process was analyzed, including the melting and resolidification of powder through selective laser melting. At this stage of the work the concerns were to achieve the maximum connectivity between the powder layers after resolidification and to avoid extreme superheat. Since the efficiency of the MMNCs strongly relies on homogeneous distribution of reinforcement particles the SLM process was optimized to avoid any clustering of the reinforcement particles.

Focusing on consolidation of MMNCS, Al10SiMg/AlN with weight ratio of 99:1 was chosen. AlSi10Mg with 10% Si and 0.5% Mg is one the most convenient compositions among the light weight alloys for laser melting processes, due to its narrow solidification range, that provides sufficient fluidity to produce sound products. Also, as the powder had been prepared via cryomilling process, the presence of AlN particles was proven based on the DFT calculations and experimental evidence described earlier. The laser power, scanning velocity and initial temperature of the powder were selected as the most important factors affecting the melting and solidification of the alloy powder. Finite volume analysis and experimental design were applied to optimize the SLM processing condition. Finite volume method was used to estimate the melt pool geometry, temperature profile of the part and velocity of solidification front. This information is necessary to produce strong parts with homogeneous properties all over the specimen, minimize energy consumption and avoid formation of defects in the sample. It was confirmed that even in the most extreme conditions the maximum temperature during the process would not exceed 1710K, which is roughly 460K below the melting temperature of the AlN reinforcement particles. The laser speed and power have significant effect on the melt pool geometry and maximum temperature of melt pool while the effect of initial powder temperature was insignificant for both of the response values. The AlN reinforcement particles are expected to have a homogeneous

distribution since the velocity of the solidification front is higher than the critical calculated value of 5900 μ m/s. Results also showed that the solidification front velocity depends on the laser speed and the effects of laser power and initial temperature are insignificant.

This work provides a comprehensive multiscale computational model tracking the Al and Mg based light-weight alloys from powder preparation stage to shaping the final product that considers potential gaps with focus on solidification process. These findings are particularly important to eliminate the extra processing steps to save time, energy and material maintaining the high quality of the final product.

To My Family and Friends

Table of Contents

List of Figures

List of Tables

Acknowledgements

There are many people that have supported me during my path in graduate school and I am pleased to express my gratitude for their contributions and supports. First and foremost, I want to thank my PhD advisor and mentor Dr. Benjamin Church for believing in me and encouraging me in all the difficult moments. Besides scientific contributions and discussions Dr. Church has taught me how caring and being ready to help others provides me opportunities to grow and learn. I am also grateful for my PhD committee members Dr. Pradeep Rohatgi, Dr. Hugo Lopez, Dr. Ilya Avdeev, Dr. Mathew Petering and Dr. Benjamin Schultz for always being ready to guide me and provide valuable comments and suggestions to improve my work.

I also would like to use this opportunity to thank Dr. Changsoo Kim for his helps and contributions to this work. And to all of those who I had the privilege to work with. I thank Dr. Anit Giri for valuable suggestions and encouragements and Dr. Ali Bakhshinejad for supporting me in my CFD calculations and being always ready to answer my questions.

And at the end, I appreciate my family and friends, for being there for me and encouraging me through my journey, especially my brother who has always inspired me.

Chapter 1

Scope and future plan

1.1 Motivation

Nanocrystalline alloys have always been the center of attention for their intensified mechanical strength. In light weight alloys such as Al and Mg based alloys, the strength is combined with light weight and enhances the energy consumption, specifically in aerospace and automobile industries. Although high strength to weight ratio of Al and Mg alloys makes them great competent for the traditional structural materials such as stainless steel and titanium alloys, there are some properties that limit the application of these materials in some industries. For instance, the plasticity of Mg metal with Hexagonal Closed Packed (HCP) structure is influenced by the small c/a ratio. The ideal value for c/a ratio in closed pack structures is 1.632. Considering the lattice constants of Mg crystal where a=0.3202nm and c=0.5199nm, the Mg unit cell is relatively compressed along the c axis with the c/a ratio equal to 1.624. This compression in the lattice causes poor ductility in the metal. Moreover, the tensile strength of pure Mg is insufficient for many applications, which needs enhancement by applying reinforcement agents, varying the composition or modifying the processing method. As a further matter in some applications that corrosive media or humidity are involved Mg suffers from fast corrosion rate.

Although Al has reasonable strength for most of the applications, and only changing the composition and addition of alloying elements can enhance the mechanical properties of pure Al, Al based nano composites provide comparable mechanical behavior to those of stainless steel, with much lower processing temperatures and considerably lower density.

In polycrystalline alloys, the strength depends directly to the motion of dislocations through the material. Adding microstructural obstacles to the alloy, limits the movement of dislocations and improves the strength of the alloy. Solid solution strengthening, precipitation hardening, and grain refinement are some methods to tailor the mechanical properties of the alloy. To elevate the mechanical strength of the alloy through the processing stage and with minimum cost it is essential to choose the convenient strengthening mechanism through the appropriate processing method and track all the interactions during each of the processing steps.

1.2 Research Problems and Suggested Plans

As it was discussed earlier, producing light weight alloys with desired properties has always been an ultimate objective in transportation industry. While maintaining the safety and performance, it is ideal to reduce the weight of vehicles, to minimize fuel consumption.

Considering the weight reduction without sacrifying the performance as the main target, we first focused on the effect of composition and processing, considering cryomilling as the processing method to reach the desired grain structure. Due to the cryogenic environment it also provides some protection for the alloy powder against oxidation, this can be beneficial specifically for Mg based powders. Also providing liquid nitrogen to the powder brings the idea of nitride formation to the mind. If the nitrogen molecules find a chance to penetrate to the metal structure and form some nitrogen-rich particles, depending on the distribution of these particles, there is a chance for activating Orowan strengthening mechanism in the alloy. Although experimental efforts have been made to detect the presence of nitrogen and nitrogen-rich particles in bulk alloy, it is really difficult to explain the adsorption, absorption and diffusion mechanisms without having an atomistic model of the system. To have a better understanding of the metal-nitrogen interactions, both on the surface and inside the bulk, we have provided some atomistic models, simulating the behavior of Al and Mg based powders in contact with liquid nitrogen in this work. Surface interactions including adsorption and absorption were carefully analyzed. The energy barriers for surface and bulk diffusion were compared at different circumstances, including composition and crystallographic orientation of the surface in contact with the cryogenic atmosphere.

Another critical challenge when dealing with Mg-based alloys, is the reactivity of Mg and

high tendency for corrosion in aqueous or even humid atmospheres. It is known that both the internal crystal structures and the impurity compositions/contents in the Mg alloys can affect the degradation rates. In spite of experiments that have attempted to test the corrosion behavior of Mg alloys, a comprehensive atomistic model that simulates the behavior of Mg alloys in corrosive media has always been missing. Such model not only has a closer look at the process, but also reduces the financial cost and environmental pollution.

After having an understanding about the atomistic behavior of metal powder in contact with the processing media, we attempted to analyze the consolidation process, including the melting and resolidification of powder through selective laser melting as well. At this stage of the work our concerns were the connectivity of the powder layers after resolidification, and to avoid extrem superheat that casues melting or decomposition of the reinforcement particles along with prohibiting particle pushing by the solidification front and agglomeration of the reinforcement agents to ensure that the distribution of the particles is homogeneous in the system.

Al10SiMg/AlN composite with a weight ratio of 99:1 was studied as the most convenient composition among the light weight alloys. AlSi10Mg is a close to eutectic composition and due to its narrow solidification range provides sensible fluidity to produce sound products. Considering the laser power and scanning velocity and initial temperature as the parameters influencing the melting and solidification of the alloy powder. In this work we applied finite volume method (FVM) to choose the appropriate processing condition. FVM was used to predict the melt pool geometry, thermal gradient and solidification front velocity in producing parts through SLM process. This information is necessary to produce strong parts with homogeneous properties all over the specimen, minimize the energy consumption and avoid defects formation in the sample.

1.3 Scope of this Work

In chapter 2 we discussed some introduction on possible processing techniques and literature review related to the research background. This chapter covers 1) nano powder processing methods 2)microstructure of nanocrystalline alloys 3)mechanical properties of nanocrystalline alloys 4)corrosion behavior of Mg alloys.

Chapter 3 covers a brief introduction on DFT theory and the computational methods used in

this study. In this chapter we explain some essential terminology required for this work and discuss the detailed computational parameters used in our calculations.

Considering the corrent state of knowledge and the shortcomings in the existing research steams, chapter 4 has been organized in aim of presenting the atomistic modeling and specifically *ab initio* calculations, focuses on the interaction of the metal powder with the processing environment. Possibility of nitride formation has been studied in this chapter and as a limiting factor for application of Mg alloys their corrosion resistance in aqueous media has been analyzed. This chapter also analyzes the selective laser melting of AlSi10Mg/AlN composite and targets optimizing the process to obtain the final product with improved properties and free of defects.

In chapter 5 we summerized all the results from chapter 4.

Chapter 2

Introduction

Nanocrystalline metals that have grain sizes less than 100nm demonstrate a considerably higher strength compared to those of coarse-grained structures with similar compositions or even alloyed ones [15]. These structural nanomaterials, specially with light metal bases, such as aluminum (Al) and magnesium (Mg) are finding applications in bulk materials, films and composites. In the past few years Al and Mg based nano alloys have found their path to a wide range of structural applications. The progress of nanomaterials field relies on developing new synthesis methods and processing techniques, as well as, fundamental understanding of the powder behavior in contact with processing atmosphere and consolidation product properties. To enhance the mechanical behavior of the final product, it is crucial to keep track of all the interactions between the powder and environment from the early stages of powder preparation to sintering and consolidation. Considering the importance of these interactions, this work has been organized in following sections:

- Motivations, objective and current status of this work (Chapter 1).
- A brief introduction and literature review on: Al and Mg based nanoalloys and metal matrix nanocomposites, nanopowders processing methods, the consequential microstructures and mechanical behaviors (Chapter 2).
- Research methods, consisting of computational modeling details and a brief explanation on terminology used in this work (Chapter 3).
- Results on powder-environment interaction, reinforcement particle formation and selective

laser melting (Chapter 4).

- Summary and conclusions (Chapters 5)

2.1 Processing: powder metallurgy (PM) technique for the synthesis of nanocrystalline alloys

Powder metallurgy (PM) as a common synthesizing method for near net component can compete with the traditional casting and forming methods. PM which covers a wide range of processing methods consists of three principal steps including powder preparation, compression and sintering. The structure and the particle size in the final product can be influenced by each of these steps but is mostly controlled during powder preparation and sintering processes.

2.1.1 Synthesis

There are two main approaches for synthesizing the nanocrystalline materials, bottom-up and top-down methods. The bottom-up methods include methods that arrange the nanostructure atom by atom and layer by layer. On the contrary side top-down methods start with the bulk material and break down the microstructure into a nanosized structure. Some of the common synthesizing methods for preparing nano powder for powder metallurgy process include [16]

- gas condensation
- vacuum deposition and vaporization
- chemical vapor deposition (CVD) and chemical vapor condensation (CVC)
- mechanical attrition
  - attrition ball mill
  - planetary ball mill
  - vibrating ball mill
  - low energy tumbling mill
  - high energy tumbling mill

- chemical precipitation
- sol-gel techniques
  - hydrolysis
  - condensation
  - growth of particles
  - agglomeration of particles
- electrodeposition

Each of these methods provide advantages and disadvantages for nano size particle preparation. For instance, the gas condensation method suffers from extreme slow rate, a source-precursor incompatibility, temperature ranges and dissimilar evaporation rates in an alloy. The vacuum deposition processes have the advantage of high deposition rates and low cost but deposition of a large number of compounds is difficult. Mechanical attrition produces the nanostructures not by cluster assembly (as most of the mentioned methods do) but by the structural decomposition of coarser grained structure due to plastic deformation. Some of the most common methods will be discussed in this section.

Inert gas condensation

Condensation of the evaporated metal in an inert gas atmosphere was a method developed by Gleiter [17]. The process takes place inside a evacuated chamber to a very high vacuum of about 10^{-7} Torr and then backfilled with a low pressure inert gas such as helium. In this process the metal vapor collides with the inert gas atoms inside the chamber and condense to small sized particles as a result of losing their kinetic energy. There are wide range of methods to prepare the metal powder including resistive heating, radio-frequency, sputtering, electron beam heating and laser/plasma heating). The collector device stores the condensed fine powders transferred to it through liquid-nitrogen filled collection device. The powder is scraped off into the compaction device which compacts the powders in two steps (1) low pressure compacted pellet and (2) high pressure vacuum compaction and under ultrahigh vacuum conditions to avoid chemical reactions

on the powder surface and minimize the amount of the trapped gas in the powder. In spite of equiaxed powder shape and the narrow range of size distribution this method has some drawbacks including possibility of imperfect bonding between particles and also contamination of powders and porosity due to insufficient consolidation [18, 19].

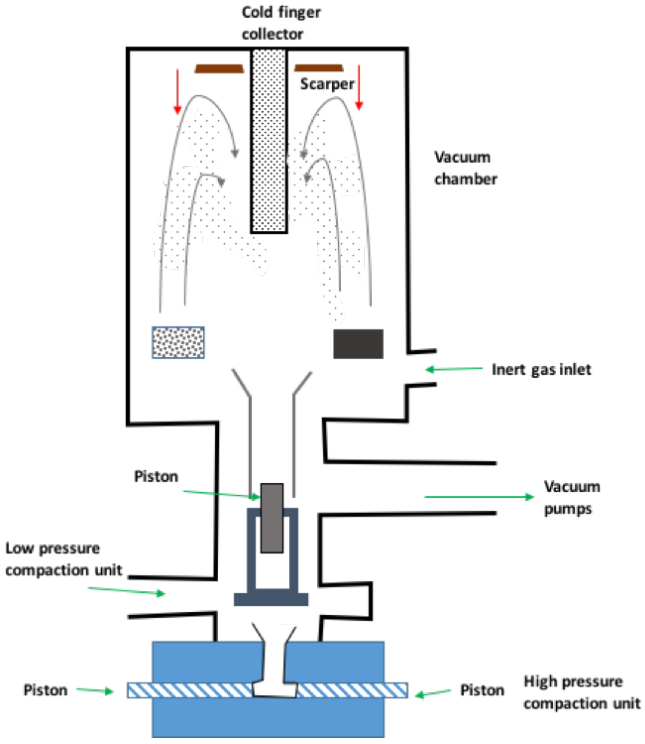

Figure 2.1: Schematic of inert gas condensation method

Nanocrystalline powders by chemical reactions

Taking advantage of chemical reactions for synthesizing nanopowders provides a homogeneous chemical composition for the produced powder resulting in some improved mechanical properties for the final product. This method can be scaled up for bulk production of nanoparticle sized metals, oxides, intermetallics, semiconductors and glasses [18, 20]. As an example, nanocrystals of Mo can be produced from reduction of $MoCl_3$ using toluene as an organic solution and $NaBEt_3H$ as reducing agent at room temperature.

$$MoCl_3 + 3NaBEt_3H \longrightarrow Mo + 3NaCl + 3BEt_3 + (3/2)H_2 \tag{2.1}$$

aluminum nanoparticles can be also produced by the similar method, that decomposes $Me_2EtNAlH_3$ where Me stands for methyl or CH_3, the decomposition process takes place in toluene heated to $110°C$ for 2 hours. The challenges associated with the chemical fabrication of nanostructures include contamination and severe agglomeration in the chemical baths which causes trouble in consolidating the nanoparticles in fully dense components. Two common methods of chemical synthesis of nanopowders are (1) sol-gel and (2) microemulsion. Both of these methods are colloidal methods which are well stablished wet chemistry precipitation with solution of different ions under controlled temperature and pressure to form insoluble precipitates.

Sol-gel technique consists of two main parts, the sol is the colloidal solution made of solid particles which are few hundreds in diameter and suspended in a liquid phase. The gel is a solid macromolecule immersed in a solvent. The basic steps of the sol-gel method are shown in Figure 2.2. These two steps are also referred to as hydrolysis and condensation of alkoxide-based precursors like tetraethyl orthosilicate $(Si(OEt)_4)$ as well.

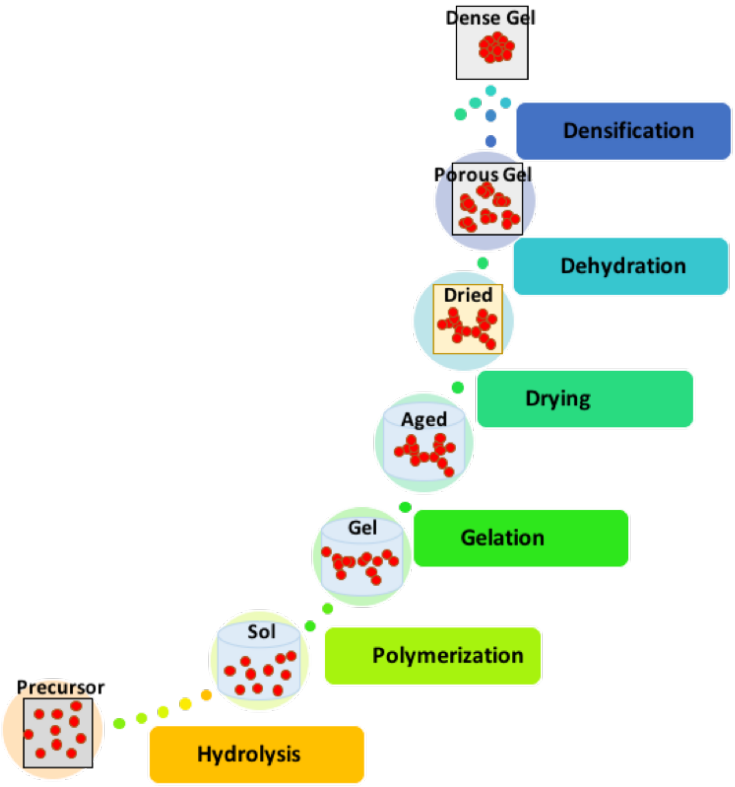

Figure 2.2: Schematic sequences of the Sol-gel process

The sol-gel process in general includes the formation of stable solutions of the alkoxide or sol-

vated metal precursor (the sol), gelation due to formation of oxide- or alcohol- bridged network (the gel) (at this step viscosity increases considerably), aging of the gel which consists of polycondensation reactions resulting in a solid mass, drying of the gel by removing water or any other volatile liquid from the gel network, dehydration or removing of the surface- bond M-OH groups to avoid rehydration and densification and decomposition of the gel at high temperature (more than $800°C$).

An example of the hydrolysis and condensation of metal alkoxides $M(OR)_z$ can be described as:

$$MOR + H_2O \longrightarrow MOH + ROH(hydrolysis) \tag{2.2}$$

$$MOH + ROM \longrightarrow M - O - M + ROH(condensation) \tag{2.3}$$

In microemulsion method [21, 22] uses isotropic, macroscopically homogeneous, and thermodynamically stable solutions of a polar phase (usually water), a nonpolar phase (usually oil) and a surfactant (molecules to form an interfacial film separating the polar and the non-polar phases) to synthesis nanoparticles. The interfacial layer produced due to the interaction of these three phases can take the form of different microstructures from droplets of oil dispersed in a continuous water phase known as O/W-microemulsion to water droplets dispersed in a continuous oil phase known as W/O-microemulsion. The intermediate state is a bi-continuous sponge phase. The proportion of various components and the hydrophilic-lipophilic balance of the surfactant present in the microemulsion the microdroplet shape switches from oil-swollen micelles dispersed in water as oil-in-water (O/W) microemulsion or water swollen micelle dispersed in oil as for water-in-oil (W/O) microemulsion, also known as reverse microemulsion. Either of these nanodroplets can function as nanoreactors for the chemical reactions to produce nanoparticles.

Mechanical attrition methods

Ball milling of powders or mechanical attrition usually is applied in two main categories of nanopowder processing. (1) the milling of elemental or compound powders known as mechanical milling with the purpose of producing finer powder size or even nanostructured materials. Cryomilling will

be discussed as an example of these processes in the following section. (2) This method which is known as mechanical alloying takes advantage of milling process to produce new alloys by mixing dissimilar powders.

Cryomilling

Among all the powder preparation techniques cryomilling has been chosen to be studied in this work as a convenient production method specifically for more reactive alloys such as Al and Mg based alloys with high tendency for oxidation. Cryomilling as a mechanical attrition method in which powders are milled in a slurry formed with milling balls and cryogenic liquid, usually liquid nitrogen, provides a suitable atmosphere for obtaining nano sized grain structure [23]. Use of liquid nitrogen in mechanical alloying took place at Exxon Research and Engineering for the first time and resulted in the shorter milling time for achieving fine particle size and smaller recrystallized grain sizes when compared to mechanical alloying performed in air or in Ar [24]. The first cryomilling research focused on $Al - Al_2O_3$ composite and aimed to understand the dispersion-strengthening mechanism [25]. Although the initial goal was to enhance the strength and creep resistance of Al composites by dispersion and only for a specific temperature range more recent researches concentrate on the nanostructure character of cryomilled bulk Al alloys for grain size refinement and strengthening [26].

Despite of the wide range of attempts to enhance the mechanical properties of Al alloys the strengthening behavior of such alloys seems to be complicated. Maung et al. [8] showed that the strength of the reinforced Al samples is consistently lower than that of cryomilled samples with no diamantine reinforcements. On the other hand, the ductility of the reinforced sample is three to fourfold higher than that of the non-reinforced sample. The reason for such behavior is that, when the grain size of some nano crystalline materials falls below a critical value in the nanoscale range, nanoscale softening or inverse Hall-Petch effect occurs. They mentioned that multiple processes including Coble creep. The absence of dislocation pile-up, the operation of Coble creep and a threshold stress, the operation of a stress-assisted thermally activated process in the boundary and the application of a composite model are responsible for the inverse Hall-Petch operate to cause nanoscale softening. A steeper slope for conventional Hall-Petch equation for Al compared to Ni and also the smaller activation energy for grain boundary diffusion of Al versus Ni are known to

be responsible for the larger critical grain size of Al than that of Ni (110nm for Al versus 15nm for Ni).

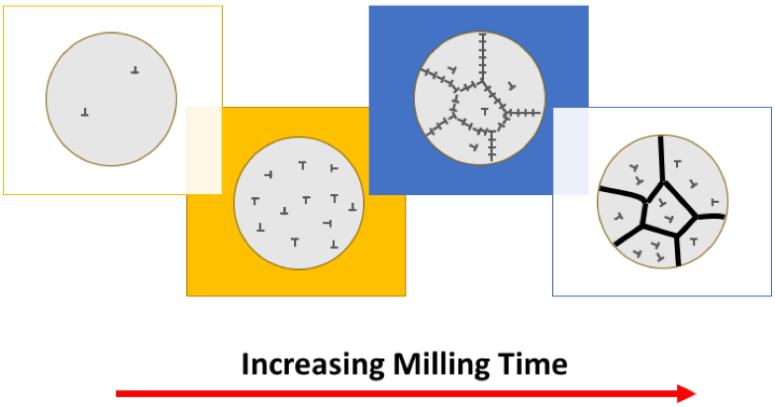

Figure 2.3: Schematic representation of grain refinement mechanism during ball milling.

Sever plastic deformation during the cryomilling process introduces strain energy to the bulk material as a result of dislocation generation. The deformation also causes grain structure modification as demonstrated schematically in Figure 2.3. The sever plastic deformation and the strain introduced due to milling process generates a high density of dislocations, these dislocations rearrange themselves into cells, subgrains and eventually ultrafine and nanosized grains [27]. The grain boundary energy increases as a result of powder grain refinement. When the powder is subjected to intense dynamic collisions between balls and the powder, the strain energy which is stored in the form of crystalline defects such as dislocations and other types of defects is released and because of the energy conservation the grain boundary energy increases.

It has been suggested that the interaction of the nitrogen from the cryomiling media with the metal powder forms metal nitride nanoparticles to activate Orowan strengthening mechanism [13, 28]. The activation energy required for diffusion of nitrogen to the metal powder and formation of nitride nano particles can be provided from the strain energy introduced to the powder. Lin et al. [28] suggested a mathematical model to estimate the strain energy during the milling process. Several processing parameters such as friction coefficient between the milling balls and powder, uniaxial tensile yield stress of powder, the geometry and the dimensional change of entrapped powder and shear work hardening factor and index.

$$U_i = ft\left(u_{E,\sigma_z} + u_{Em\sigma_r} + u_S\right)/m \tag{2.4}$$

Where f, t, u_{E,σ_z}, u_{E,σ_r}, u_S and m are the frequency of collision, milling time, the normal stress component along the height direction, the normal stress component along the radial direction, the shear stress component and the mass of powder respectively.

$$u_{E,\sigma_z} = 2\pi\Delta hY\left[-\frac{h}{2\mu}r_E - \left(\frac{h}{2\mu}\right)^2 - \left(\frac{h}{2\mu}\right)^2 \exp\left(\frac{2\mu}{h}r_E\right)\right] \tag{2.5}$$

$$u_{E,\sigma_z} = 2\pi hY\left[\sqrt{\frac{h}{h-\Delta h}} - 1\right] \times \left[-\frac{h}{2\mu}r_E - \left(\frac{h}{2\mu}\right)^2 + \left(\frac{h}{2\mu}\right)^2 \exp\left(\frac{2\mu}{h}r_E\right) - \frac{r_E^2}{2}\right] \tag{2.6}$$

Where Y is the uniaxial tensile yield stress of the powder, μ in the coefficient of friction between powder and balls. h and r_E are the height and radius of the cylindrical shape trapped powders.

$$u_s = KV_E\left(\int_0^{\gamma_{zx}} \gamma_{zx}^n d\gamma_{zx} \int_0^{\gamma_{zy}} \gamma_{zy}^n d\gamma_{zy}\right) \tag{2.7}$$

Where K and n are the shear work-hardening factor and index respectively,γ_{zx} and γ_{zy} are the shear strains and V_E is the entrapped powder aggregates volume.

Table 2.1 presents all the cryomilling parameters associated with the milling media and the Mg powder for calculating the introduced strain energy for the specified milling time. In this study we considered two types of stainless steel ball materials one made of SS 316 and the other one made from SS 440C. The rest of parameters other than the milling ball materials properties remained the same for both of the calculations.

2.1.2 Consolidation (compaction and sintering)

For the nanostructured powders to be applicable to construct actual products a density close to the theoretical density and a minimum mechanical strength depending on the product function are required. Consolidation typically combines pressure and temperature to form strong atomic bonding between the particles to reach high compactness and a density close to the theoretical density and without significant coarsening and agglomeration of the reinforcement particles.[18].

Table 2.1: Cryomilling parameters associated with the introduced strain energy.

		Parameters	Mg/SS316	Mg/SS 440C
Media	F	Impeller's rotational frequency (1/s)	3-4	3-4
	R	Attritor radius (m)	0.15	0.15
	ρ_B	Ball density (kg/m^3)	8000	7667
	E_B	Balls Young's modulus (Pa)	$2.1 \times 10^1 1$	$2.03 \times 10^1 1$
	r_B	Ball radius (m)	0.003	0.003
	M	Total ball mass (kg)	40	40
	V_m	Milling volume (m^3)	0.1037	0.1037
	H	Height of ball milling space (m)	0.206375	0.206375
Powder	ρ_P	POwder density (kg/m^3)	1740	1740
	Y	Uniaxial tensile yield strength (Pa)	20,000,000	20,000,000
	m	Mass	1	1
	K	Work hardening factor	534,000,000	534,000,000
	n	Work hardening index	0.4573	0.4573
Media and powder	C	Ball/powder mass ratio	40	40
	μ	Ball/powder friction ratio	0.4	0.4

The driving force for the densification of the nano-sized particles can be high because of the high surface energy resulted from larger surface area of these powders compared to equal volume of the same powder with conventional size. This results in sintering of such powder in lower temperatures compared to the conventional particle sizes. The enhanced kinetics of sintering for nano-sized powder causes the sintering process start at $0.2-0.4T_m$ compared to $0.5-0.8T_m$ for particles with larger sizes (micron or larger).

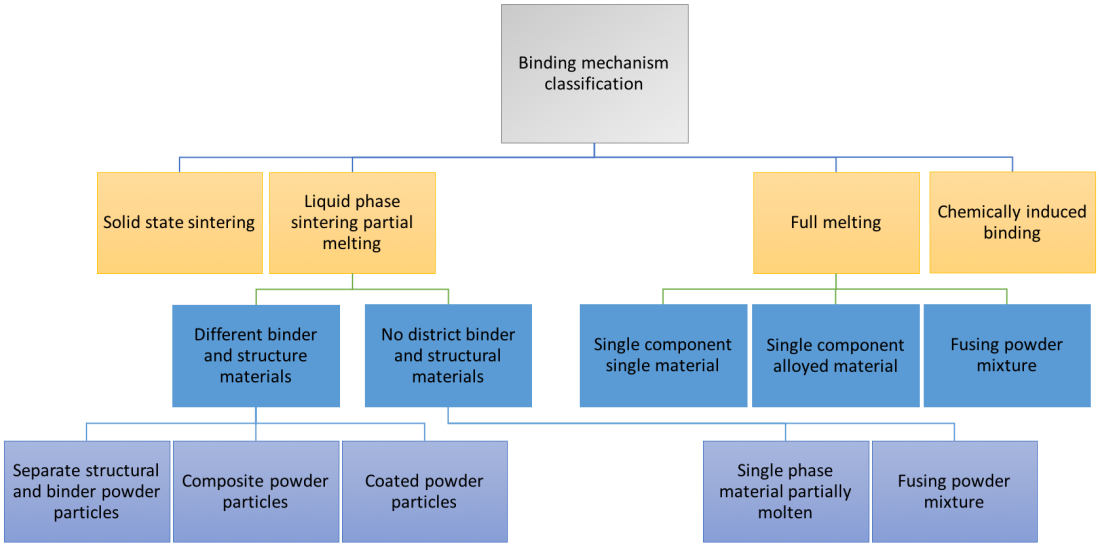

Figure 2.4: Laser Based powder consolidation mechanisms[1].

In traditional consolidation methods the first step before sintering the powder is the compaction which is initially applied to the powder at room temperature to obtain a sample with green density. The work part after compaction is called green compact and the word green means that the part is not yet fully processed (the part is unfired and only pressed). The green density of the part is higher than the initial density due to pressure during compaction but not uniform in the green compact. In this step the goal is to obtain green compact with enough stability to tolerate further handling to the next step [18]. Then it requires to be sintered. Sintering is a thermal treatment for bonding particles into a coherent, predominantly solid structure via mass transports in atomic scale resulting in a improved strength and a lower system energy [29]. Such process requires enormous compressing machines and high temperature furnaces. Powder bed consolidation techniques were introduced in late 80's to overcome the complications of powder processing and facilitate the powder based production process. The importance of these technologies is confirmed by recent study of NACFAM ($NationalConcilforAdvancedManufacturing, USA$). That has identified Rapid Manufacturing as the most innovative and potentially disputed manufacturing technology to emerge within next few years [1, 30].

Powder Bed Fusion (PBF) defined in ASTM F2792 [**?**] applies thermal energy to selectively fuse areas of layer of powder using a heat source such as laser or electron beam. Different branches of PBF has been introduced to produce polymer, metal or composite parts. Figure 2.4 shows different categories of powder based consolidation mechanism in detail. Lower power lasers bind the particles surfaces by surface melting and producing green parts that require further post-processing to make them fully dense. Using higher power for the laser beam fully melts the particles which causes them to fuse together and bind with the previous layer as it solidifies. The later method is of primary interest of this study as it does not require additional steps for producing the final part [31].

Figure 2.5 demonstrates the schematic view of Selective Laser Melting (SLM). The laser beam which is considered to be a Gaussian heat source irradiates the top surface of the powder bed, a fraction of the energy from the heat source is reflected, and the remaining energy is absorbed. The high energy density applied to the surface results in formation of a small-sized melt pool. Beside conduction and radiation convection is also responsible for heat transfer, energy loss and phase changes in SLM process.

The special and temporal distribution of the transient temperature fields of complex three

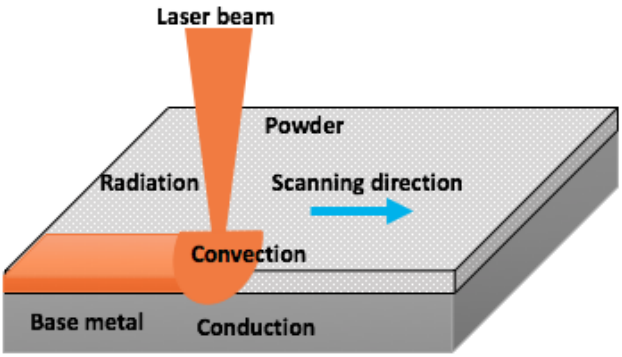

Figure 2.5: Schematic of selective laser melting process

dimensional structure of domain D can be expressed as equation 2.8 [32, 33]. Prediction of instantaneous temperature field results in better understanding of the details of the SLM process, minimizes defects in the final product and provides a guide for optimizing the processing parameters. Here ρ is density, c is the specific heat capacity, T is the temperature of the system, t is the time, k is the thermal conductivity and Q is the generated heat per volume within the component.

$$\rho c \frac{\partial T}{\partial t} = \frac{\partial}{\partial x}\left(k\frac{\partial T}{\partial x}\right) + \frac{\partial}{\partial y}\left(k\frac{\partial T}{\partial y}\right) + \frac{\partial}{\partial z}\left(k\frac{\partial T}{\partial z}\right) + Q \tag{2.8}$$

For SLM processing of the powder there are several parameters responsible for defining the condition of the system. Laser power (P), scanning velocity (V), laser spot diameter (d), scanning pattern, scanning hatch distance (b), powder layer thickness (a). Considering a fix size for the laser spot the input energy density is defined as $E = \frac{P}{V \times b \times a}$ and the geometry of the melt pool, heat affected area, quality of fusion, cooling and solidification rate, etc. can be calculated based on the input energy density.

The temperature distribution in the powder bed at the initial time in domain is considered to be T_0 the heat transfer on the surface of system where the heat flux (q) is presented can be defined as equation 2.9 [34]:

$$k\frac{\partial T}{\partial n} - q + q_c + q_r = 0 \tag{2.9}$$

q_c the convection and q_r radiation heat in quation 2.9 can be described as:

$$q_c = h(T - T_0) \tag{2.10}$$

$$q_r = \sigma\epsilon(T^4 - T_0^4) \tag{2.11}$$

Where h is the coefficient of heat convection, σ is the Stefan-Boltzmann constant and ϵ is the emissivity. The mathematical expression of the input heat flux with Gaussian distribution is defined as equation 2.12 [35].

$$q = \frac{2AP}{\pi\omega^2} exp\left(\frac{2r^2}{\omega^2}\right) \tag{2.12}$$

Where A is laser absorption of powder and ω represents the radius of the Gaussian laser beam, defined as the distance from the center of laser beam to the point where heat flow density mitigates to $\frac{1}{e^2}$ times of that at the center of the laser beam, r represents the distance of a point on the surface of powder bed measured from the laser beam center at time t. If $|x|$ and $|y|$ are the distance along X- and Y- axis.

$$r^2 = (|x| - |V.t|)^2 + |y|^2 \tag{2.13}$$

Various mathematical, numerical, finite volume and finite element analysis have attempted to describe the heat transfer mechanisms in the porous media undergoing phase changes during SLM process [33, 34, 35, 3, 2, 11, 36, 37, 38]for different alloys and metal matrix composites. An early study by Jeager [39] provides a mathematical model to describe the motion of moving heat source on the medium. Later JunChang et al. [40] simulate the heat transfer by using a semi-analytical way to evaluate the temperature distribution for pulsed laser treatments. The finite element model by Matsumoto [41] was one of the earliest computational approaches that analyzed the temperature development during SLM process in powder bed for metallic powders in 2-D. Tolochko et al. [42] investigated the laser sintering mechanism involving partial melting of the powder. Another model developed by Cervera [43] demonstrates that thermal properties are changed by porosity. Yang et al. [44] provided a 3-D finite element model for direct laser fabrication considering temperature-dependent materials properties. In their model Nisar et al. [45] considered the phase changes with

respect to the moving heat source. The 3-D finite element model by Roberts et al. [46] considered the powder bed with multilayer sintering mechanism, phase change, porosity and temperature-dependent material properties. In addition to the early attempts to describe the behavior of metal powders several more recent studies have focused on more challenging materials such as light weight alloys and composites. The study by Li and Gu [2] studies the geometry of the melt pool for the AlSi10Mg alloy considering a transient thermal behavior for a porous powder media and the porosity to be calculate as:

$$\phi = \frac{\rho_s - \rho_p}{\rho_s} \tag{2.14}$$

Where ρ_s is the density of the solid material with 100% density and ρ_p is the density of the powder. The prosity in most of the studies varies from $\phi = 0.4$ for powder to $\phi = 0$ for dense solid. In the contour map of Figure 2.6 they demonstrate the contour map for the temperature profile for the laser scanning of AlSi10Mg with 250W power and 200 mm/s laser scanning velocity. They showed that with this energy input the depth of the melt pool will be 61.7 μm and the highest temperature achieve as demonstrated in Figure 2.7 shows that as the laser power increases the maximum temperature also increases and at a constant scanning velocity of 200mm/s the maximum temperature of the system increases from 875 K to 1750 K when the laser power changes from 150 W to 300 W.

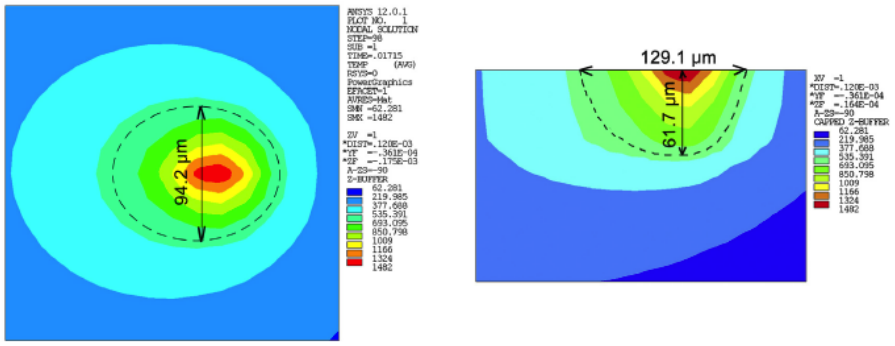

Figure 2.6: Melt pool geometry and temeprature distribution during SLM process where P=250W and V=200 mm/s. (a)top view (b) side view of the cross section of the melt pool [2]

In another work Dai and Gu [3] demonstrated the liquid metal turbulence and Marangoni effect

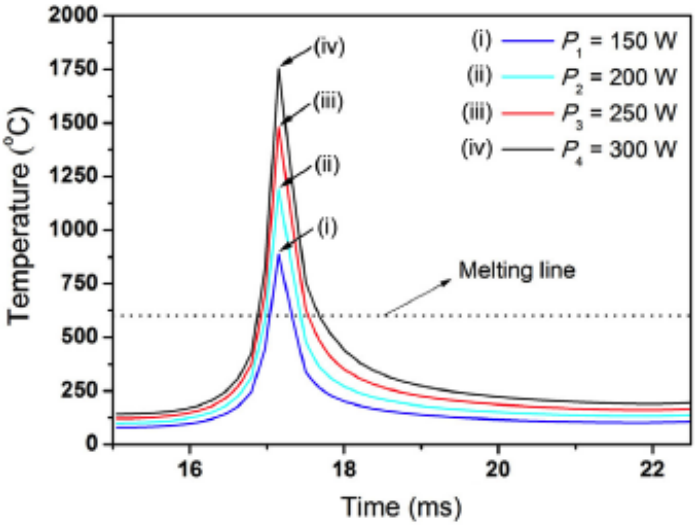

Figure 2.7: Temperature variation over the time for a portion of scanning time at the center point of the surface where P=150W, 200W, 250W and 300W and V=200 mm/s. [2]

during SLM process, resulting in motion of gas bubbles in the melt pool. Figure 2.8 shows how thermo-capillary flow (Marangoni convection) induced by surface tension affects the behavior of the gas bubbles. Since the intensity of the fluid flow increases with the enhancement of input linear energy density some vortex is observed in the melt pool with respect to the energy input. This vortex results in scaping of the bubbles from the melt pool by increasing the energy input. However at very high linear energy densities although the bubbles have the capability to scape from the pool the rotational pattern of the flow entraps the bubbles at the bottom of melt pool.

Forouzmehr et al. [36] considered the optical penetration depth of the laser to account to estimate the geometry of melt pool with respect to the experimental shape. Yan et al. [4] studied the SLM process in multi-physics scheme and focused on the particle melting as the laser heats up the surface. Figure 2.9 shows the particle melting process in during the laser scanning process. Wu et al. [37] considered the random distribution of powdered particles and their effect on the melt pool behavior. In their model Liu et al. [47] considered the effect of thermal analysis during SLM for their columnar to equiaxed transition (CET) model and developed a solidification model to study the microstructure of AlSi10Mg alloy during laser scanning path.

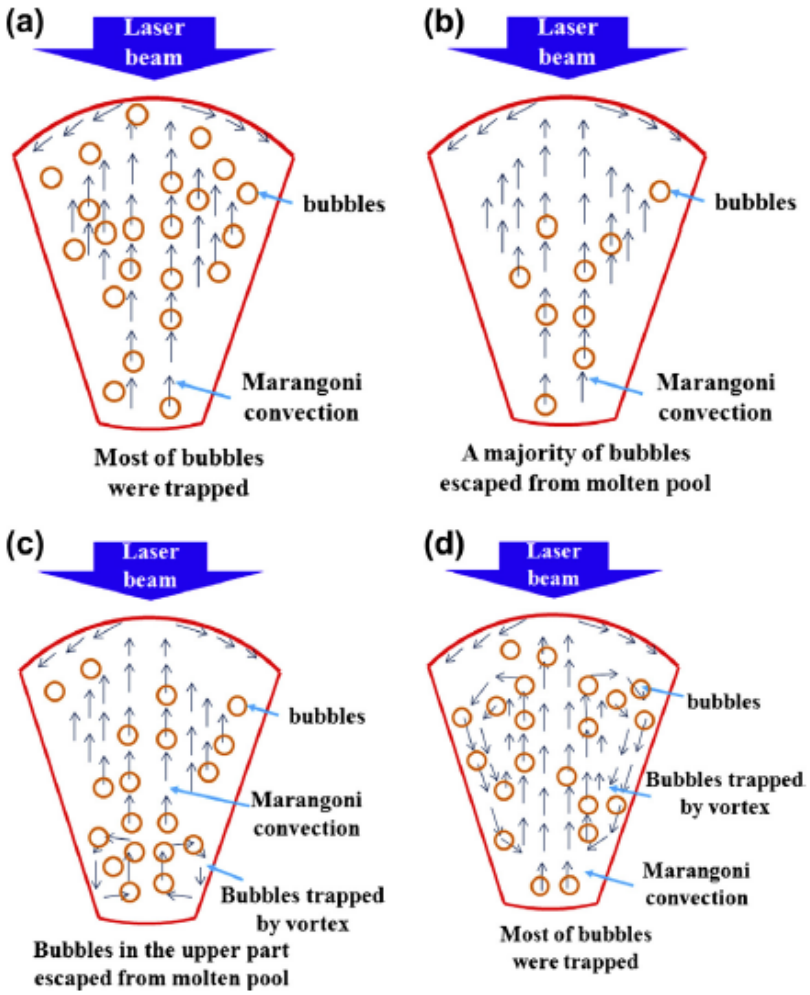

Figure 2.8: The schematics of gaseous bubbles movement in the melt pool on increasing linear energy denisty (LEDs): (a) LED = 15 kJ/m, (b) LED = 17.5 kJ/m, (c) LED = 20 kJ/m, and (d) LED = 22.5 kJ/m. [3]

2.2 Microstructures of PM nanocrystalline alloys

There are two main difference between the microstructure of nanocrystalline alloys processed through powder metallurgy compared to traditional ingot metallurgy [48, 49]. The first noticeable difference is that the alloys processed by powder metallurgy typically contain a significant volume fraction of second phase particles formed during the processing and in addition to the intentionally added reinforcements or the particles formed due to the alloy chemistry. For instance, Al_2O_3 particles are regularly present in the Al based alloys as a result of oxidation of powder surface. This thin oxide layer breaks up during the processing and distributes evenly in the structure.

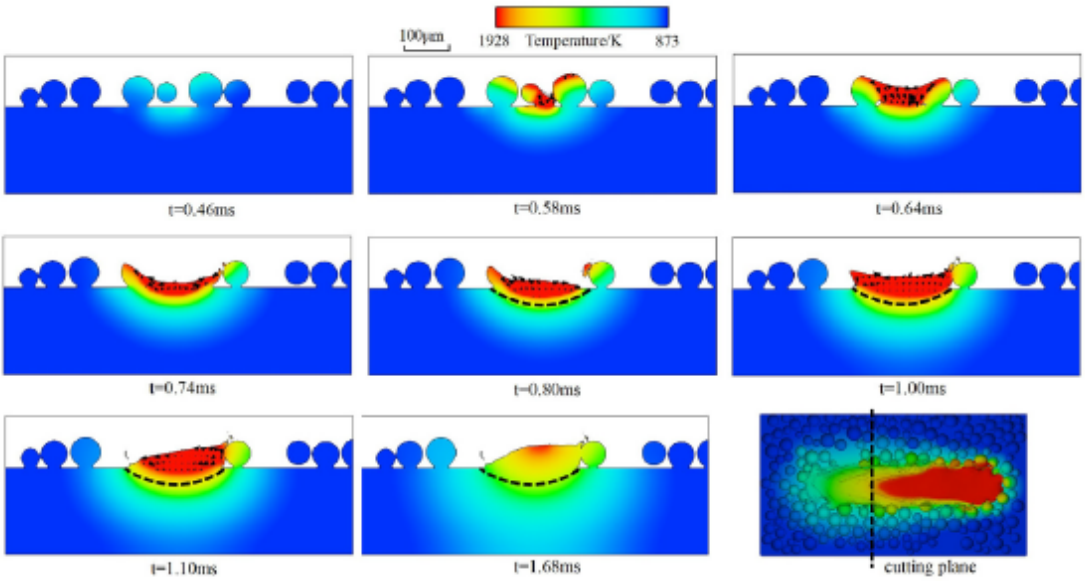

Figure 2.9: Simulation results of formation process of nonuniform single track (cross section view). The black dashed curve represents the bottom boundary of melted region in the substrate. The arrows are velocity vectors. [4]

The higher amount of secondary phases particularly Al_2O_3 and AlN in Al alloys and Mg_3N_2 in Mg alloys seems to have constructive effects on the mechanical properties of the alloy. The strengthening mechanisms and the contribution of the secondary phases will be discussed in more details in the next section. The second difference is the presence of a large fraction of low angle boundaries in the as-processed and annealed condition which can vary depending on the thermomechanical processing. Unlike the secondary phases, the existence of low angled grain boundaries is not advantageous for enhanced mechanical properties. The reason for this negative effect is that the plastic deformation is controlled by the sliding and the low angle boundaries are not amenable to sliding. In the case that the as-processed and annealed material contains a significant large fraction of low angle grain boundaries a conversion to high angle grain boundaries is required. This is due to predominant quantity of low angle grain boundaries, the deformation is limited to the intergranular dislocation generation and motion, by applying strain to the alloy, the low angle boundaries transfer to high angle boundaries and grain boundary sliding becomes the dominant deformation mechanism.

The formation of the secondary phases sometimes is activated due to the mechanical milling of the powder. Tavoosi et al. [5] demonstrated that milling a mixture of Al and ZnO powder for 60

hours results in a replacement reaction with the formation of Al_2O_3 and Al and Zn solid solution. Figure 2.10 shows the morphology of the Al-Zn alloy including nanosized Al_2O_3 powder in part (a) and Al-Zn alloy powder in part (b). They also showed that at the beginning of the milling the solubility of Zn in Al is higher than the equilibrium state which is accompanied by a decrease in lattice parameter of the Al matrix. At the later stages of milling times, Al-Zn supersaturated solid solution decomposes and the lattice parameter of Al increases resulting in a decrease in hardness value of as-milled powder [50].

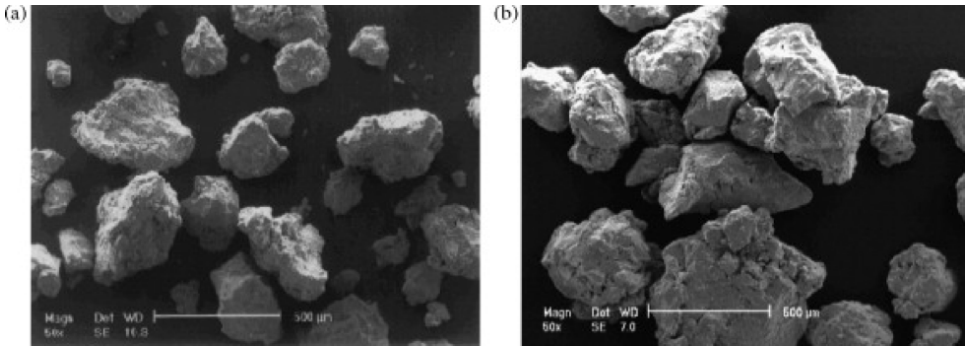

Figure 2.10: Morphology of powder particles after 60h ball milling (a) Al-Zn alloy with Al_2O_3 nanopowder (b) Al-Zn powder [5].

In another study on the Al-based nano-powders Al-Aqeeli et al. [6] described the strengthening mechanism responsible for increased hardness of Al-Mg-Zr elemental powder mixture by increasing the Zr content. When the amount of Zr element increases in the composition of the alloy a nanocomposite formed from the Al(Zr,Mg) solid solution and an intermetallic. At this point considerable enhancement in structural stability and hardness of the alloy was observed. The X-ray diffraction patterns reported in Figure 2.11 confirm the formation of Al_3Zr and Al_3Zr_4 intermetallics and ZrO_2 oxide during the milling process of Al-Mg-Zr powder mixture. Also Figure 2.12 shows the formation of $Al_{12}Mg_{17}$ by increase in the amount of Mg content in a Al-Mg binary alloys [7]. Experiments show that the Zr-rich intermetallics do not find a chance to form during the milling process if the amount of Mg is higher than 10%. Annealing the alloy may assist the formation of intermetallics such as $Al_{9.83}Zr_{0.17}$ for ternary alloys containing $40-55\%$ Mg and 5% Zr.

Al-Aqeeli et al. [6] developed a new Al-Mg-Zr nanocomposite combining nanosized particles distributed in an amorphous structure to enhance the mechanical properties. This idea was first proposed by Kim et al. [51] to produce ultrahigh strength in Al88Y2Ni9M1(M=Mn or Fe). Some

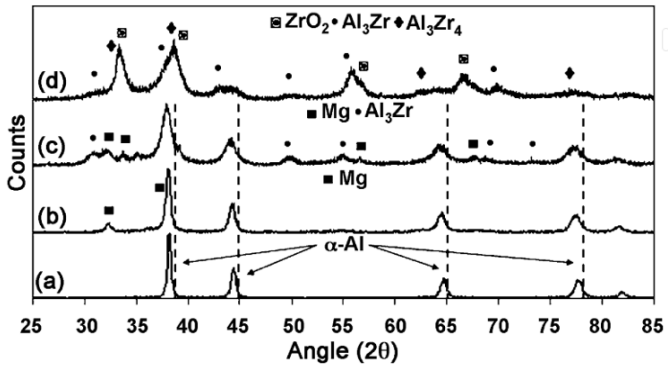

Figure 2.11: X-ray diffraction patterns of as-milled (a)10Mg-90Al, (b) 10Mg-85Al-5Zr, (c) 10Mg-70Al-20Zr and (d) 10Mg-55Al-35Zr [6].

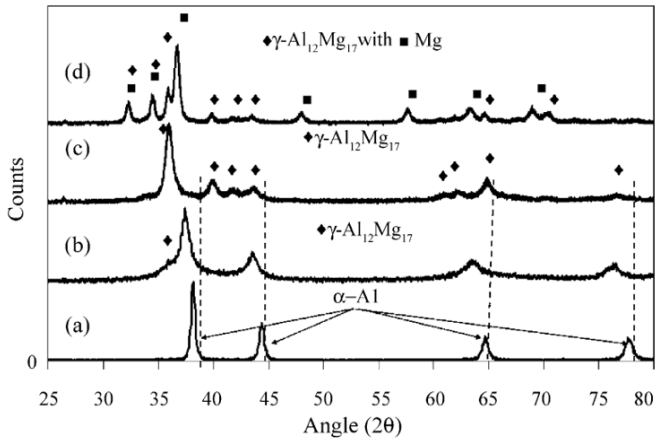

Figure 2.12: X-ray diffraction patterns of as-milled (a)10Mg-90Al, (b) 40Mg-60Al, (c) 60Mg-40Al and (d) 90Mg-10Al)[7].

finely dispersed FCC-Al particles in the amorphous matrix. High resolution transmission electron microscopic (HRTEM) image of the Al-10Mg-20Zr alloy showing the coexistence of nanocrystalites and amorphous phase is presented in Figure 2.13.

2.3 Mechanical properties of PM nanocrystalline alloys

2.3.1 Grain refinement and Hall-Petch effect

Considerable enhancement has been observed in the mechanical properties of Mg based alloys based on the Hall-Petch relationship. An important factor that makes grain refinement one of the most effective methods for improving the mechanical properties in Mg alloys is their high K value

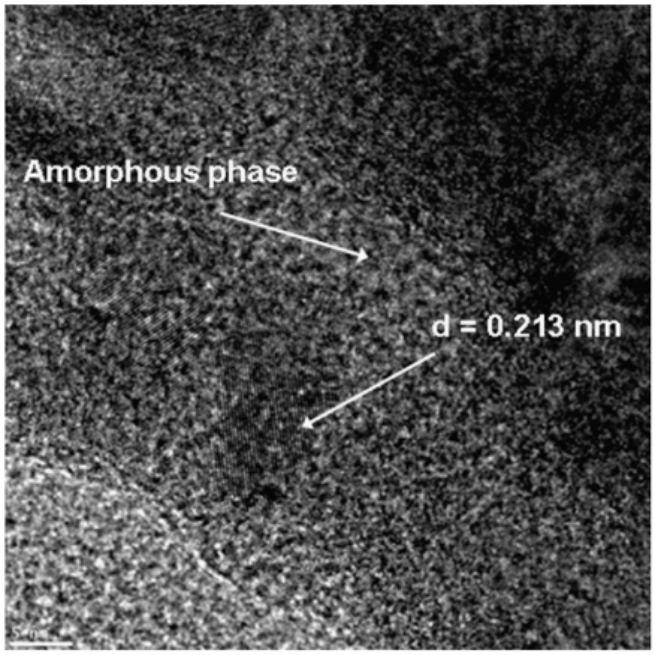

Figure 2.13: HRTEM image of Al-10Mg-10Zr alloy highliting the region containing both amorphous and nanocrystaline structures [6].

[51, 52]. As the Hall-Petch relation states the Yield strength of polycrystalline materials is directly influenced by the grain size [53, 54]

$$\sigma_y = sigma_0 + \frac{k_y}{\sqrt{D}} \tag{2.15}$$

Where σ_y is the Yield strength, σ_0 is the starting stress for dislocation movement. This is the Yield stress of a single crystal in the absence of any strengthening mechanism other than solid solution.k_y is the strengthening coefficient (constant for each material) and D is the average grain size. In the cases where the presence of external particles results in grain refinement and metal matrix nano composites form the equation can be modified, to incorporate the grain refinement effect in MMNCs, as

$$\Delta\sigma_{GR} = k_y \left(\frac{1}{\sqrt{D_{MMNC}}} - \frac{1}{\sqrt{D_0}} \right) \tag{2.16}$$

D_{MMNC} and D_0 are the average grain sizes of polycrystalline matrix in MMNC and the unreinforced material, respectively. For this equation to be valid, only the grain structure can change due to grain refinement and all the other factors such as precipitation condition or texturing resulting

from mechanical post-processing [55]. In general, it is suggested that the second-phase particles in polycrystalline materials pin the grain boundaries and limit the grain growth [8]. Accumulation of incoherent second phases at the boundaries decreases the energy of the system due to reduction in their areas. These secondary phases also inhibit the boundary movements and because these boundary motions require generation of more boundaries in the spots that particles previously resided, this will result in an energy increase. Zener and Smith [56] explained that the corresponding force between a single particle and a boundary could be calculated from

$$F = \pi\gamma(r) \tag{2.17}$$

where γ is the grain boundary energy and r is the particle average radius. This equation can be modified for multiple particles interacting with the boundary.

$$F = (3/2)\gamma(f/r) \tag{2.18}$$

In this equation f is the volume fraction of pining particles, and the particle spacing $\lambda = \sqrt{lt/f}.l$ and t are the length and thickness of the particle. The grain boundary, secondary phase interaction concept has been developed over the time to comprehend the effect of particle-grain boundary interaction geometry, the interaction of coherent particles with boundaries, a random and non-random particle distribution and particle shape [57, 58, 59, 60, 61]. Although a several forms of Zener equitation have been proposed considering different parameters, all these equations keep the original equation form and among the parameters controlling the pinning force, the particle size (r) and the particle spacing (l) have the critical rolls in eliminating the grain growth. It worth mentioning that the contribution of the nano particles in a metal matrix material is only grain refinement and restricting the size of the grains in the MMNCs rather than assisting new grain nucleation. The Zener equation then can be formulated to

$$D_m = \frac{4\alpha d_p}{3V_p} \tag{2.19}$$

During the grain refinement and grain boundary pinning through the nanoparticle addition during the processing and post-processing. Where α is a proportionality constant, D_m is the

smallest grain size of the matrix, d_p is the reinforcement particle diameter, and V_p is the volume fraction of particles [56]. For MMNCs it is recommended that the equation without explicit effect of particle size be used and instead the grain size effect be considered. D_0 here is the grain size that results from processing conditions when the alloy contains no reinforcement particles and p is the proportionality constant that describes the refining power of the reinforcement, which can be empirically determined.

$$D_m = \frac{D_0}{(1 + pV_p)^{\frac{1}{3}}} \tag{2.20}$$

Although grain refinement and the Hall-Petch effect are known as common strengthening mechanisms in alloys, it has been demonstrated that in some nanocrystalline materials when the grain size falls below a critical value the strength may decrease due to an effect known as inverse Hall-Petch behavior. Several factors affect the inverse Hall-Petch behavior including Coble creep, the absence of dislocation pile-ups at the ultrafine grain sizes, the Coble creep operation with a threshold stress and the process of a stress assisted thermally activated process in the boundary [62, 63, 64, 65, 66, 67]. Most of the models predicting the nanoscale softening usually predict unrealistic values for the grain size corresponding to the transition from hardening to nanoscale softening. They also have predictions which are not entirely consistent with several deformation characteristics reported for nano-crystalline materials that include high and variable stress exponent, activation volume with the range $10b^3 - 40b^3$, an activation energy close to that of boundary diffusion and limited ductility. On the other hand, it has been suggested by Mohamed et al. [68] that while the Hall-Petch behavior controls the strength of larger grains a new deformation process based on dislocation sliding containing boundary sliding for smaller grains is activated. In this way the nanoscale softening can be quantitatively predicted. Figure 2.14 plots the applied shear stress against $\frac{1}{\sqrt{d}}$, the straight line is the Hall-Petch equation and the curve represents the dislocation accommodated boundary sliding. For the grain size larger than the d_c conventional Hall-Petch behavior is dominant and as the grain size becomes smaller than d_c strength is determined by dislocation-accommodated boundary sliding.

$$\dot{\gamma} = 9\left(\frac{b}{d}\right)^3 \left(\frac{D_{gm_0}}{b^2}\right) \exp\left(\frac{-Q_{gb}}{RT}\right) \left[exp\left(\frac{2vb^3}{kT}\right) - 1\right] \tag{2.21}$$

Where b is the Burgers vector, d is the grain size, D_gbo stands for the frequency factor for grain boundary diffusion, R is the gas constant, Q_gb, τ, T, k and v are the grain boundary diffusion activation energy, applied shear stress, the absolute temperature, Boltzamanns constant and the activation volume, respectively. This equation can be presented in another way as

$$\frac{1}{\sqrt{d}} = \left[\frac{\left(\frac{\dot{\gamma}}{9} \left(\frac{exp\left(\frac{-Q_{gb}}{RT}\right)}{bD_{gb_0}} \right) \right)}{\left(exp\left(\frac{v\tau}{kT}\right) - 1\right)} \right]^{\frac{1}{6}} \tag{2.22}$$

To plot the applied shear stress vs. $\frac{1}{\sqrt{d}}$ for Al as demonstrated in Figure 2.14, the activation volume is considered as $10b^3$, Q_{gb} and D_{gb_0} are equal to 85kJ $mole^{-1}$or $0.6Q$, where Q is the activation energy for lattice diffusion and $1.86cm^2s^{-1}$, respectively. Shear strain rate is $10^{-3}s^{-1}$, T =300K and b is equal to 0.289nm. The data in this figure are superimposed, to show the transition from conventional Hall-Petch to inverse Hall-Petch behavior [69, 70].

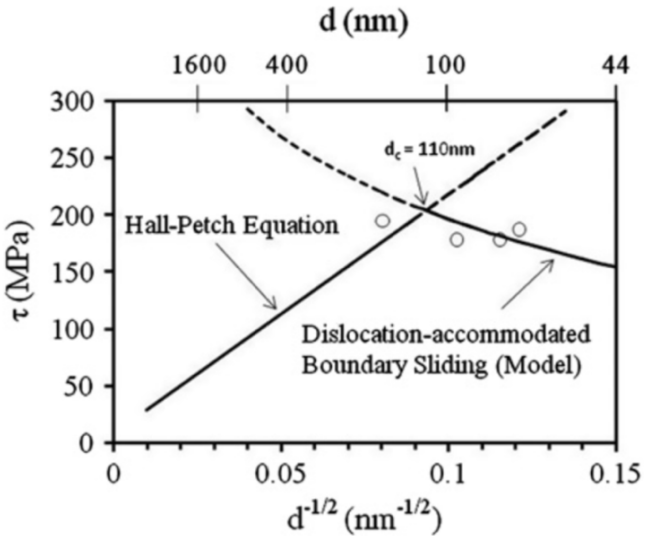

Figure 2.14: The critical grain size is calculated as the intersection of the equation of Hall-Petch behavior with the equation corresponding to the dislocation-accommodated grain boundary sliding [8].

2.3.2 Orowan strengthening

Presence of secondary phases in the nano-crystalline alloys can activate another mechanism, known as Orowan strengthening mechanism. The Orowan strengthening model corresponds to the mechanical behavior enhancement as a result of small hard particles resisting against the motion of dislocations. In the interaction of dislocations and hard nano particles, the hard phase functions as obstacles and results in bowing of the dislocations followed by reconnection and finally formation of loops around the particles. Formation of the dislocation loops, leads to high work hardening in the alloy [71, 72, 73, 74, 75]. A schematic demonstration of this process is demonstrated in Figure 2.15.

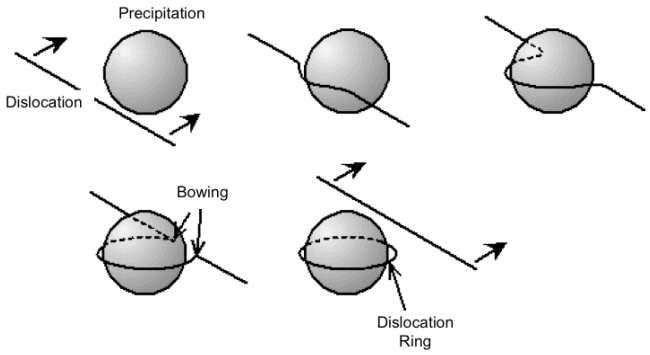

Figure 2.15: Schematic demonstration of dislocation, secondary phase interaction during the Orowan strengthening process.

2.3.3 Enhancing the ductility in nano-crystalline alloys

Application of nanostructured metals and alloys in the bulk form requires them to combine tensile strength with ductility. Improving the ductility of PM nano-crystalline alloys in some cases is a challenge since the brittleness can be too high to affect the practical use of such materials in spite of their high strength [76]. Here some strategies will be proposed to enhance the tensile ductility of such alloys simultaneously keeping the majority of the strength resulted from Hall-Petch effect and nano-sized grains. Depending on the application, the type of acceptable deformation before failure varies. For most of applications a significant uniform elongation is required under tensile stress, but in most of the cases nanocrystalline alloys gain their strength at the expense of ductility [77].

The first suggestion is to mix up the length scales, specifically by creating a bimodal or even

multi-modal grain size distribution, which can result in high yield strength combined with fairly large uniform elongation. It worth mentioning that a functionally gradient material with a combination of good strength and ductility is beneficial for fatigue performance. Although there is a small trade-off to lose some strength, but the gained uniform strain is considerable compared to the small loss of strength in nano-micro-scale bimodal structures. Such grain structure can be achieved either from mixing powders with different grain sizes [9] or by rolling the metal at liquid nitrogen temperature and then applying annealing heat treatment techniques [15]. In the latter method the resulting material has a typical heavily deformed microstructure with high density of dislocations in a nanoscaled network. The low temperature of liquid nitrogen delays the dynamic recovery and allows the dislocation density reaches a higher steady-state level than that achievable at room temperature. The former method on the other hand blends specified volume fraction of micron-sized powders with the same compositions with the cryomilled powder of nano grain size. This mixture is then extruded to form the bimodal alloy. Formation of Lüders bands during the tensile testing of these alloys was reported and caused enhancement elongation compared to purely nanostructured alloy. Han et al. [9] reported that they did not observe obvious necking during the plastic deformation of 5083 Al bimodal alloys, but confirmed the formation of Lüders bands, as demonstrated in Figure 2.16. The Lüders bands are reported to form immediately after the maximum load and was accompanied by a stress-drop period. During subsequence deformation, intense plastic deformation is reported to be localized in the vicinity of the Lüders bands.

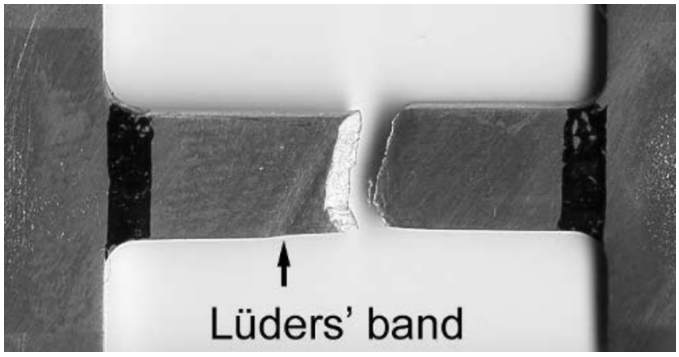

Figure 2.16: A failed tensile specimen of the bimodal 5083 Al alloy containing $30 Vol\%$ coarse grains [9].

The second approach to reach high strength and ductility in the materials is using a mixture of two or multiple phases with different sizes and properties or in other words using composites instead

of alloys. A combination of ductile particles in strong but brittle matrix may result in high ductility without considerable loss of strength. Such system may benefit from large number of interfaces formed as a result of solidification, a high strain hardening rate because of dislocation accumulation in the micro-sized dendrites, and finally large plastic strains resulted from the large number of slip bands and profuse dislocation activities [78, 79]. The next method takes advantage of formation of nanoscale growth twins instead of the nano sized grains for strengthening. It is suggested by Lu and Ma [10, 80] that a high density of coherent twin boundaries promotes high yield strength while preserving the capacity for effective dislocation storage. This effect results in high strain hardening rates at high flow stresses, stabilizing uniform tensile deformation to large plastic strains which combines ultrahigh tensile strength with a considerably large elongation to failure. A transition-electron microscopy (TEM) of such system verifies the gathering of dislocations in regions where the twin spacing is large. The thin twin ribbons are cut by dislocations and dislocations sources are produced from accumulation of dislocations in twin boundaries and low defect content regions with coherent and low energy twin boundaries save room for dislocation storage upon tensile straining. Figure 2.17 illustrates and example of a strained sample with nanoscale twins after tensile test.

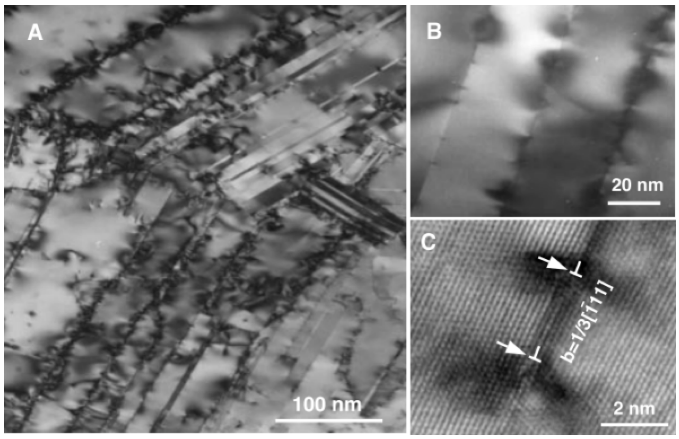

Figure 2.17: (A) TEM image of strained sample after tensile test showing nano sized twins and dislocation storage. (B) closer view of twin boundaries and dislocations. (C) TEM image of twin boundary with Frank dislocation and Burgers vector of $b = 1/3[\bar{1}11]$ [10].

The next approach to enhance the ductility of nanostructured alloys focuses on activating Orowan strengthening method by dispersing nano-pricipitates in the alloy. Precipitation hardening is known as the most effective method for some alloys [76]. In nano crystalline alloys, hard precipitates reduce the dynamic recovery by dislocation generation, dragging or pinning. Due to decrease

in the amount of dynamic recovery, a considerable amount of dislocations is stored, increasing the strain-hardening rate and resulting in a larger uniform strains simultaneously enhancing the strength [81]. The final approach considers the role of flaws such as porosity on reducing the ductility. Nano crystalline materials produced through consolidation suffer from lower strength if the porosity formation is not controlled in them. They also may initiate shear localization and consequently high propensity for shear banding in irradiated alloys or consolidated nano-crystalline metals. To prevent materials failure and ductility enhancement in consolidated materials it is required to obtain flaw free materials and consolidate the powder to full density with nano-sized grains and a narrow grain size distribution [82, 83, 84].

2.4 Corrosion behavior of Mg alloys

In spite of great potential of Mg and Mg alloys in wide range of applications, relying mostly on the high strength to weight ratio of these alloys, combined high resistance to heat/creeping, high elongation before fracture, these metals suffer from high (degradation) corrosion rates in oxygen atmospheres. Devices fabricated from Mg based metals require a diverse range of corrosion resistances depending on the sites and types of applications, however, the degradation rates of Mg/Mg alloys are generally much higher than required and practical implantation of Mg-based devices could present a formidable difficulty. There have been considerable research efforts focused on improving the corrosion resistance of Mg/Mg alloys [85, 86, 87, 88, 89, 90, 91, 92]. In general, controlling the types and contents of the alloying elements is the first and easiest way to improve the degradation/corrosion properties of metals. In case of Mg, it is experimentally validated that incorporating alloying compositions enhances the corrosion resistant properties of Mg to a certain degree. For example, it has been reported that a Mg alloy with containing up to 4% Al has a corrosion rate $4-9\%$ lower than pure Mg [93, 94, 95]. Ca and Zn are also of commonly included alloying elements in Mg-based materials [96, 97, 98]. Zn is often included to improve the mechanical properties of Mg alloys, even though research has shown that the corrosion resistance of alloys containing Zn could be slightly decreased [99]. Other studies have demonstrated that adding rare-earth elements (REs) such as Ce, La, Nd, and Y can improve the corrosion resistance of Mg-based alloys [83,90]. Among these studies of RE elements, Y has received the most attention, as

the standard electrochemical potential of Mg (-2.372 V) and Y (-2.372 V) are identical, which prohibits the formation of micro-galvanic cells in the alloy that can significantly lower the chance of local degradation [100]. Microstructural features also influence the degradation behavior of Mg/Mg alloys. The crystallographic orientation of a surface plane in contact with corrosive media can be a factor in determining the degradation rates of Mg/Mg alloys. For example, Song et al. [79] and Xin et al. [87] showed that loosely packed crystallographic planes of AZ31 alloy have greater tendency to corrode. Furthermore, they revealed that the basal plane has the lowest surface energy and slowest corrosion rate compared to other high-energy planes. Other efforts to enhance the resistance to degradation of Mg alloys include post-processing treatments such as coating, anodizing, and heat treatments [88, 101, 102, 103]. The micro-galvanic corrosion and hydrolysis are the main mechanisms that explain the degradation of Mg/Mg alloys. For the micro-galvanic degradation mechanism, the segregation of impurity elements with low hydrogen overvoltage (e.g., Ni, Fe, Cu) in the structure of Mg alloys lead to the development of intermetallic components that can serve as efficient cathodic sites [101, 104, 105, 106, 107]. Hydrolysis, on the other hand, is the reaction of the substrate with water and is not only restricted to the local electrochemical potential differences due to the compositional variations in the substrate. Here in the present work, as a primary analysis for the degradation process, we do not consider any segregation in the substrate, and we focus on the hydrolytic degradation and the surface dissolution of Mg/Mg alloys, placing an emphasis on solid solution effects. The interaction between a water molecule/water clusters and other transition metal surfaces has been widely studied using the density-functional theory (DFT) computation technique. Schnur and Gro [108] applied ab initio molecular dynamics (AIMD) to show that, although the ice-like hexagonal water bilayers could be polarized on strongly interacting transition metals surfaces, the electronic structure of the metal surface is weakly affected by the interaction with the water layer. Carrasco et al. [109] and Chen et al. [110] used DFT calculations to simulate the water cluster structure and they found that a strong adsorption of the water molecule on the metal surface leads to a hydrogen bonding among the water molecules. Kolb et al. [101,102] and Calle-vallejo et al. [111] also applied DFT calculations on stepped platinum surfaces and showed that surfaces with lower coordination number exhibit a higher tendency to adsorb water molecule. Peköz et al. [112] observed a similar adsorption behavior for water clusters on both flat and stepped transition metal surfaces. Greeley and Norskov [105] and Strasser et al. [113] studied

the thermodynamics trends of dissolution in the alloy surfaces of transition metals based on periodic DFT calculations. However, despite a rich history of experimental efforts to improve the corrosion resistance of Mg alloys introduced in the preceding paragraph, only a few attempts have been made to theoretically understand the corrosion mechanisms at the atomistic level. Velikokhatnyi et al. [114] showed that alloying Mg with Ca and Y may improve the corrosion properties by forming more stable protective passivation layers. Liu et al. [115] combined their experiments with the density-functional theory (DFT) calculations of the surface energy by Vitos et al. [116] to explain the dependence of corrosion behavior for pure Mg on crystallographic orientations. In this study, using the DFT computation technique, we attempt to explain the interaction between a water molecule and metallic surfaces, then we concentrate on the dissolution of Mg atoms from the surface of Mg/Mg alloys to describe the combined effects of surface orientations and types of alloying elements. Since the initiation of corrosion will occur through the hydrolysis mechanism involving the interactions between water molecules and metallic surfaces, quantifying the degree of these interactions will be useful for understanding the degradation behavior of Mg alloys. Further, because adding one impurity element can change the tolerance limits of other impurities, it is not a trivial task to understand the surface degradation of Mg alloys using experimental approaches. With this in mind, in the current work, we used the electrode potential shift calculations to explain the general dissolution behavior of Mg atoms from the surface of Mg alloys. In the following section, we introduce descriptions for DFT computational methodology along with calculation parameters. In Chapter 3, we provide detailed computational results and discussion on the adsorption of water molecule on Mg-based surfaces and electrode potential differences of these surfaces. In Chapter 4, we summarize these results and provide important remarks for the present study.

Chapter 3

Research methods

3.1 Density-functional theory (DFT) calculation

Density functional theory (DFT) also known as ab initio principle is one of the modeling approaches in this work. DFT based calculations have become a common method for many-body problems in solid state applications. As an initial step they deal with the total energy of the system and address methods to find the ground state energy of a many electron system [117]. This approach is capable of calculations from surface interactions to bulk material properties such as diffusion energy barriers and formation energies. Some fundamental aspects of DFT are reviewed in this part to build the foundation for the theoretical discussions on DFT based results. Concepts such as Schrödinger equation, molecular Hamilton operator, electronic wave function and the resulting Fermi correlations have been reviewed in this chapter.

3.1.1 Fundamental aspects in DFT

Schrödinger equation

In quantum mechanics the wave function ($\Psi(x,t)$) of a particle gives the probability of finding that particle at a certain position and the Schrdinger equation is used to find the allowed energy levels of quantum mechanical systems. The general form of Schrdinger equation for the time-dependent can be presented as

$$i\hbar\frac{\partial\Psi}{\partial t} = -\frac{\hbar^2}{2m}\frac{\partial^2\Psi}{\partial x^2} + V\Psi \tag{3.1}$$

Where $\hbar = \frac{h}{2\pi}$=1.054573 $\times 10^{-34} Js$, m is the particle mass, V is the potential energy and as it was mentioned earlier $\Psi(x,t)$ is the corresponding wave function. The charge density, energy of the many-body and non-interacting system can be calculated accurately if the functional is known [118]. However, the exact functional is not known but it is universal and does not depend on the material. The Schrödinger equation thus can be solved exactly, in principle, for any system and allows excellent approximations to the functional to be developed and used in unbiased and predictive studies for different materials consequently these approximations are referred to as *ab initio* or *first principles* methods.

Self-consistent-field (SCF)

Hartree-Fock or self-consisting-field method of the atom suggests that the motion of a single electron in the effective field of the other N-1 electron is governed by a one particle Schrödinger equation. Hartree equations for N one-particle wave-functions (atomic orbitals) are sets of coupled integrod-ifferential equations and the result of self-consistency of the electronic charge distribution with its own electrostatic field. The Hartree equations were shown to be the conditions for optimization of an approximate wavefunction consisting of atomic orbitals [119]. The Hartree equation for an N-electron atom where each electron moves in the potential field of the nucleus in addition to the N-1 other electrons is equal to

$$H_i^{eff}\psi_i(r) = \epsilon_i\psi_i(r) i = 1...N, \tag{3.2}$$

where H_i^{eff}

$$H_i^{eff}\psi_i(r) = -\frac{\hbar^2}{2m}\nabla^2 + V_i(\psi_1\psi_2...\psi_N) \tag{3.3}$$

and

$$V_i(\psi_1\psi_2...\psi_N) = -\frac{Ze^2}{r} + \sum_j \neq ie^2 \int dr' \frac{|\psi_i(r')|}{|r-r'|} \tag{3.4}$$

The potential V depends on the charge distribution of the electron (ψ_i) , the eigenvalues (ϵ_i) represents the total one-electron energies in the self-consistent field. In SCF approach the first step is to write the Hamiltonian operator for the N-electron atom. Which in a simplified form gives

$$H = \sum_{N}^{i=1} \{-\frac{\hbar^2}{2m}\nabla^2 - \frac{Ze^2}{r_i}\} + \sum_{J>i}\sum_{i=1}^{N}\frac{e^2}{r_{ij}} \tag{3.5}$$

Based on the suggested system of atomic units by Hartree:

$$\hbar = |e| = m = 1 \tag{3.6}$$

The atomic unit for length is equal to the first Bohr radius ($a_0 = \frac{\hbar^2}{me^2} = 0.529 \times 10^{(}-8)cm$), the atomic unit of energy equals to $1Hartree(Ha) = \frac{e^2}{a_0} = 27.2$ eV and the Hamiltonian is written as

$$H = \sum_{N}^{i=1} -\frac{1}{2}\nabla^2 - \frac{Z}{r_i} + \sum_{J>i}\sum_{N}^{i=1}\frac{1}{r_ij} \tag{3.7}$$

And the Schrödinger equation of an N-electron system is written as

$$H\Psi(r_1...r_N) = E\Psi(r_1...r_N) \tag{3.8}$$

E here is the total energy of the atom known as the energy required to dissociate a $N+1$ particle system. Also the exchange phenomena proofs that the probability of finding two electrons of parallel spin at the same point in space is exactly zero. Exchange forces or exclusion forces reduce the repulsive energy of the electrons of the same spin by keeping them apart. These forces result in formation of Fermi hole, the region around each electron effectively excludes to the electrons of the same spin which is a property of Fermi-Dirac particles.

$$f(E) = \frac{1}{e^{(E-E_F)/kT}+1} \tag{3.9}$$

In Fermi-Dirac distribution function for a system of identical fermions with thermodynamic equilibrium, E is the energy, Ef is the Fermi energy, k is the Boltzman constant and T is the absolute temperature []. Hartree-Fock scheme provides a subset of the equation consisting of an

approximation of the N-electron wave function by an antisymmetrized product of N one-electron wave functions, where the one-electron functions $\psi_i(r)$ are known as Orbitals with spin functions α or β . The composite spin-orbital functions may be defined as

and the simplest totally antisymmetric N-particle function is the determinantal form

Although Hartre-Fock approximation does not give the exact solution of the N-electron Schrdinger equation, it gives the best solution to the determinal form of it.

The energy functional

The energy functional in Schrödinger equation can be defined as

$$E[\rho] = T[\rho] + V_{ext}[\rho] + V_{ee}[\rho] \tag{3.10}$$

where T is the kinetic energy, V_{ext} the interaction with the external potential and Vee is the electron-electron interaction.

$$V_{ext}[\rho] = \int \hat{Vext}\rho(r)dr \tag{3.11}$$

As Kohn and Sham [120] suggested the kinetic energy can be calculated from equation and it is known exactly from the orbitals. Such a fictitious system of N non-interacting electrons can be described by a single determinant wavefunction in N orbitals ϕ_i . Here $\rho(r)$ is the electron density.

$$T_s[rho] = -\frac{1}{2}\sum_{i}^{N}\langle\phi_i|\nabla^2|\phi_i\rangle \tag{3.12}$$

$$\rho(r) = \sum_{i}^{N}|\phi|^2 \tag{3.13}$$

simplifying the electron-electron interaction to classical Coulomb interaction or Hartree energy can be written in terms of the density as

$$V_H[rho] = \frac{1}{2}\int\frac{\rho(r_1)rho(r_2)}{|r_1 - r_2|}dr_1dr_2 \tag{3.14}$$

Then the energy functional will be

$$E[rho] = T_S[\rho] + V_{ext}[\rho] + V_H[\rho] + E_{xc}[\rho] \tag{3.15}$$

Where $E_{xc}[rho]$ is the sum of the errors from applying non-interactive kinetic energy and the error due to treating the electron-electron interaction classically.

$$E_{xc}[\rho] = (T[\rho] - T_S[\rho]) + (V_{ext}[\rho] - V_H[\rho]) \tag{3.16}$$

Finding a functional $E_{xc}[\rho]$ that embodies the required information is done using very simple minded approximations. The most widely used approximations are the local-density approximation (LDA) introduced by Kohn and Sham [120] and generalized-gradient approximation (GGA) [121]

The principle assumption of LDA is that for each infinitesimal element of density $\rho(r)dr$ the exchange-correlation density is that of a uniform electron gas of density $\rho = \rho(r) = n \uparrow + n \downarrow$ (density of electrons with upward spin, $n \uparrow$, plus the density of the electrons with downward spin $n \downarrow$). Here can be presented as

$$E_{XC}^{LDA} = \int d^3r \rho(r) \epsilon_{xc}(\rho(r)) \tag{3.17}$$

Where ϵ_{xc} is the exchange-correlation energy per electron in a uniform gas of density ρ. While LDA is clearly wrong because the charge density is highly non-uniform around atoms, the uniform electron gas is the only system for which can be calculated from which $\epsilon_{xc}(\rho(r))$ can be constructed [122]. Although LDA has shown accurate calculations in many cases for some systems including the cases where the electron density changes rapidly, it does a poor approximation due to ignoring spatial variations in the density. Generalized-gradient approximations (GGA) which have been developed to overcome this deficiency, include the dependence of the approximation on the gradient of the density. Using GGA the binding prediction and the dissociation energies specifically for hydrogen containing systems [123], improves. The GGA approximation can be presented as

$$E_{XC}^{GGA}[n \uparrow, n \downarrow] = \int d^3r \epsilon_{xc}(n \uparrow, n \downarrow, \vec{\nabla} n \uparrow, \vec{\nabla} n \downarrow) \rho(\vec{r}) \tag{3.18}$$

In general, it is suggested that GGA can improve the computational accuracies for total energies, atomization energies, structural energy differences and energy barrier compared to LDA,

because the GGA functional depends on electron density and its gradient and it provides a better solution for the inhomogeneous electron densities. In spite of wide range of use of LDA and GGA functionals they are still far from the ideal calculation and Finding an accurate and universally applicable remains a great challenge in DFT [124]. Some modifications have been suggested for more complicated molecules and materials to improve the GGA calculations. Perdew and Wang [114] suggested to keep the positive features of local spin density while applying some inhomogeneity effects to generate PW91 functional. The limitation of the PW91 functional is the complications in the mathematical details which need to be defined carefully and the unclear relationship between the parameters. Perdew, Burke, and Ernzerhof provided the (PBE) functional [111] which is known to be efficient and accurate for structural properties but less accurate for estimating the other properties [125, 111, 115]. B3LYP, meta-GGA and B2PLYP are some other modifications for the DFT functionals. B3LYP is a hybrid DFT functional and is developed from combining GGA and HF. Meta-GGA is a more advanced version of GGA which contains higher derivatives. Grimme et al. [116, 126] proposed B2PLYP functional as the most advanced functional which has not been employed in any commercialized DFT package yet and can improve the energetic and spectroscopic properties.

k-points

Based on Blochs theorem the work function of the electrons in aperiodic system can be presented as

$$\Psi_{kn} = U_{kn} exp(ik.r) \tag{3.19}$$

Where U_{kn} is a periodic function and k is the k-point referring to all the values in the first Brillouin zone. Where the first Brillouin zone is the primitive cell in the reciprocal space and the reciprocal space in solidstate physics is the array of the reciprocal lattices. This theorem helps to simplify the Kohn-Sham theory for ground state calculation. Some of the most important of these simplifications include the electron-electron interactions mapping to non-interacting electron system, or considering periodicity for an infinite solid bulk system. The idea is to choose an appropriate supercell so that the Blochs theory can be applied even to aperiodic structures such

as surfaces. In DFT a supercell can be defined with vectors to show the required crystal structure and the atom positions in the cell [127]. The reciprocal space unit vectors are

$$\vec{b_1} = 2\pi \frac{a_2 \times a_3}{a_1.(a_2 \times a_3)} \tag{3.20}$$

$$\vec{b_2} = 2\pi \frac{a_2 \times a_1}{a_2.(a_3 \times a_1)} \tag{3.21}$$

$$\vec{b_3} = 2\pi \frac{a_1 \times a_2}{a_3.(a_1 \times a_2)} \tag{3.22}$$

Here a_1, a_2, a_3 are the vectors are the real space unit vectors. The real space lattice vector $\vec{R}$ and reciprocal lattice vector $\vec{k}$ can be presented as

$$\vec{R} = n_1 a_1 + n_2 a_2 + n_3 a_3 \tag{3.23}$$

$$\vec{k} = x_1 b_1 + x_2 b_2 + x_3 b_3 \tag{3.24}$$

In DFT calculations it is suggested that increasing the number of k-point, improves the accuracy of the computation but the drawback is that the computational time raises as well. When comparing the stability of several systems based on their energy state it is important to notice that consistent k-point values and similar lattice parameters are used [128].

Pseudo-potentials

In DFT for reducing the calculation expenses it is suggested to use pseudo-potential for the system which assumes that the change in the surrounding atoms only affects the valence electrons and does not have any effects on the nuclei and the core electrons. Eliminating the interactions other than the valence electrons in the bonding does not give the exact results compared to the Coulomb potential but it is generally accepted that the plane wave basis set can represent both the pseudo-potentials and pseudo-wave function. Also simplifying the solid-state calculations is another advantage of pseudo-potential calculations [129, 130].

Geometry optimizaion

The ground state energy of the system requires finding the equilibrium configuration of the atoms by geometry optimizing the structure. In geometry optimization the most stable state of the system is found and the corresponding total energy is used for other energy state calculations such as transition state (TS), formation energy and the reaction energy. One of the most common methods to represent the equilibrium state of the system with respect to the geometry optimization is the potential energy surfaces (PES). PES calculation is based on Born-Oppenheimer approximation which separates the motion of electrons and the nuclei and assumes a fixed position for the nuclei and finds the PES by solving the electronic structure of the system. In a PES graph the vertical axis is usually the energy of the system and the other axis represent different aspects of geometry like angles and distances between different parts of the system. PES can be used to calculate reaction energy barrier, formation energy and transition state [131]

3.1.2 Computational Methods

DFT calculations were performed to estiate the energy of the system in the most stable state using the DMol3 module in Materials Studio package (version 7.0, Accelrys Inc.) [132, 133]. Adsorption behavior of molecular nitrogen (N_2) and bulk interaction (structural stability) of both atomic and molecular nitrogen (N and N_2) on a Mg $4 \times 4 \times 2$ supercell with 30 $\mathring{A}$ vacuum space and coverage of 0.0625 monolayer (ML) were studied by treating exchange-corelation energy with PW91 functional in the GGA scheme. Impacts of different crystallographic surface structures were compared using the Mg systems with basal (0001), prism ($10\bar{1}0$), and pyramidal ($\bar{1}01\bar{1}$) surface planes. Figure **??** presents the DFT slab models with periodic boundary conditions containing (a)basal, (b)prism, (c)pyramidal surfaces, and (d)the schematic illustration for the positions of these planes in a hcp crystal structure. The double-numeric quality basis set plus polarization with all electron core treatment was utilize in our model. In all the computations, the Fermi smearing value of 0.007 Ha (1Ha=27.2114eV) and a real-space cutoff of 4.9 $\mathring{A}$ were used to improve the computational performance, and the self-consistent iteration tolerance of 10^{-6} was applied. The charge and spin was chosen to be 0.05 for density of mixing and the dipole slab correction was applied to accelerate the convergence. To represent the surface and bulk component of crystals, one bottom layer was

fixed and the rest of the layers were free to relax in all the geometry optimization computations. For the convergence condition in geometry optimizations, the tolerances were considered to be 10^{-5} Ha for energy, 2×10^{-3} $Ha/\mathring{A}$ for force gradient, and $5\times10^{-3}\mathring{A}$ for displacement. A ($2\times2\times1$) k-point set was used and the adsorption energy (E_ad) was calculated from the difference between the energies of the combined structure of Mg/N_2 molecule and the seperate structures of isolated adsorbent and adsorbate. In studying the adsorption behaviro of N_2 on different sites over the Mg surface, the vibrational frequencies for the surface-N_2 (ν_{N-S}) and the intermolecular N-N stretching modes (ν_{N-N}) were computed using a finite-difference method. During the vibrational computations, the Mg substarate was frozen while the N_2 molecule was free to vibrate in any direction. In addition to the adsorption behavior of liquid nitrogen onto the Mg alloy surfaces, the structural stability of Mg was evaluated by calculating the energy of the system with N_2 molecule or N element absorbed in the bulk material. The structural stability was studied by comparing the energies of the system for separate parted and the final combined configuration. The energy of N atom was treated as half of the total energy of N_2 molecule [134, 135].

The bulk diffusion of elemental N and molecular N_2 was studied by performing DFT computation using pure Mg and Mg alloy system containg Al. The initial $4\times4\times2$ supercell structures comprised of 64 atoms (pure Mg or Mg alloy with one Al atom in a substitutional position) were geometry optimized to start with respective equilibrium structures. The k-point for these calculations was set to $(2\times2\times2)$. The k-point mesh testing was conducted using various mesh sizes with the unit cell of Mg crystal for all the calculations and confirmed the consistancy in the results for energy within a tolerance of $\sim 0.002eV$.

Transition of nitrogen between two closest equivalent octahedral, tetrahedral, or substitutional neighboring positions requires overcoming the diffusion energy barrier. This energy barrier was estimated by calculating the transition state (TS) for the displacement of nitrogen between two neighboring equivalent positions. The starting and ending configurations of the atomistic structures containing nitrogen atoms/molecules have been geometry optimized with prescribed computation conditions seeking local energy minima. To improve the TS search procedure, a complete linear synchronous transit (LST)/quadratic synchronous transit (QST) calculation was performed. This method combines a linear or quadratic synchronous transit approach for the initial steps of optimzation with a quasi-Newtonian or eigenvector-following method for rapid convergence toward the

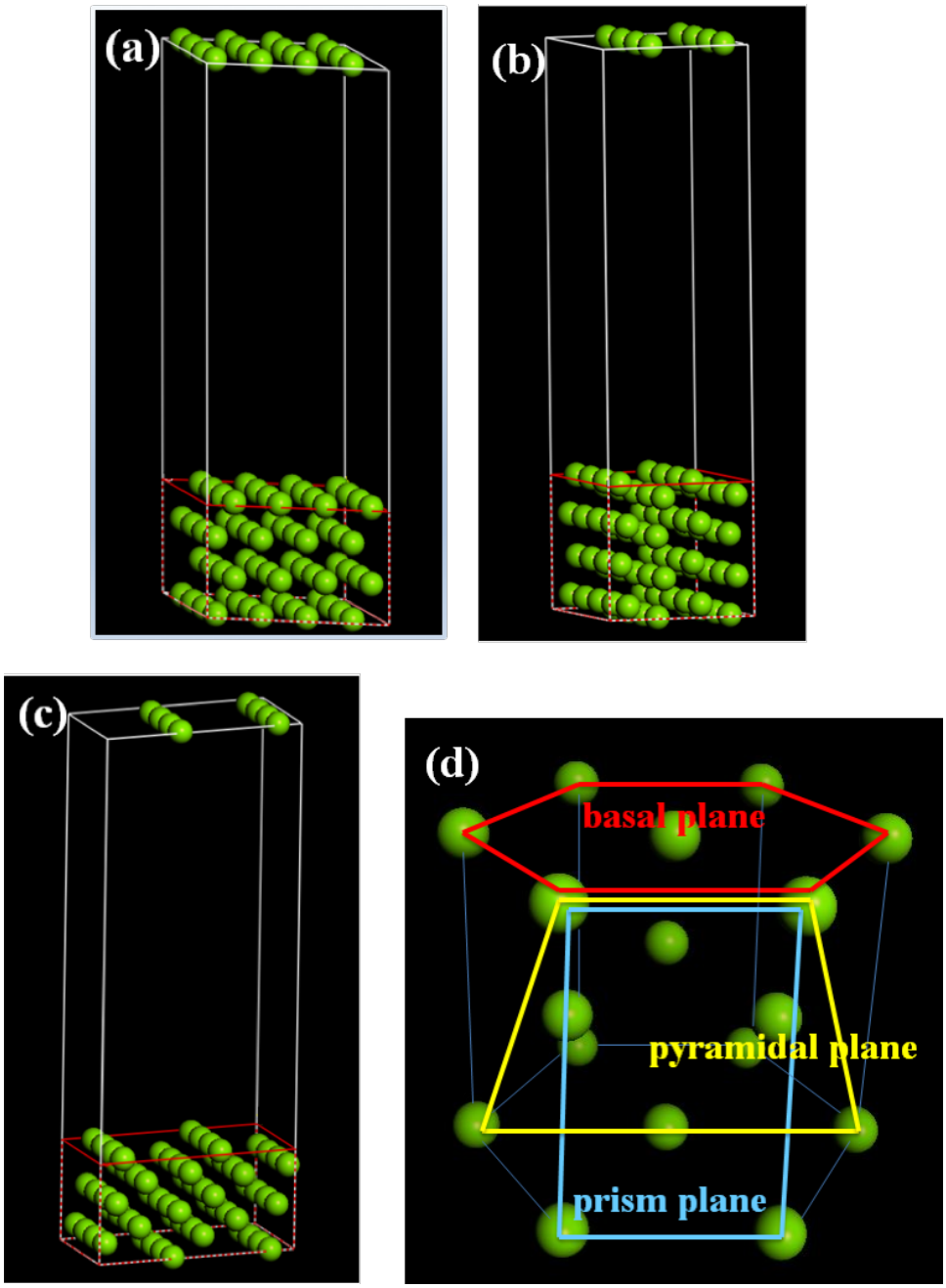

Figure 3.1: DFT slab models with periodic boundary conditions containing (a)(0001) basal, (b)$(10\bar{1}0)$ prism, and (c) $(\bar{1}01\bar{1})$ pyramidal surfaces, and (d) the schematic illustrations for the positions of these planes in a hpc crystal struucture.

end of the optimzation. The LST calculation estimates the TS by finding the highest point along the shortest line connecting two minim, while QST extends LST by subrsequently searching for the minimum along a line perpedicular to the previous one. Therefore, in QST, the parabolic path connecting the minima in conjunction with the found point may then be searched for a maximum

[136, 137, 138]. The LST/QST calculation was followed by nudged elastic band (NEB) method to find the minimum energy path (MEP) to confirm the TS calculations [139]. Since QST provides a relatively accurate guess for the MEP and enables the analysis of more complex path reactions, the QST results were used to find the TS and the MEP for the diffusion process. Nucleation of Mg nitrides (i.e.,Mg_3N_2) inside the lattice was simulated by implanting N atoms in the octahedral sites in the bulk lattice assuming a coherent interface for the early stages of nitride formation. The energies of pure Mg and optimized anti-C-type Mg_3N_2 with $Ia\bar{3}$ space group (i.e.,antibixbyite structure) were then compared. Since the atmospheric pressure in the cryomilling prcess would be in the order of approximately $\sim$ 1MPa and would not go beyond 20.6 GPa (the critical pressure for the transformation to anti-B-type structure), this antibixbyite structure is thought to present the stable structure for Mg_3N_2 during the cryomilling process [140].

Due to sensivity of the Mg to corrosion, attempts were made to study the corrosion behavior of pure Mg metal and Mg surface alloyed with Al, Ca, Zn or Y. Corrosion studies in this work were performed under two main categories:a) water adsorption on the metal surface b)dissolution behavior of the metal surfaces. Effects of crystallographic orientation and composition on the water molecule adsorption and the dissolution were studied by optimizing the slab surface cleaved to basal, prism and pyramidal planes. The electrode dissolution potential of the Mg/Mg alloys were quantifies by calculating the electrochemical potential difference between the alloy and pure Mg systems. The electrod potential difference was predicted based on the calculation of chemical potentials from the perfect Mg/Mg alloy surfaces and the surfaces with one or two point defects (i.e,vacancies). The detailed procedures applied to obtain the electrode potential difference are further described in the 'Result and Discussion' section.

The DFT calculations for Al-based systems were performed using same methods and software as Mg-based system were used. Since corrosion is not a critical issue with Al alloys this study does not cover the corrosion study caluculations and focuses on the interactions taking place in cryogenic atmosphere.

For the surface calculations including the adsorption energy and the dissociation energy evaluations, a $2 \times 2 \times 2$ Al(FCC) suppercell was cleaved to (100), (110) or (111) surface orientations, and they were doubled in their thicknesses to contain a total number of 64 atoms in the slab systems. To avoid undesired interactions due to periodic boundary conditions, a vacuum space of $30\mathring{A}$ was

added along the slab height direction. For the diffusion energy barrier calculations, $2 \times 3 \times 3$ supercells with 72 atoms were built to study the N_2/N transport between two sequential octahedral sites. We tested the stability of Al lattice structures including N_2/N in other potential interstitial locations such as tetrahedral sites. The diffusion of nitrogen species through adjacent octahedral sites were studied in this work, as these sites were identified as the most stable positions containing N_2 or N. The k-point meshed test confirmed that a k-point mesh of $2 \times 2 \times 4$ provides stable results for all the Al-based systems calculations. In addition to the pure Al system, to examine the impacts of common impurities in Al alloys, one atom of Mg, Mn, or Fe was placed at a substitutional site on the Al surface and in the Al bulk, for the adsorption and the diffusion energy barrier calculations, respectively. The positions of nitrogen species for both the surface and bulk calculations in the alloyed systems have been carefully chosen nearby the alloying elements intended to attain the hiest contribution from the impurity metal-nitrogen interactions.

3.2 Finite Elements Analysis

3.2.1 Computational Methods

A three-dimensional finite volume method was developed using ANSYS Fluent software. Figure 3.2 demonstrate the schematic diagram of SLM process involving melting and resolidification of the powder, considering the phase change phenomena due to heat exchange between the powder, laser and solid base. Thermal conduction is detected to be responsible for most of the heat transfer in the system, however the influence of convection and radiation cannot be ignored in the calculations. A 0.2 mm layer of powder is evenly distributed over a 0.5 mm thick slab. The whole system including powder and base plate consist of a $1mm \times 5mm \times 0.7mm$ block in X, Y and Z directions respectively. The laser scans the top XY surface as demonstrated in Figure 3.2 (a) and moves in positive Y direction. The calculations are carried out with a uniform structured mesh composed of 64000 hexahedral cells, with $15.625 \times 10^{-6} mm^3$ sizes, which are optimized for obtaining a compromise of computation time and accuracy as demonstrated in Figure 3.2 (b). The powder material is considered to be AlSi10Mg/AlN composite and the base solid is considered to be AlSi10Mg with composition and materials properties detailed in tables 3.1 and 3.2 and Figure 3.3.

Table 3.1: AlSi10Mg chemical composition in wt% [11]

Si	Mg	Fe	Mn	Ti	Zn	Ni	Cu	Pb	Sn	Others	Al
9-11	0.2-0.45	<0.55	<0.45	<0.15	<0.1	<0.05	<0.05	<0.05	<0.05	Others	balance

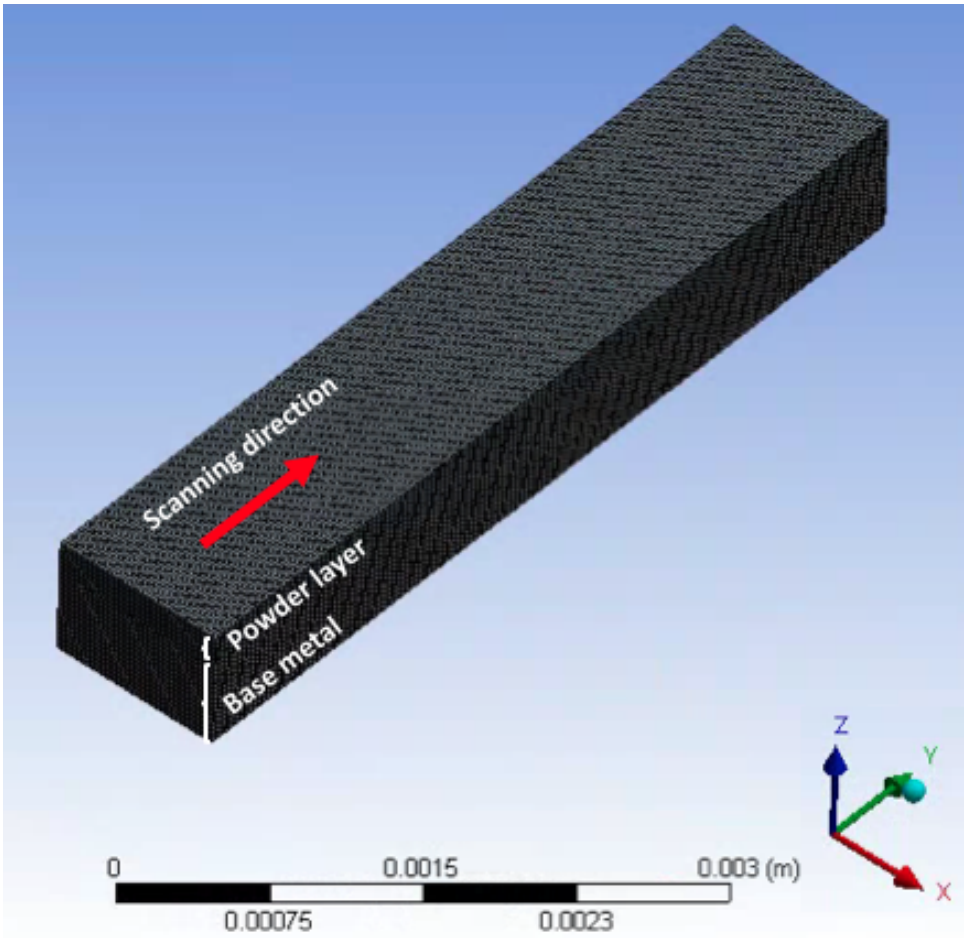

Figure 3.2: Demosntration of the geometry and mesh for the studied SLM process

Governing Equations and boundary conditions

During the SLM process a laser beam provides the heat to system causing the fusion in powder and base material if the input energy is adequate. A Gaussian distribution is considered for the heat source with the mathematical formula as equation 3.25 [146]:

$$q = \frac{2AP}{\pi R^2} exp\left(-\frac{2r^2}{R^2}\right) \tag{3.25}$$

Where A is the laser energy absorbance of the powder, P is the laser power, R is the effective

Table 3.2: Materials properties and theoretical parameters for selective laser melting

Parameter	Value	Reference
Initial temperature, T_0	298, 373, 473 K	
Laser power, P	100, 150, 200 W	
Scan speed, V	100, 150, 200 mm/s	
Radius of laser beam, ω	35 μ m	
Powder porosity	0.4	
Powder layer thickness, t_{layer}	0.2 mm	
Laser absorptivity of AlSi10Mg powder,	0.09 N/m	[141]
Solidus temperature, T_s	830 K	[142]
Liquidus temperature, T_l	867 K	[142]
Latent heat of fusion of AlSi10Mg, H	389 kJ/kg	[143]
Density of AlSi10Mg powder, ρ	2650 kg/m^3	[144]
Viscosity	1.3×10^{-3} $Pa.s$	[145]

laser beam radius at which the energy density reduces to $\frac{1}{e^2}$ at the center of the laser spot, and r is the radial distance from a point on the powder bed surface to the center of the laser spot. A Volume of Fluid (VOF) model was combined with solidification and melting model to consider detailed phase change from porous powder to liquid and eventually to solid. To define the latent heat required for solidification and melting exchange enthalpy was described as a function of temperature as in equation 3.26. Where ρ is the density, c represents the specific heat capacity and T is the temperature.

$$H = \int \rho c dT \tag{3.26}$$

As the laser beam irradiates the top surface of the powder a fraction of the energy is reflected and the rest is absorbed causing temperature raise in the powder bed and eventually melting of the powder and depending to the density of input energy, melting of the base solid.

The spatial and temporal distribution of the temperature field is expressed with equation 3.27 in 3D:

$$\rho c \frac{\partial T}{\partial t} = \frac{\partial}{\partial x}\left(k\frac{\partial T}{\partial x}\right) + \frac{\partial}{\partial y}\left(k\frac{\partial T}{\partial y}\right) + \frac{\partial}{\partial z}\left(k\frac{\partial T}{\partial z}\right) + Q \tag{3.27}$$

Where k is the thermal conductivity and Q is heat generated per volume. Equation 3.28 can specifically define the initial condition for the temperature distribution in the powder bed at time

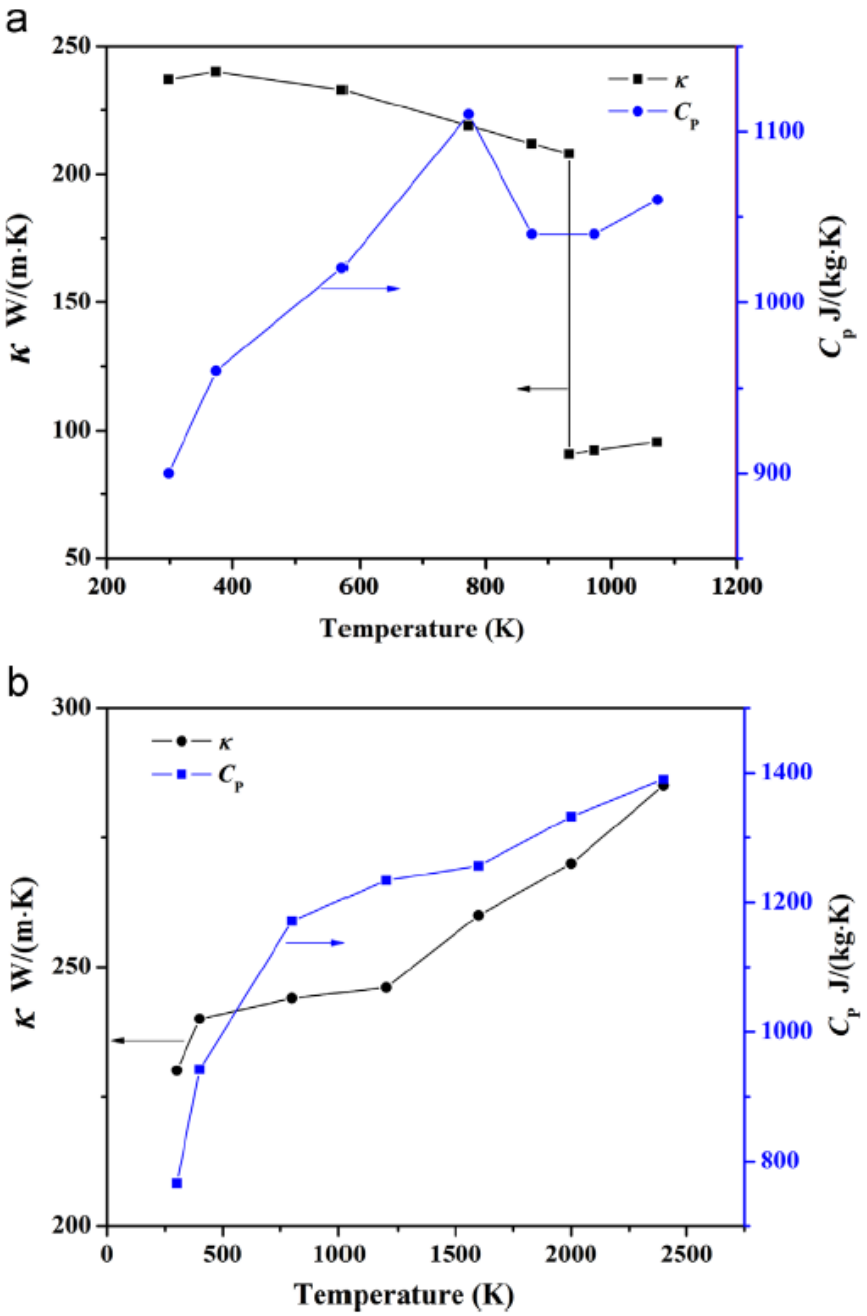

Figure 3.3: AlSi10Mg/AlN composite materials properties (a) thermal conductivity and specifica heat at constant pressure for AlSi10Mg alloys (b) thermal conductivity and specifica heat at constant pressure for AlN particles [11, 12]

t=0.

$$T(x,y,z,t)|_(t=0) = T_0(x,y,z) \in D \tag{3.28}$$

Where T_0 is the initial temperature and varies from 298 K to 373 and 473 K. And the natural boundary condition on the surface (S) with normal n, where the heat flux is imposed, is defined as equation 3.29.

$$k\frac{\partial T}{\partial n} - q + q_c + q_r = 0(x, y, z) \in S \tag{3.29}$$

In this equation q is the input heat flux with the Gaussian distribution as defined earlier. q_c is the heat convection and q_r is the heat radiation.

$$q_c = h(T - T_0) \tag{3.30}$$

$$q_r = \sigma\epsilon(T^4 - T_0^4) \tag{3.31}$$

h is the coefficient of heat convection and σ is the Stefan-Boltzman constant and ϵ is the emissivity. In this model during the melting process thermal properties of the powder and base solid such as thermal conductivity and specific heat capacity are temperature dependent.

3.2.2 Design of Experiment

Design of experiment (DOE) approach was utilized to explain the variation of sintering quality during the selective laser melting process and identify the key parameters and interdependencies with a minimal amount of data. Various experimental process parameters affect the quality of final product, among which the most important ones are laser scanning speed, powder bed initial temperature and laser power. Taguchi methods [147] were devoted for experimental design in this work. In Taguchi Design of Experiments all experiments are planned a priori and the results are analyzed after completing all the experiments. The experiments in this research have been designed using an L9 orthogonal array (OA), conducted in an ordered manner and then the outcome results were analyzed statistically using ANOVA to find the best combination of parameter levels. Table 3.3 lists all the runs performed for the L9 orthogonal array. Three different levels have been considered for each independent variable (i.e. laser scanning speed 100, 150 and 200 mm/s, laser power with 100, 150 and 200 W and initial powder bed temperature equal to 298, 373 and 473 K.

Table 3.3: Taguchi design of experiment. L9 orthogonal array.

Run No.	Speed (mm/s)	Laser power (W)	Powder bed temperature (K)
1	100	100	298
2	100	150	373
3	100	200	473
4	150	100	373
5	150	150	473
6	150	200	298
7	200	100	473
8	200	150	298
9	200	200	373

Maximum temperature and geometry of the melt pool, and velocity of the solidification front were recognized as the response values identifying the quality of the final product. The signal to noise ratio and other parameters used in ANOVA are calculated by the following equations [148]:

$$\frac{S}{N_i} = -10log\left(\frac{1}{n}\Sigma_{i=1}^{n}\frac{1}{y_i^2}\right) \tag{3.32}$$

$$S_m = \frac{\left(\Sigma_{i=1}^{9}\eta_i\right)^2}{9} \tag{3.33}$$

$$S_A = \frac{\left(\Sigma_{i=1}^{3}\eta_{A_i}\right)^2}{N}S_m \tag{3.34}$$

$$S_T = \Sigma_{i=1}^{9}\eta_i^2 S_m \tag{3.35}$$

$$S_E = S_T \Sigma S_A \tag{3.36}$$

Where the various kinds of A (control factor) are laser scanning speed, laser powder and initial temperature of the powder and n is degree of freedom and is equal to 2 in this work. y_i is the measured characteristic, maximum melt pool temperature and geometry, and solidification front velocity, S_m is the average of the squares of the sums, S_A is the sum of squares correlated to the control factor A, S_T sum of squares of the variance and S_E is sum of squares of the errors correlated to all controlled factors.

After collecting the response values based on the control factors, a main factor effect plot is concluded. The slope of the plot reveals if the control factor has significant effect on the response value. A horizontal line is interpreted to no main effect, while as the slope is steeper the main effect present has a greater magnitude.

Chapter 4

Result and discussion

4.1 Mg cryomilling

Developing advanced alloy systems with high strength-to weight ratios is the center of attention especially for structural material sectors including automotive, aerospace, and military applications. Mg nanocrystalline alloys with low density and good machinability have claimed to provide much improved mechanical properties in presence of alloying elements such as Al, Zn, Si, Mn, and Y in their composition. More recent researches revealed that the addition of discontinuous particles in the form of nanosized reinforcement particles has a high potential to enhance the mechanical properties by improving the modulus, the strength, and the ductility of materials. In these metal-matrix nano composites (MMNCs), the volume fraction, the shape, the size, and the orientation of the reinforcement particles can strongly affect the strengthening improvement of materials. Cryomilling, particularly under liquid nitrogen environments, is often employed in PM synthesis because it has a high potential to produce finer grain sizes compared with conventional ball milling. The liquid nitrogen atmosphere is intended (1) to decrease the milling time needed to achieve the desired fine particle size while minimizing powder agglomeration and welding to the milling media, (2) to minimize the oxidation reaction during the process, and (3) to prevent dynamic recovery and recrystallization [149]. In addition to these benefits, the cryomilling process can introduce nitrogen-based impurities to the matrix, which can act to stabilize the microstructure of the material by pinning dislocations and by activating Orowan strengthening mechanisms [55, 150, 151, 152]. The Orowan strengthening mechanism is activated when these secondary precipitates are homoge-

neously dispersed inside the grains and are sufficiently small [75]. Although it is known that the nitrogen molecule has a considerable reactivity with Mg powder [153] and that the free energy of formation of Mg nitride (Mg_3N_2) is negative (-400.83 kJ/mol) [154], the presence of Mg nitride in the Mg nanocrystalline materials synthesized via cryomilling processing has not yet been clearly confirmed and the atomistic interaction between nitrogen species and bulk Mg lattices has not been systematically explored [155, 156, 157]. The low temperature of the cryomilling process decreases the reactivity between liquid nitrogen and Mg powder, unless the mechanical forces from milling break the triple bonding of N_2 and result in nitride formation. On the other hand, the diffusion of the nitrogen into the bulk will increase the possibility of nitride formation by increasing the contact between the nitrogen and the metal atoms. It is expected that nitride formation would be achieved on the surface of grains and that the formed nitrides would be mechanically forced inside the bulk lattice of Mg/Mg alloys [155, 150, 158, 127]. It is, therefore, pivotal to understand the interactions between nitrogen species and lattice atoms below the surface, because the formation and dense segregation of nitride particles along the grain boundaries/surfaces of the synthesized Mg/Mg alloys are generally believed to deteriorate the mechanical properties. With this, in the present study, we attempted to address the following questions; (1) what is the mechanism and what are the activation energy barriers of nitrogen diffusion in the Mg matrix during the cryomilling process?, and (2) what is the formation energy and the type of N-rich dispersoids?

To answer these, we majorly focused on the quantification of nitrogen molecule adsorption and absorption on the Mg-based surfaces, bulk diffusion energy barriers of various diffusion routes in pure Mg and Mg alloy lattices using density-functional theory (DFT) computational technique.

4.1.1 Nitrogen adsorption on Mg surface

The reported experimental value of N_2 dissociation energy is 942 kJ/mol[159]. Because this dissociation energy of triple-bonded N_2 molecule is very high, nitrogen is more likely to be adsorbed in the molecular form rather than the elemental form. To confirm the experimental finding of the N_2 dissociation energy and to validate the computation in the present study, we have performed the simple DFT calculation to estimate the dissociation energy of N_2 molecule. The dissociation energy (D°) for $AB \longrightarrow A+B$ reaction can be calculated from $D^\circ = \Delta Hf_0^\circ(A) + \Delta Hf_0^\circ(B) - \Delta Hf_0^\circ(AB)$, where $\Delta Hf_0^\circ(X)$ represents the formation enthalpy of "X" compound or element. Our calculation

based on the single isolated N_2 molecule with the computational parameters given above predicted that the dissociation energy is $D^\circ = 995$ kJ/mol, which only shows about $\sim 5(\%)$ difference with the reported experimental value [159].

Given the high dissociation energy required for bond breaking of N_2 molecules, we first focused on the adsorption phenomena of N_2 molecule over the Mg/Mg alloy surface. Computation of the binding energy (i.e., adsorption energy, E_{ad}) is the most widely used scheme to quantify the tendency of adsorption in many systems. The binding energy can be obtained by,

$$E_{ad} = E_f - E_{slab} - E_{N_2} \tag{4.1}$$

Where E_{ad} is the adsorption energy, E_f is the total energy of the Mg/Mg alloy systems containing an N_2 molecule, E_{N_2} is the total energy of Mg/Mg alloy slab systems without N_2 molecule, and E_{N_2} is the energy of an isolated nitrogen molecule, respectively. For our computation, first, the vertical position (i.e., z-coordinate) of an N_2 molecule was adjusted to obtain the preferred adsorption site by geometry optimization. After the preferred vertical position of a nitrogen molecule was identified for each system, the vertical position of the N_2 molecule was fixed and all other coordinates were relaxed. Starting from the preferred vertical site, an N_2 molecule was located on top of the pure Mg or Mg alloy surface. We used $(4 \times 4 \times 2)$ super-cell structures for all of nitrogen molecule adsorption simulations, and one center Mg atom on the surface was replaced by one of the three alloying elements for Mg alloys. The initial in-plane sites (i.e., x- and y-coordinates) of the nitrogen molecule were varied to explore the minimum energy status of the slab systems. For studying the effects of alloying elements, alloying atoms with the coverage of 0.0625 ML have been doped on the top surface layer, as shown in Figure 4.1(a). Figure 4.1(a) illustrates a top-view example of the DFT slab model with an Al impurity element containing nitrogen molecules over the basal plane of Mg-Al alloy. Here, the N, Mg, and Al atoms are colored as blue, green, and magenta spheres, respectively. The shaded spheres (dark green spheres) in Figure 4.1(a) are the Mg atoms positioned in the 2^{nd} layer from the surface.

For the adsorption sites of the N_2 molecule on the pure Mg surface, four representative high-symmetric positions including the "atop" (on top of an Mg atom), the "bridge" (on the middle point of two neighboring Mg atoms), and the "hollow 1" and the "hollow 2" (on the center of three

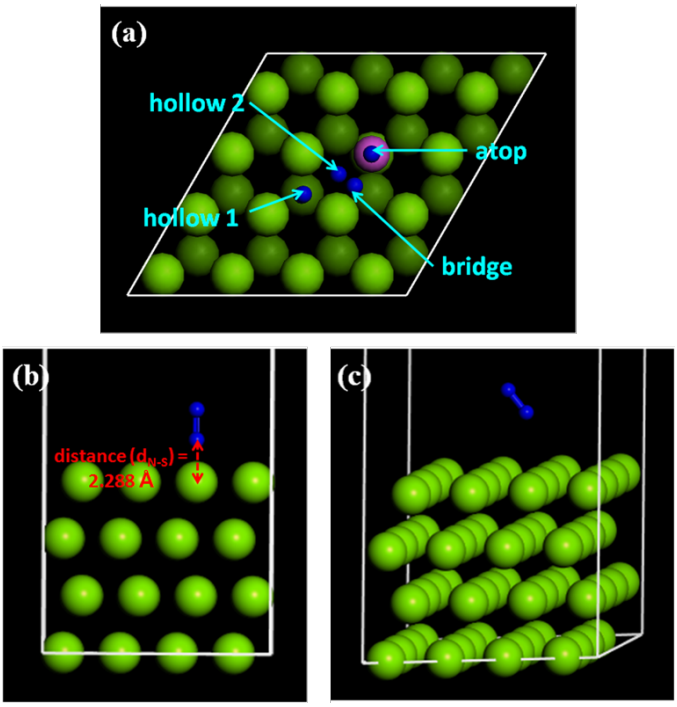

Figure 4.1: (a)The four representative adsorption sites on the Mg surface, and the geometry optimized structures of (b) the atop and (c) the bridge sites in the pure Mg materials with basal surface plane

triangular Mg atoms) sites have been considered. The hollow 1 site differs from the hollow 2 site by the existence of the Mg atoms (i.e., the "B" atoms in the ABABAB hcp stacking sequence) in the 2^{nd} layer from the surface. These four representative binding sites are also illustrated in Figure 4.1 (a). As shown in Figure 4.1 (b), the geometry optimization of the systems for all of the positions except the bridge site generated the stable N_2 molecule with the vertical orientation (vertical alignment). The vertical distance (d_{N-S}) from the Mg surface atom to the nitrogen molecule in the most stable condition was 2.288 A° when the nitrogen molecule is located on top of surface Mg atom (i.e., "atop" position). The N_2 molecule in the bridge site, on the other hand, shows the highest stability of the configuration with a tilted alignment of the N_2 triple bond with reference to the Mg metal surface as presented in Figure 4.1 (c). This is presumably derived from the attractive interaction between the nitrogen element and the Mg atom in the 2^{nd} layer from the surface; as depicted in Figure 4.1 (a), the bridge site is asymmetrically positioned above the 2^{nd} layer (shaded green atoms) along the unit cell lattice line. Figure 4.2 shows the relative total energy differences in the system during the configuration changes of N_2 molecule when the computation was performed with the atop site. The

orientation of N_2 bonding has been altered from the horizontal alignment to the vertical alignment with the transition state (TS) coordinate in Figure 4.2. Assuming that the liquid N_2 molecules can have random orientation over the Mg surface, initial configuration of horizontal orientation was selected to estimate the maximum energy barrier for molecular rotation over the atop site. The transition state coordinate is arbitrarily chosen (i.e., no units). The triple-bond alignment angles with reference to the surface plane are also given in the Figure. These calculation results imply that when the N_2 triple-bonding orientation is changed from the horizontal to the vertical configurations, the highest system energy is observed at the system with $\sim 18^\circ$ alignment angle, and ~ 0.02 eV of transition energy barrier must be overcome.

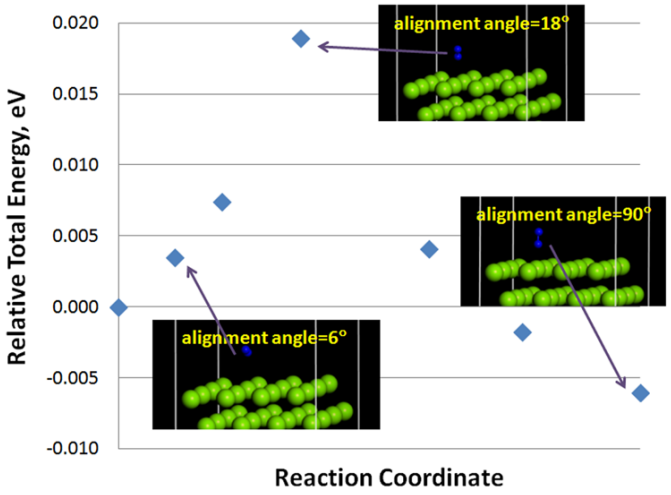

Figure 4.2: Relative total energy difference of pure Mg system containing a N_2 molecule in the atop site with various triple-bond alignment configurations

The electronic spectrum of N_2 with occupation of the bonding 3σ orbital by paired electrons results in a diamagnetic molecule. It was found that the diamagnetic N_2 molecule has a weak attraction to the non-magnetic Mg surface based on the current DFT calculation of the adsorption energies for different positions, alloying elements, and crystallographic orientation. This weak attraction even varies with the adsorption site locations. Table 4.1 summarizes the calculated adsorption energy, N-N triple-bond length, N_2 surface bond length and the vibrational frequencies of N-N bond ($\nu N-N$) and N_2-surface ($\nu N-S$) of N_2 molecule on Mg surface. In the contour map of Figure 4.3, we present the calculation results of the in-plane binding energy of N_2 with various adsorption sites on the pure Mg. In the figure, the closed and dashed circles respectively denote the

positions of Mg atoms on the outermost surface and the next layer. From these table and figure, it is clearly seen that the atop site (=-0.0886 eV) is the most preferential position for the N_2 with the lowest binding energy followed by the bridge ($E_{ad} = -0.0547eV$), hollow 1 ($E_{ad} = -0.0459eV$) and hollow 2 ($E_{ad} = -0.0434eV$) sites. Note that the minimum binding energy of pure Mg surface ($atopposition, E_{ad} = -0.0886eV$) is lower than the calculated binding energy of the pure Al system ($E_{ad} = -0.038eV on (111) surface of pure Al$), which indicates that pure Mg can attract the liquid N_2 molecule more easily in a thermodynamic sense than pure Al. The binding energy onto (111) Al surface was calculated using the identical procedures and computation parameters except the k-point set ($(6 \times 6 \times 1)$ for Al) provided in the 2. Computational Methods section. Because the diffusion path of atop-bridge-atop would require only 0.034 eV, it is expected that the N_2 adsorption can be achieved by this path. It should be mentioned that the vertical distance between the metal surface and the molecule (d_{N-S}) increases from atop position to the bridge site and then the hollow sites due to the steric and bond-order conservation arguments which explains that the distance between the metal and the nitrogen would increase with the possible number of adsorbate-substrate bonds. The triple-bond lengths (d_{N-N}) between two N atoms for all cases are greater than the bond length of isolated N_2 ($1.107A^\circ$). d_{N-N} becomes relatively larger for the atop site due to the strong interaction of the molecule with the surface. Comparing ν_{N-N} values for the N_2 for different adsorption sites clarifies that atop position not only has the lowest adsorption energy and the distance with the N_2 molecule, but also the lowest vibrational frequency and longest triple bonding length, which would lead to the consequent highest stability among the studied binding sites. As it is expected that, by increasing the distance between two N atoms the corresponding vibrational frequency decreases, the lowest ν_{N-N} with bond length of $1.122A^\circ$ for the atop position was predicted. In addition, it is seen that d_{N-N} slightly increases and ν_{N-N} decreases when the N_2 molecule moves from the bridge to hollow sites, respectively. The experimental bond length and stretching frequency for the free N_2 are $1.098A^\circ$ and $2331cm^{-1}$ respectively [139]. In our calculation, the corresponding values from DFT are $1.107A^\circ$ and $2369.4cm^{-1}$, respectively, which demonstrate the rigor and the reliability of our calculations. Here, the frequency is given by the energy of photons absorbed to cause molecular vibrations in a wavelength unit. From Table 4.1, calculated ν_{N-N} results of N_2 molecules on Mg surface show that the frequency decreases by adsorption to the metal surface compared to the free nitrogen with no interaction to the surface

($\nu_{N-N} = 2369.4 cm^{-1}$).

Table 4.1: Calculated binding energies (E_{ad}), surface-nitrogen distance (d_{N-S}), nitrogen bond length (d_{N-N}), vibrational frequencies of N_2 triple bonding (ν_{N-N}) and the surface-nitrogen atoms (ν_{N-S}) for an N_2 molecule at different sites over the basal surface plane of Mg

Surface planes	Alloying elements	position of N_2	E_ad (eV)	d_{N-S} (Å)	d_{N-N} (Å)	ν_{N-N} (cm^{-1})	ν_{N-S} (cm^{-1})
Basal	None	Atop	−0.0886	2.288	1.122	2128.5	231.1
		Bridge	−0.0547	3.651	1.109	2298.9	218.3
		Hollow 1	−0.0459	3.755	1.110	2287.9	269.4
		Hollow 2	−0.0434	3.789	1.111	2273.0	270.2

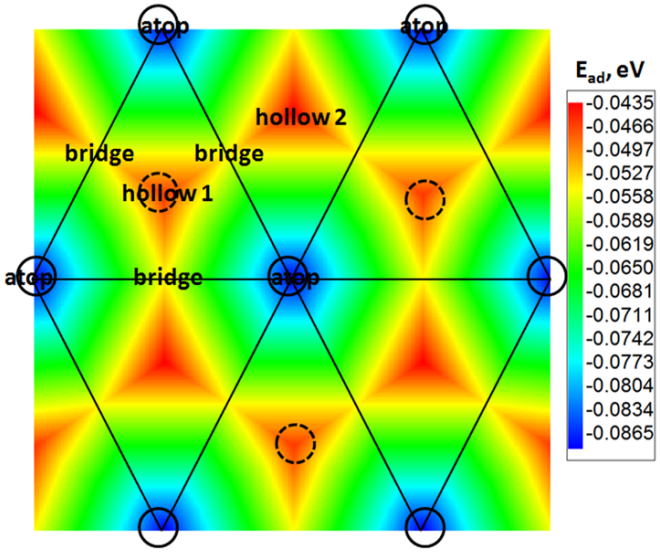

Figure 4.3: Contour map of the adsorption energy for N_2 molecule on the basal plane of pure Mg. Closed circle and dashed circle denote the position of Mg atoms on the outermost surface and the next layer (i.e., 2^{nd} layer) from the surface, respectively

4.1.2 From absorption to bulk interaction of nitrogen in Mg lattice

Finding the minimum energy path of a reaction is an important approach for studying the reactivity of the process. In this work, we have applied the nudged elastic band (NEB) method to find the minimum energy path for the process and to define the N_2 dissociation path and transport barriers [139]. To perform an NEB calculation for the interaction of the nitrogen with the pure Mg, an N_2 molecule was equilibrated on the atop position of pure Mg surface as the initial structure (i.e., reactant). For the final structure (i.e., product), two separated nitrogen atoms that had diffused inside the Mg bulk after the geometry optimization were used. Considering these two structures as

the reactant and the product of the reaction, a global TS search based on the linear synchronous transit/quadratic synchronous transit(LST/QST) calculation was performed starting with pairing the equivalent atoms in two structures. To assure that the calculated transition state (TS) connects the reactant and product, the NEB calculation using TS confirmation was applied to the system. In the current work, at least five energy path estimates for the TS were tested and the minimum energy path was selected. Figure 4.4 shows the calculated relative total energy change from the geometry optimized state of N_2 molecule in the atop site to a final imaginary state of two elemental N atoms underneath the surface. The final state was obtained by performing geometry optimization computation of two isolated N atoms underneath the Mg surface. This TS calculation was intended to predict the energy barrier of N_2 molecule dissociation over the Mg surface that will be diffused into the bulk region during the cryomilling process. In the figure, the total energy of the initial state was set to 0 and the relative energy changes are plotted along an arbitrary transition state coordinate. The vertical distance from the surface to the N_2 molecule (d_{N-S}) was calculated from the difference between the z-coordinate values of the surface Mg atom and the lower N atom. dN-S decreases from the equilibrium value of $2.288A^\circ$ to $-1.049A^\circ$, where the negative sign of d_{N-S} indicates that the N atoms are positioned inside the bulk Mg region. These transition state (TS) calculations predict that the energy barrier for the dissociation of N_2 molecule and diffusion into the bulk Mg requires 1.13 eV (i.e., $\sim$ 110 kJ/mol), which is about 9 times lower than the triple-bond breaking energy of a single N_2 molecule. However, if Boltzmann distribution (probability $\propto e^{\frac{-DeltaE}{k_BT}}$, where ΔE, k_B, and T are the energy difference, Boltzmann constant, and absolute temperature, respectively) for this phenomenon of bond breaking and diffusion into the bulk is considered, the probability is still nearly 0 (i.e., $\sim 10-64$ at 90 K). It is, therefore, likely that the N_2 liquid would remain in their molecular form unless a very high external energy is provided during the milling process. Currently, it is our understanding that there are no available experimental or theoretical data about the kinetic energies for Mg materials. Despite this energy barrier, the total energy of a system with separated N atoms showed a lower value, which implies that the isolated N atoms are more stable inside the bulk region of Mg once the N_2 bond is broken up. If there are N atoms in the Mg lattice, they have been likely broken up near the Mg surface as the dissociation energy of free N_2 molecules is much higher (i.e., 995 kJ/mol by our calculation).

Table 4.2 summarizes the results of calculated binding energies (E_{ad}), surface-nitrogen distance

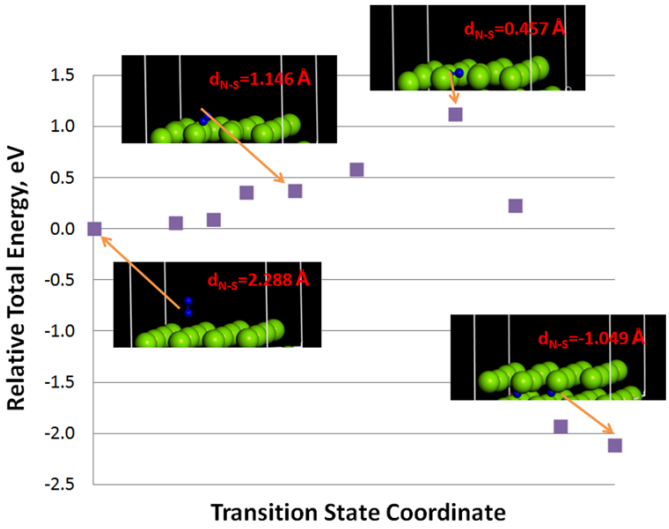

Figure 4.4: Relative total energy difference of pure Mg system containing a N_2 molecule in the atop site with various triple-bond alignment configurations

Table 4.2: Calculated binding energies E_{ad}, surface-nitrogen distance (d_{N-S}), and nitrogen bond length (d_{N-N}) for Mg systems with different surface planes, alloying elements, and N_2 positions.

Surface planes	Alloying elements	position of N_2	E_ad (eV)	d_{N-S} ($\AA$)	d_{N-N} ($\AA$)
Basal	None	On top of Mg	−0.0886	2.288	1.122
	Al	On top of Mg	−0.0893	2.292	1.122
	Zn	On top of Mg	−0.0906	2.286	1.122
	Y	On top of Mg	−0.0563	2.322	1.120
	Al	On top of Al	−0.0245	4.178	1.107
	Zn	On top of Zn	−0.0441	3.947	1.108
	Y	On top of Y	−0.6200	2.434	1.126
Prism	None	On top of Mg	−0.1453	1.123	2.245
Pyramidal	None	On top of Mg	−0.1953	1.127	2.203

(d_{N-S}), and nitrogen bond length (d_{N-N}) for Mg systems with different surface planes, alloying elements, and N_2 positions. As explained before, addition of common Al, Zn, and Y elements on the substitutional surface position was considered in this work. The atop site of N_2 adsorption was selected for all of the calculations as it showed the lowest energy of the pure Mg system. From the table, it was found that incorporation of Al and Zn shows similar effect on the N_2 binding energies of the system. When Al or Zn atoms are present on the surface of Mg alloys, the adsorption of liquid nitrogen will occur through the atop site over the Mg surface atom with relatively same binding energy with that of pure Mg system. Adsorption on the Al or Zn will be less likely to occur as the binding energy is much larger, which implied that addition of Al or Zn

would reduce the N_2 adsorption tendency of the Mg alloys during the cryomilling process. When Y atom is doped on the surface, on the other hand, the binding strength of N_2 molecule can be substantially increased through the adsorption over the Y surface atoms; for the atop configuration over Y atom is equivalent to -0.6200 eV that is about 7 times lower than the binding energy for the same configuration of pure Mg ($E_{ad} = -0.0886eV$). Thus, it is expected that the liquid nitrogen adsorption would be strongly enhanced by the surface alloying of Y. Therefore, as long as the surface energies of alloying Y is not high and there are Y impurities on the Mg surface, compared with other types of Mg alloys, Mg alloys containing Y (such as WE43) would show much stronger tendency to capture the N_2 molecules. The surface orientation also impacts the binding tendency of N_2 molecules. Although the grain boundary and interface character distributions of nano Mg/Mg alloys synthesized from PM are not known, considering the surface energies of different orientations, it is expected that relatively much higher population would be observed. The calculated results in Table 4.2 clearly show that, values associated with the prism $(10\bar{1}0)$ and pyramidal $(\bar{1}01\bar{1})$ surface planes are considerably lower than the binding energy from the basal surface, which indicates that attracting N_2 molecules could be facilitated by forming the less popular high energy surfaces.

Stability of nitrogen in Mg/Mg alloy

Next, we have examined the absorption behavior of N_2 molecule or N atom into the bulk lattice of pure Mg. Although we have shown that it would require a very high energy to break the triple-bond of an N_2 and to diffuse them into the lattice, the adsorption behaviors of both the N_2 and N absorbate types are studied for some special cases of interest. In Table 4.3, the results of absorption energies for the situations studied in the present work are summarized. We first have considered the stability of the N_2 and N absorbate in the vacancy lattice of Mg atom, because it was previously reported that the existence of vacancy sites is important in the lattice absorption and diffusion of nitrogen species in Al/Al_2O_3 nanocomposites [160]. When a vacancy site of Mg atom was occupied by an N_2 molecule or an N atom, these absorbates showed instability such that they would diffuse out of the original location and move to an interstitial position or they would move out of the bulk lattice (N_2 in the vacancy site on the surface), as summarized in Table 4.3. These instability phenomena happened regardless of the vacancy positions (in the surface or in the $2_n d$ layer from the surface).

Table 4.3: Calculated absorption energies (eV) of N and N_2 in the Mg system with and without a vacancy site.

Absorbate type	Existence of vacancy	Absorption site	Absorption energy (eV)
N_2	Yes	Mg vacancy on the surface	Unstable, moves out of surface
	Yes	Mg vacancy in the 2nd layer	Unstable, moves to interstitial position
	No	Tetrahedral site between the surface and the 2nd layer	−0.2269
	No	Tetrahedral site between the 2nd and 3rd layer	−0.2767
N	Yes	Mg vacancy on the surface	Unstable, diffuses into the lattice
	Yes	Mg vacancy in the 2nd layer	Unstable, diffuses into the lattice
	No	Tetrahedral site between the surface and the 2nd layer	−6.2182
	No	Tetrahedral site between the 2nd and the 3rd layer	−6.3673

We then studied the lattice diffusion of the absorbates through the interstitial sites. The N_2/N absorption energies of the tetrahedral sites of hcp Mg crystals are shown in Table 4.3. In contrast to the cases in which the absorbates were occupied in the vacancy sites, when the absorbates are positioned in one of the interstitial sites, the systems showed much higher stability. For example, the absorption energies are calculated as -0.2262 and -6.2182 eV for N_2 molecule and N atom, respectively, when the tetrahedral sites between the surface and the 2^{nd} layer from the surface are occupied. The absorption energies of tetrahedral sites between the 2nd and the 3_{rd} layers from the surface showed similar but slightly lower values compared with the energies from the tetrahedral sites between the surface and the 2^{nd} layer. These two tetrahedral sites and the probable diffusion route are illustrated in Figure 4.5(a). Here, "A" and "B" positions denote the tetrahedral sites in the surface/2^{nd} layer and the $2^{nd}/3^{rd}$ layer, respectively. Using these "A" and "B" positions of N_2/N as the initial and final configurations, respectively, the transition state (TS) search and the corresponding total energy calculation were conducted, and the relative total energy changes are shown in Figure 4.5 (b). Several test trial calculations were conducted to find the minimum energy paths displayed in Figure 4.5(b). It is seen from these results that the energy barriers for N_2 and N through the tetrahedral sites are ~ 1.705 and $\sim 1.128eV$, respectively, which implies that, even for the N case, the lattice diffusion into the bulk Mg from the 2^{nd} layer to the 3^{rd} layer is as difficult as the N_2 dissociation over the Mg surface. To activate the solution strengthening and/or Orowan strengthening mechanism based on the N_2/N particles/dispersoids, therefore, these energies will be required to overcome the energy barrier when it is assumed that the N-rich dispersoids are formed near the surface of Mg matrix grains because it is expected that the N_2/N species collected in the Mg bulk during the milling process would be accumulated near the grain boundary area

of the synthesized nano alloys. Note that, other than the tetrahedral sites (T-sites), the stability in the octahedral site (O-sites) occupancy was also tested for N_2 and N. It was predicted that, however, these octahedral cases are not as stable as the tetrahedral cases (data not shown). From these results, it is expected that the N atom would display a higher stability than N_2 molecules in the Mg lattice near surface once it is formed during the PM process, although it is currently not experimentally clearly observed that individual N atoms exist in the Mg bulk lattice [160].

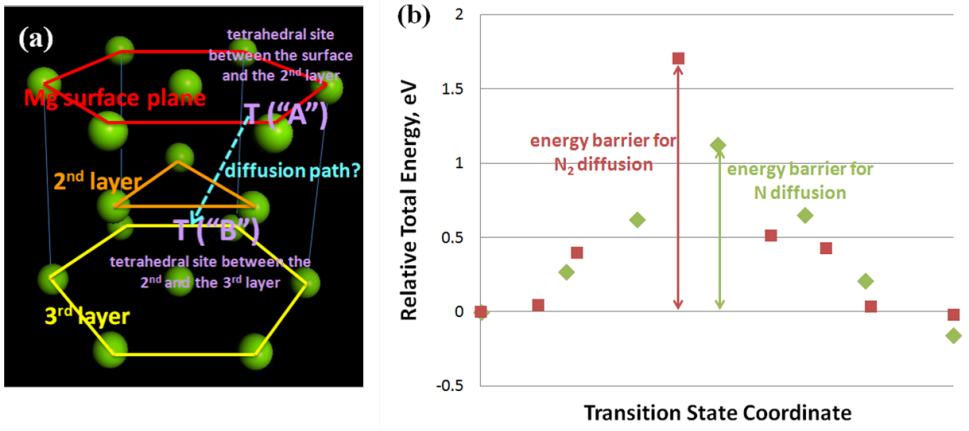

Figure 4.5: (a)Schematic illustration of the two tetrahedral sites for N_2/N lattice diffusion and (b)the relative total energy calculations to show the diffusion energy barrier between the two tetrahedral sites near the grain surface region.

To compare the diffusion energy barrier of N in the bulk region without the free surface of Mg matrix, total energy calculations based on geometry optimizations were performed using a pure bulk supercell structures containing $4 \times 4 \times 4$ atoms without vacuum surface. Two distinct diffusion paths, i.e., T-sites and O-sites in the bulk Mg, have been tested to compare the energy barriers for these two diffusion mechanisms. The relative total energy calculation results are plotted in Figure 4.6, demonstrating that the diffusion through T-sites is much easier than that through O-sites in the bulk Mg; the diffusion energy barriers for these are ~ 0.645 and ~ 1.632 eV, respectively. Therefore, the diffusion of N will be facilitated through the T-sites in the pure bulk lattice of Mg, if it occurs. Further, it is found that the diffusion energy barriers of N in the pure bulk and the bulk regions near the surface are different, which implies that incorporation of N into the subsurface of matrix grains is more difficult than the diffusion in the pure Mg matrix. As a final remark, although the results in the current work do not directly address the formation mechanisms of Mg_3N_2 near the grain surface, it should be mentioned that the present work can provide a useful insight about the

dissociation and the diffusion energies that must be kinetically provided to incorporate the nitrogen species into the Mg nano alloys during cryogenic PM process, which can lead to much enhanced mechanical properties by forming N-rich dispersoids near the grain surfaces and activating the Orowan strengthening mechanism by mechanical penetration of these dispersoids.

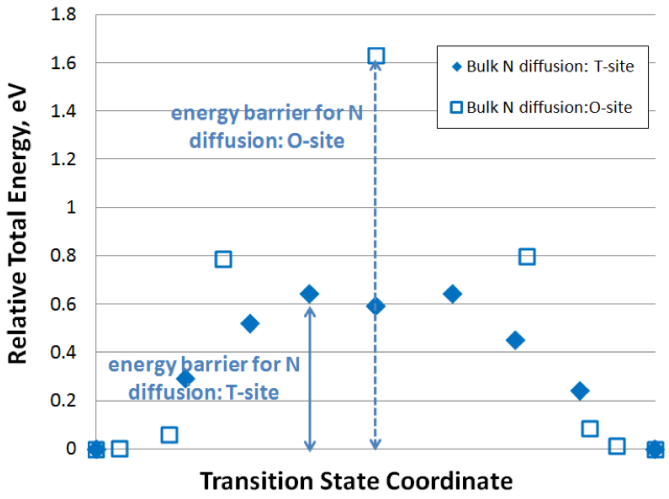

Figure 4.6: Relative total energy calculations to show the diffusion energy barrier of N between two tetrahedral sites and octahedral sites in the bulk region.

4.1.3 Diffusion of nitrogen in Mg lattice

Because it is not currently known whether the molecular or the elemental nitrogen (i.e., N_2 or N, respectively) would be predominantly present in the bulk Mg lattice during cryomilling, we modeled the MEP for the diffusion of both N_2 and N travelling between two sequential sites. Figure 4.7 depicts the schematic illustration of cryomilling attritor. Figure 4.7 also shows the initial and final Mg alloy model configurations containing one Al atom (i.e., Mg-Al alloy). In the figure, the dark blue, green, and magenta spheres represent N, Mg, and Al atoms, respectively. The same color notations for Mg, Al, and N atoms are used throughout the figures in the entire manuscript. For pure Mg systems, the Al alloying atom was replaced by the original Mg atom. The numbers in the figure indicates the relative atomistic z-positions in the unit cell. Here, the initial and final structures are superimposed to simply illustrate the interstitial diffusion paths through the (a) octahedral and (b) tetrahedral sites. For the substitutional diffusion case shown in Figure 4.7(c), rather than considering the two vacancy sites, switching the lattice positions between nitrogen

species at $z = 1/2$ and the center Mg atom at z=0 position was modeled. Prior to the diffusion calculation, we tested the input parameters of the DFT computation by calculating the formation energy of a vacancy ($E_{f,v}$) in the bulk Mg matrix using the following approach [161].

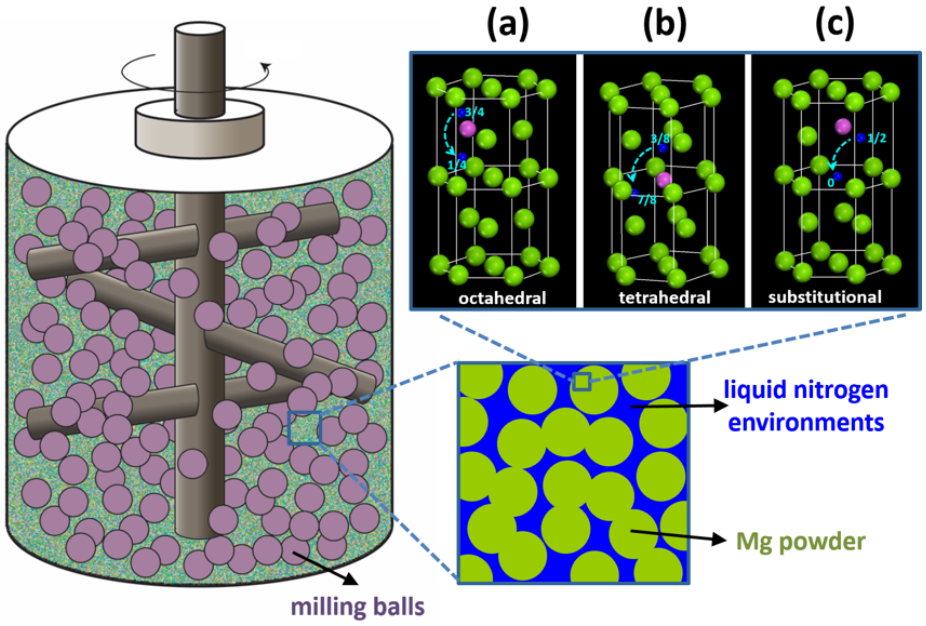

Figure 4.7: Schematic illustration to show the cryomilling attritor and the initial/final positions of N diffusing through the (a) octahedral (interstitial), (b) tetrahedral (interstitial), and (c) substitutional sites. The numbers indicate the relative atomistic z-positions in the unit cell.

$$E_{f,v} = E\left(n-1, 1; \frac{(n-1)}{n}\Omega\right) - \left[\frac{(n-1)}{n}\right] E(n, 0; \Omega) \tag{4.2}$$

Where $E(n, m; \Omega)$ is the total energy of the computational system of volume Ω with n atoms and m vacancies. $E_{f,v}$ in the Mg matrix was calculated as $\sim 0.86eV$, which shows a consistent prediction with previously reported values [162, 163]. After confirmation of the reliability on the input parameters, each of these initial and final configurations shown in Figure 4.7 has been geometry optimized to find the most stable coordinate for either N or N_2. Because the critical radius of an interstitial atom located in a tetrahedral site is ~ 0.54 times smaller than that in the octahedral site of a typical HCP crystal, it is likely that there is relatively much smaller space for the diffusion of N_2 molecule through the tetrahedral sites. With this, N_2 diffusion through the successive tetrahedral sites was excluded in the current computational sets.

Table 4.4: Formaion energy for the initial configurations considered in the present DFT study

Position	Nitrogen type	Formation energy in pure Mg ($eV/unit$)	Formation energy in Mg-Al alloy ($eV/unit$)
Tetrahedral	N_2	-	-
	N	-7.844	-7.832
Octahedral	N_2	-6.821	-7.011
	N	-8.249	-8.153
Substitutional	N_2	-6.504	-6.515
	N	-4.201	-7.213

Table 4.4 shows the calculated formation energies (E_F) of the structural configurations considered in the current work. (E_F) for each structure was obtained by subtracting the total energy of the completely separated objects from the total energy of the system combining the Mg/Mg-Al matrix and N/N_2 as given by,

$$E_F = E_T - E_{metal} - E_{N/N_2} \tag{4.3}$$

Where E_T is the total energy of the combined system including both Mg/Mg-Al and nitrogen, E_{metal} is the total energy of either Mg or Mg-Al alloy, and E_{N/N_2} is the total energy of isolated N or N_2. As presented in Table 4.4, all of the structural configurations manifest a strong thermodynamic stability with E_F ranges of -4.201 to -8.249 eV/unit. Therefore, these structures for bulk diffusion would be deemed reasonable as the initial configurations.

As described in the Computational methods section, before conducting the MEP computations to estimate the energy barrier for diffusion, the initial and final configurations have been geometry optimized starting from the regular structures containing a nitrogen species at the exact octahedral, tetrahedral, and/or substitutional sites. For systems with an N_2 molecule, the center of mass of the N_2 molecule was initially positioned at these interstitial lattice sites. Figure 4.8 shows the examples of energy variations with geometry optimization steps for the (a) pure Mg and (b) Mg-Al systems including an N_2 molecule at the octahedral site. The small red dots in the initial structural images of the figure indicate the center of mass of the N_2 molecule. After geometry optimization, one can easily notice that the center of the corresponding N_2 molecule is not positioned at the exact octahedral site locations any longer due to anisotropic interactions between the N_2 molecule and

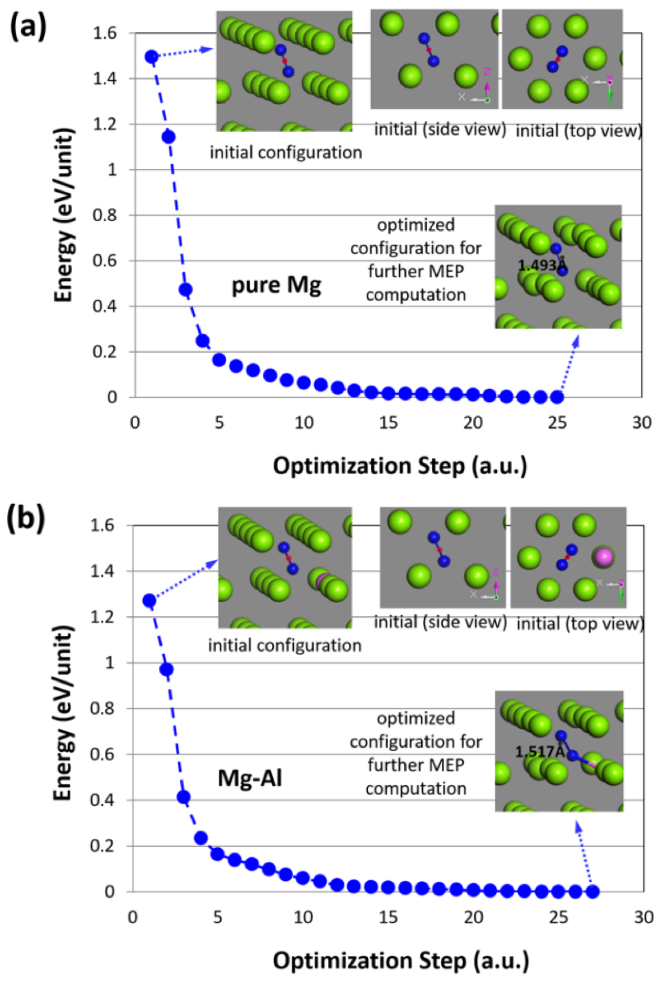

Figure 4.8: Examples of energy minimization before he minimum energy path (MEP) calculations for he (a)pure Mg and (b)Mg-Al systems including an N_2 molecule at the octahedral site.

the surrounding lattice atoms. These local energy minima states have been set up as the initial structures for further MEP computations. For each computation set, a final configuration of the atomic structure for diffusion with local energy minima has also been identified using the same geometry optimization approach.

In Figure 4.9, we first show the relative total energy changes (ΔE) in the octahedral and the substitutional cases using the scale in the left-hand side y-axis based on the calculated MEPs for N_2 molecule. In the path coordinate, the initial and final configurations are indicated as 0 and 1 (arbitrary units), respectively. The energy level of initial configuration was set to 0 for a relative comparison. To correlate the ΔE values, the N-N bond length of N_2 molecule (d_{N-N}) during the

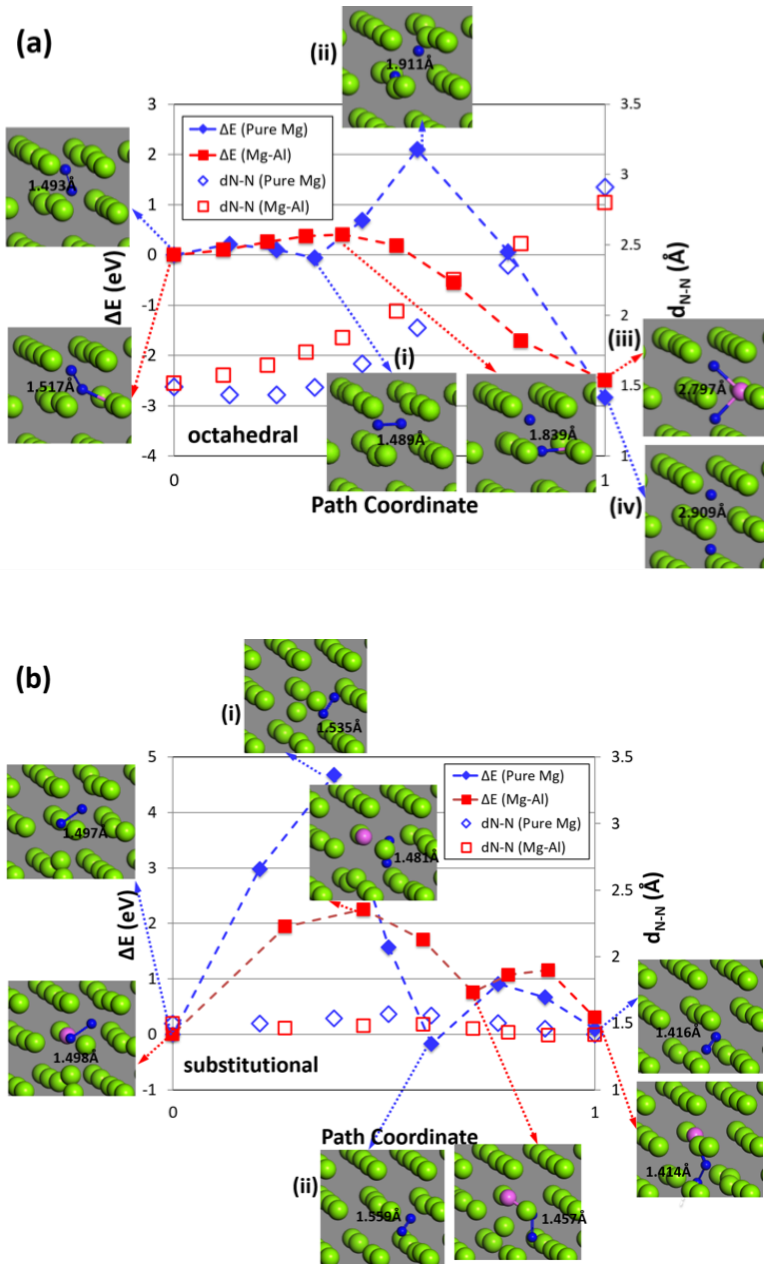

Figure 4.9: Calculated minimum energy path (MEP)and the N-N bond length (d_{N-N}) for a N_2 molecule in the pure Mg and Mg-Al alloy diffusing through the (a) octahedral and (b) substitutional sites.

diffusion process was also displayed using the scale in the right-hand-side y-axis. For diffusion of N_2 between two sequential octahedral sites in pure Mg system (blue symbols), the initial change of d_{N-N} occurs by a small stretching of the N-N bond, and it increases as the diffusion proceeds. As the N_2 molecule rotates and finds a more relaxed site until the molecule is horizontally oriented as presented in image (i) of Figure 4.9(a), ΔE decreases slightly, however, then for the nitrogen to

pass through the Mg plane and diffuse to the next octahedral site, a significant amount of energy is required. At this stage, one N atom distorts the regular structure of the dense Mg plane as shown in the structural image (ii) of Figure 4.9(a), which is not favorable for the Mg structure, therefore, the energy of the system increases. At this point, d_{N-N} increases resulting in complete dissociation, because is considerably larger than the nominal range of the nitrogen bonding ($1.098 - 1.454A^{\circ}$ for the triple and single bonding, respectively) [164, 165]. In this work, a 10% tolerance from the ideal bond length was considered for the bond breaking criterion. The ideal bond was defined as the sum of covalent radii of two atoms forming the bond. This tolerance limit was used based on the energy calculation with regards to the isolated N_2 molecule bond length. From this, it is predicted that not only the triple bonding of N_2 breaks, but also there is no probability for the formation of single N-N bond during this diffusion process. In the proceeding computational frames after N_2 dissociation, d_{N-N} continues to increase, and the molecular diffusion changes to the atomic diffusion, which results in decreasing the energy level of the system. The decrease in ΔE continues until one of the N atoms is located in the initial $z = \frac{3}{4}$ octahedral site while the other one occupies the final $z = \frac{1}{4}$ octahedral site as shown in the structural image (iv) of Figure 4.9(a). The negative relative energy for the final state implies that the N_2 molecule is not able to diffuse to the bulk of the Mg matrix through the interstitial sites, the existence of N_2 molecule is relatively unstable inside a perfect Mg crystal lattice, and the dissociation of N_2 molecule would take place to minimize the energy of the system when sufficient energy is supplied.

In Figure 4.9 (a), a similar behavior is observed for the Mg-Al alloy system (red symbols). Again, it was found that the highest energy level of the system corresponds to the state where one N atom is located in the passing (0001) atomic plane of matrix. However, the maximum ΔE for the transition is much less than in pure Mg, presumably due to the smaller size of the Al atom. The lowest energy level of the system is obtained when the complete dissociation of N_2 takes place and each of the N atoms is positioned in the sequential interstitial site as shown in the snapshot (iii) of Figure 4.9(a). In both pure and alloy compositions after N_2 dissociation, the moving N atom interacts with their closest neighbors to create weak bonding. The calculation shows that the average bond lengths for Mg-N are $\sim 1.922A^{\circ}$ and $\sim 2.117A^{\circ}$ for the pure Mg and alloy systems, respectively, and the Al-N bond length is equal to $1.879A^{\circ}$. The higher tendency for bond formation could be the reason for the smaller energy barrier in the alloy system. However,

as these interactions are weak, the N atom can continuously move through the Mg lattice to lower the energy of the system once the energy barriers are overcome as shown in Figure 4.9 (a).

Figure 4.9(b) shows and of the N_2 molecular diffusion when a vacant site is accessible near the diffusion path. Considering in Figure 4.9 (b) (open symbols), bond breaking would not be expected either in pure Mg or in Mg alloy systems; the variations in are relatively small, which will not result in molecular dissociation of N_2 during diffusion. When the substitutional diffusion is modeled taking into account of the switching event of simultaneous N_2 and Mg lattice diffusion, the changes in the energy of the systems are much more significant for N_2 diffusion compared with the octahedral diffusion case. As seen in the calculation results, the system needs to overcome an energy barrier of $\sim$ 4.7 eV for pure Mg (blue solid symbols) and $\sim$ 2.3 eV for Mg-Al alloy (red solid symbols) systems, respectively. The maximum in pure Mg is realized when the switching Mg atom approaches the initial vacancy site while one of the N atoms of N_2 is still located in the same plane as shown in the structural image (i) of Figure 4.9 (b). As the Mg atom moves closer to the plane, the energy of the system decreases until it fills the vacant site and N_2 occupies an interstitial site that is close to the newly formed vacancy (see the image (ii) of Figure 4.9 (b)). The calculation showed that this state exhibits an energy level that is comparable or slightly lower than the initial and final configurations. For further diffusion, a secondary energy barrier of $\sim 1eV$ exists. Similarly, for Mg-Al alloy, the peak position of is observed when one of the N atoms passes through the next (0001) lattice plane, and the energy barrier is estimated as $\sim$ 2.3 eV that is nearly half of the value of the pure condition. In the alloy system, the N_2 molecule has higher probability for diffusion in the metal, although the energy barrier is still high. Unlike the pure case, the intermediate minima is less stable than the initial and final states, but again the system will experience a secondary transition state with energy barrier of $\sim 0.4eV$.

It was reported that the bond breaking energy of the N_2 triple bond over the pure Mg surface ($\sim 1.13eV$) is $\frac{1}{9}$ of the dissociation energy of an isolated N_2 molecule ($\sim 9.7eV$) [136]. Although this bond breaking energy over the Mg surface is much lower than the dissociation energy of a single N_2 molecule, 1.13 eV is still a very high barrier for N_2 molecules to break into the elemental form. It is currently uncertain if elemental N is present in the Mg bulk lattice during the cryomilling process of nanocrystalline Mg alloys/composites. If elemental N atoms are available in the bulk Mg lattice, it is likely that a high external mechanical energy was provided to the liquid N_2 molecule during the

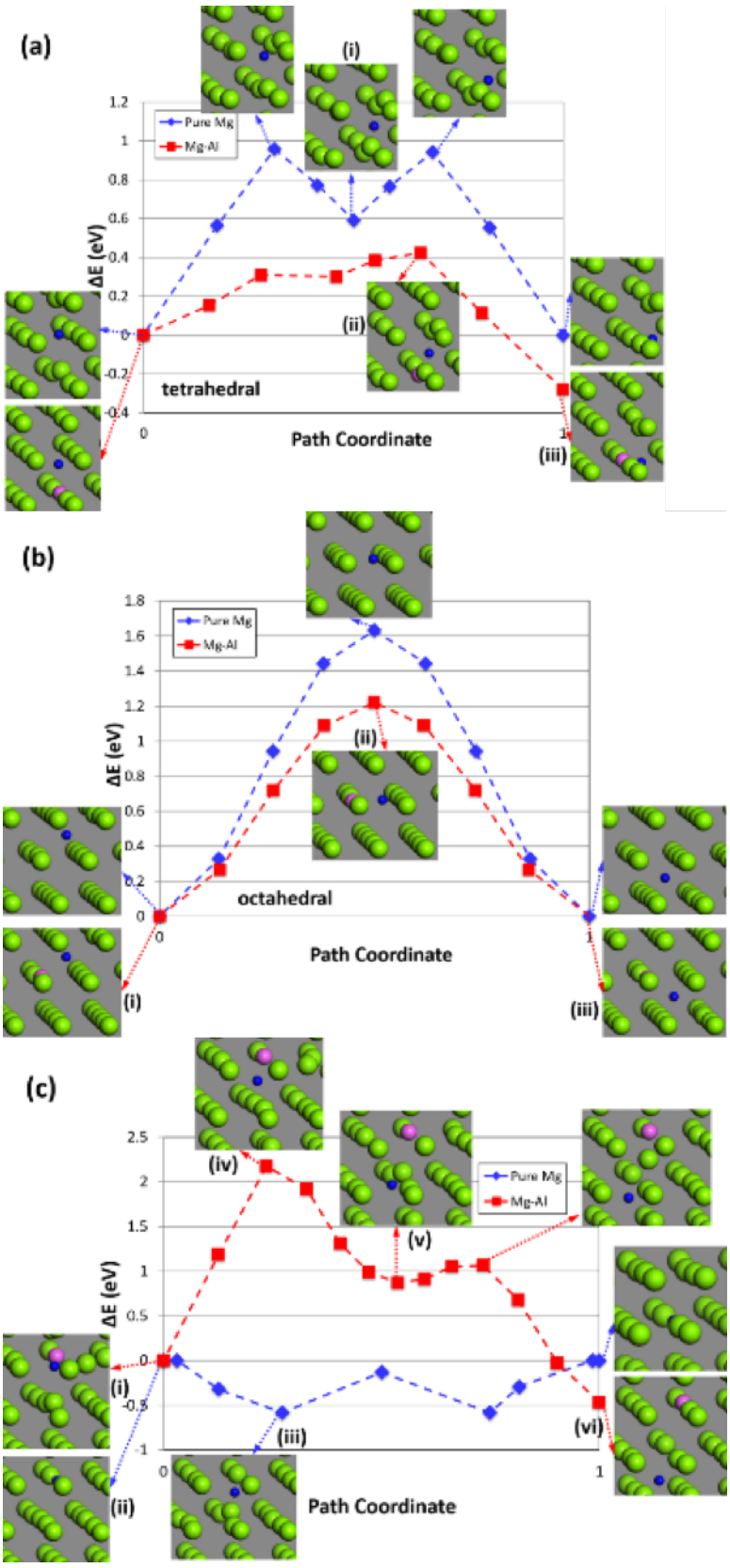

Figure 4.10: Calculated minimum energy path (MEP) for N atom in pure Mg and Mg-Al alloy diffusing through the (a) tetrahedral, (b) octahedral, and (c)substitutional sites.

cryomilling process. Also, there might be other mechanisms of N_2 dissociation with a much lower bond breaking energy barrier. Irrespective of the high dissociation energy barrier, the bulk Mg system containing separated/dissociated N atoms showed a more stable configuration [127]. With the possibility of the presence of elemental N, in Figure 4.10, we show the total energy changes (ΔE) of the Mg materials based on the MEP calculations for the N atoms travelling between the sequential (a) tetrahedral and (b) octahedral sites. Interstitialcy diffusion through the tetrahedral sites was considered for elemental N diffusion, as the atomistic volume of N atom is sufficiently small to be retained in the tetrahedral sites.

For elemental N diffusion through the tetrahedral path inside the bulk of pure Mg (blue symbols in Figure 4.10(a)), the lattice distortion of surrounding Mg atoms due to the N diffusion was symmetric, therefore, the consequent ΔE through the diffusion path is also symmetric. The initial and final geometries showed the highest stability, and a local minimum is observed indicating that there is a relatively stable position between the two sequential tetrahedral sites at the half way point of diffusion, as shown in the structural image (i) of Figure 4.10(a). When an N atom is travelling in Mg-Al system (red symbols in Figure 4.10(b)), the ΔE variation is not symmetric anymore in the travelling path due to the anisotropic interaction of N atom and the surrounding matrix atoms. The maximum is observed when the moving N atom is located slightly above the (0001) matrix plane (see the structural image (ii) of Figure 4.10(a)). In the final stage after geometry optimization, the N atom is positioned in line with the (0001) matrix plane, off from the regular tetrahedral site in the HCP crystal, as seen in the snapshot (iii) of Figure 4.10(a). Here, the forces from all neighboring atoms would be balanced to establish the minimum energy state. Note that the diffusion energy barrier of N atom in Mg-Al alloy system is much lower than that in pure Mg materials. Although a higher attraction is expected from Mg atoms for the moving N due to the higher electronegativity differences between Mg and N than between Al and N, there is a $\sim 16.6\%$ decrease in the atomic radius when an Mg lattice atom is substituted with an Al atom. This would provide more space for the travelling N atom, thereby lowering the energy of the system in the final state. It is thought that the energy barriers of the N atoms through the tetrahedral path are still too large to be overcome by Boltzmann statistics, but they are much smaller than the barriers for the diffusion through the octahedral sites reported in Figure 4.10(b). The energy barriers for the transition between octahedral sites are 1.63 eV and 1.22 eV for pure Mg and the alloyed systems, respectively. This

means that the octahedral site provides a much more stable site for the N atom compared with the other surrounding sites in both pure and alloyed systems. Monitoring the trajectory files for this process reveals that the highest for both pure and alloyed systems correspond to the configurations when the N atom is passing through the compact (0001) matrix plane (see the structural image (ii) of Figure 4.10(b)). The predicted MEPs are symmetric for both pure and alloy materials, and less lattice distortion is observed compared with the tetrahedral diffusion case as shown in the structural images (i) and (iii) of Figure 4.10(b). This can be explained by a higher stability of the N atom in the initial and final octahedral sites after geometry optimization.

In addition to the N diffusion through the tetrahedral and octahedral sites, the substitutional diffusion of N is modeled with switching the (vacancy + N) and Mg atom positions, and it was identified that the energy barriers for the pure and alloy systems are 0.58 eV and 2.17 eV, respectively. Figure 4.10(c) presents the calculated profiles for these substitutional scenarios. After geometry optimization of the initial structures, the N atom is pushed away from the original substitutional position in searching for the local minima in the Mg-Al alloy case, most likely due to the anisotropic interactions between the N and Mg-Al lattices as shown in the structure image (i) of Figure 4.10(c). In contrast, we observe that when all of the surrounding matrix atoms are identical, the forces applied to the N atom can be balanced off with each other, which leads to the N atom residing in the vacant site until diffusion starts (see the structure image of (ii) of Figure 4.10 (c)). This state is considered as a very shallow local minimum state; as the N atom diffuses inside the bulk and exchanges its position with one of the Mg atoms, the energy of the system decreases because the small N atom prefers the interstitial sites in the diffusion path rather than the original vacancy site. In this substitutional situation, the minimum energy state in the diffusion pathway corresponds to the intermediate transition state (image (iii) of Figure 4.10(c)), not the initial or final states. Therefore, it would be more relevant to estimate based on this minimum energy configuration, and for such diffusion is now 0.58 eV. On the other hand, when one of the matrix atoms is replaced by Al, the diffusing N atom is subject to a relatively high MEP, as shown in the structure image (iv) of Figure 4.10(c) until it reaches a local minimum (image (v) of Figure 4.10(c)) upon passing (0001) matrix plane. At this local minimum, the vacancy remains unchanged, and once the N atom starts to diffuse to the next layer, the vacancy moves to the plane close to the N atom where the second peak in the energy plot is observed. In the final state, the N atom is located in the

interstitial site (i.e., near the octahedral site) away from the Al impurity as shown in the image (vi) of Figure 4.10(c). From these results, it is expected that, as long as the N_2 molecules are dissociated to two N atoms, the existence of vacancy sites strongly reduces the energy barrier in pure Mg. Table 4.5 summarizes the energy barriers through the different diffusion paths of N and N_2 in the pure and alloy Mg systems considered in the current work. The units of energy barrier were converted to [kJ/mol] from [eV/structural unit]. As seen in the octahedral diffusion case, when molecular dissociation is accompanied, the diffusion energy barrier includes the atomistic diffusion energy barrier in addition to the energy required for dissociation. When a vacant site is available near the diffusion path of an N2 molecule, the current DFT calculation showed similar results to the work by Ma et al. [160]; they showed that molecular diffusion is much preferred when a vacancy is located closer than $7.4A^{\circ}$ to the N_2 molecule in the Al/Al_2O_3 system. From Table 4.5, it is clear that the existence of Al impurities can promote the diffusion kinetics for both N atoms and N_2 molecules. However, when a lattice vacancy exists near the N atom, the optimized structures and the diffusion path could be strongly influenced by the presence of alloying elements and that the switching phenomena through the substitutional diffusion in the pure Mg materials would be essentially achieved by the interstitial mechanism. It must be noted that, the diffusion energy barriers listed in Table 4.5 are based on the probable diffusion projectiles considered in this work. It is perceived that there might be other diffusion mechanisms/paths than the cases listed in Table 4.5. However, it would be reasonable to set the energy barrier ranges of N and N_2 bulk diffusion to be $\sim$ 100 to $\sim$ 160 kJ/mol and $\sim$ 200 to $\sim$ 450 kJ/mol, respectively. These energy barriers can be lowered to $\sim$ 40 to $\sim$ 200 kJ/mol and $\sim$ 40 to $\sim$ 220 kJ/mol for N and N_2 diffusion, respectively, when Al is incorporated as an alloying element. In conjunction with Table 4.5, in Figure 4.11, we also show the entire total energy changes including the formation energies (E_f in Eq. **??**). In the figure, the y-axis positions of horizontal bars represent the relative total energy changes of the initial (before diffusion) and final (after diffusion) structures with regards to the energy of the completely separated (i.e., Mg/Mg-Al matrix and N/N_2 atom/molecule) systems.

Note that, in Figure 4.11, the relative energies of the initial and the final states of the substitutional N diffusion for pure Mg were adjusted to the energies of local minima (see the structural snapshot (iii) of Figure 4.10(c)) in the diffusion pathways so as to represent the energy barrier of 0.58 eV. For pure Mg, it is thought that the interstitial tetrahedral and the substitutional switch-

Table 4.5: Summary of the diffusion energy barriers calculated in the present DFT study

Position	Nitrogen type	Energy barrier in pure Mg (kJ/mol)	Energy barrier in Mg-Al alloy (kJ/mol)	Comment
Tetrahedral	N_2	-	-	-
	N	92.336	40.771	-
Octahedral	N_2	202.563	38.941	N_2 dissociates
	N	157.485	117.691	-
Substitutional	N_2	451.12	217.067	N_2 does not dissociate but diffuses with high energy barrier
	N	56.032	209.707	-

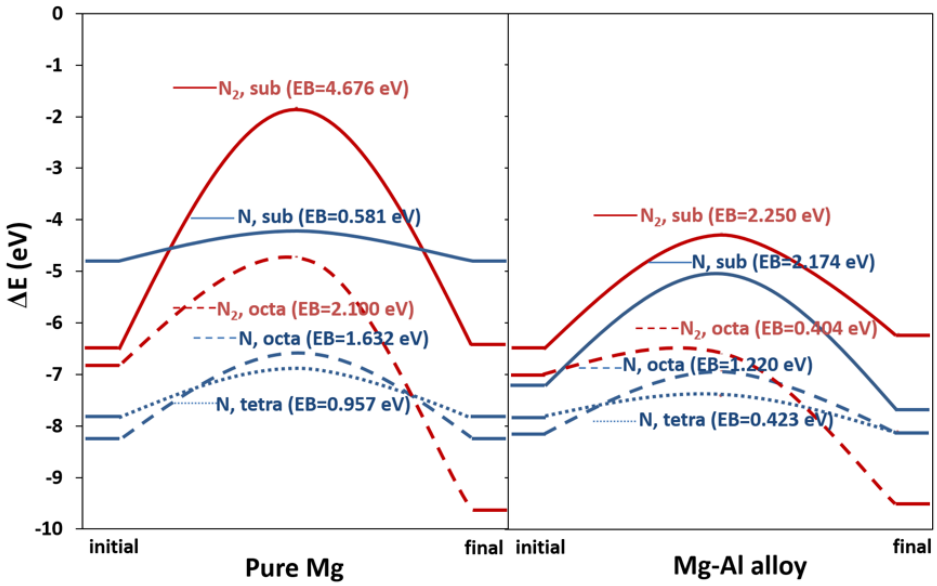

Figure 4.11: Summary of formation energies and total energy changes of the structural cinfigurations including diffusion energy barriers (EB) for the pure Mg and Mg-Al systems considered in the present DFT calculations.

ing mechanisms would be the easiest routes for N atom diffusion and that interstitial octahedral mechanism involving the N_2 dissociation would also be favorable, although there is a fairly high diffusion energy barrier ($\sim 2.10eV$). When Al is included in the Mg matrix, the formation energies are comparable to those of pure Mg, but the total energy of the Mg-Al system with a vacancy/N atom pair is much lower than that of the pure Mg system. For this alloy system, the interstitial tetrahedral diffusion of N and substitutional/dissociation of N_2 mechanism would be the easiest

paths out of the scenarios tested in this work For both systems, the dissociation of the N_2 molecule into N atoms is expected in the octahedral diffusion case (i.e., red dashed curves in Figure 4.11). From Figure 4.11, one can readily find that the relative total energy of Mg/Mg-Al lattices (-6.82 and -7.01 eV for pure Mg and Mg-Al, respectively) containing an N_2 molecule at octahedral site is higher than those of Mg systems with a single N atom either at octahedral or tetrahedral sites that are given by the initial and final energy states with dashed (octahedral) and dotted (tetrahedral) curves. After N_2 dissociation in this octahedral diffusion, however, the relative total energy of lattices including two N atoms at octahedral sites becomes much lower (-9.65 and -9.51 eV for pure Mg and Mg-Al, respectively) than the energies of those lattices with a single N atom at interstitial positions. Therefore, it is thought that when N_2 molecule is introduced in the Mg/Mg-Al matrices, the dissociation of N_2 molecule is energetically feasible through the octahedral diffusion process if the corresponding energy barrier can be overcome.

4.1.4 Formation of Mg nitride

As alluded to earlier, nitrides formed during the cryomilling process have been credited as a source of Orowan strengthening and as a mechanism to pin the grain boundaries serving to help retain the nanocrystalline structure [55, 150, 151, 166]. Therefore, as the next computation set, the formation energy of N-rich dispersoids was calculated. Here, we assume that the N-rich dispersoids would take the crystal structure of Mg_3N_2 (anti-C-type, antibixbyite structure) [140]. The antibixbyite structure can be constructed starting from the Fluorite structure (i.e., CaF_2 structure); CaF_2 structure was used for Mg_2N and an idealized antibixbyite structure was obtained by removing $\frac{1}{4}$ of Mg atoms from a $2 \times 2 \times 2$ supercell [167]. The final structure was set in a way that each nitrogen atom to have six nearest neighbor Mg atoms. Considering that the nucleation of such second phase starts with forming a coherent interface, we calculated the formation energy of an Mg_3N_2 nuclei containing several formula units of Mg_3N_2. To create such a coherent interface, it was assumed that an Mg_3N_2 nucleus with coherent interface would be initiated by the nominal HCP Mg structure containing N atoms in the octahedral site because of the high stability of N atoms positioned in the HCP octahedral sites and the high structural similarity between the cubic anti-C-type Mg_3N_2 and HCP Mg containing N atoms in the octahedral sites. Figue 4.12(a) and (b) show the atomistic structures of Mg_3N_2 dispersoids, (a) before and (b) after geometry optimization.

The calculated formation energy for this nitride was -457.86 kJ/mol that is comparable with the experimental value of -460.66 kJ/mol at room temperature [168]. These results further confirm that the antibixbyite nitride structure could be thermodynamically stable in the cryomilling condition when a sufficient number of nitrogen atoms is available. In Figure 4.12(c), the formation energy variations Mg_3N_2 nuclei with various numbers of Mg_3N_2 units near the basal (0001) surface region and in the bulk are shown. Calculated results showed negative formation energy values for both of the structures implying the thermodynamic possibility of the formation of this Mg_3N_2 nuclei-like structure when sufficient N atoms are available at these sites. The predicted formation energy for the structures in the (0001) surface is higher than that in the bulk region, however, note that the initiation and subsequent growth rate of Mg_3N_2 precipitates would be limited by the contents and the diffusion rates of available nitrogen atoms. Also, although the formation energy of this nuclei-like structure in the bulk region is lower than that in the surface region, the results predict that there is a higher chance for observing this component near the surface layer because unless sufficient energy is provided before the formation of such N-rich dispersoids near the surface/grain boundary of Mg grains, the diffusion energy barrier in the bulk Mg lattice is very high for the most of the situations considered in this study.

Mg_3N_2 was identified experimentally in a cryomilled Mg WE43 powder [13]. In Figure 4.13 (a), a dispersoid (indicated by the white arrow in Figure 4.13) of about 100 nm in diameter was observed using high angle annular dark field (HAADF) STEM at a camera length of 80 mm. EELS was used to detect the presence of nitrogen and oxygen in the dispersoid. Figure 4.13(b) shows the presence of the both the nitrogen and oxygen k-edges present in the EELS spectrum. Utilizing these types of spectra, EELS was used to map the spatial distribution of oxygen and nitrogen in and around the dispersoid observed. In Figure 4.13(a), we also show the elemental maps obtained by subtracting a power-law background from the spectra at each pixel and integrating the remaining signal in the nitrogen and oxygen k-edges, respectively. In these elemental maps (middle column of Figure 4.13(a)), the brightness of each pixel is indicative of the relative concentration of the respective element. We also provided the elemental map using a color scheme for visualization. From these figures, it was identified that oxygen was distributed evenly throughout the region examined (see the middle bottom or right-hand side images of Figure 4.13(a)) and nitrogen was strongly concentrated in the dispersoid (see the middle top or right-hand side images of Figure

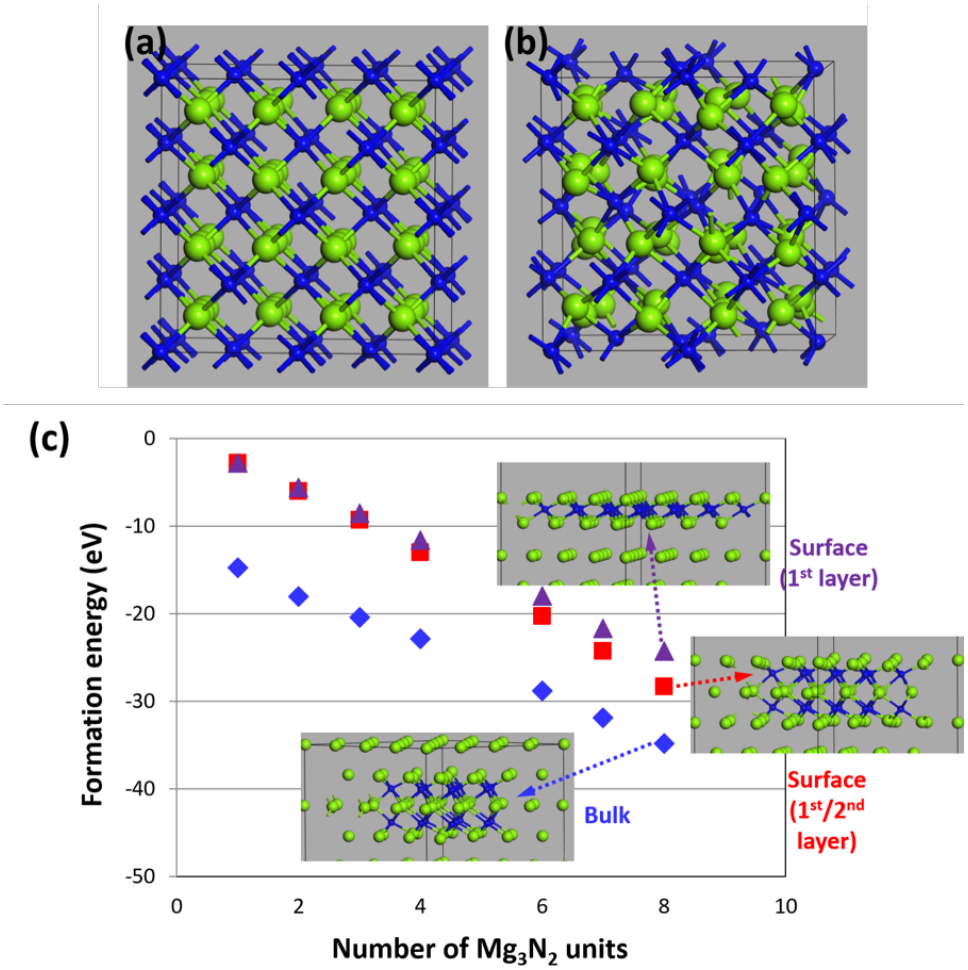

Figure 4.12: Summary of formation energies and total energy changes of the structural Antibixbyite crystal structure of Mg_3N2, (a) before and (b) after the geometry optimization, and (c) formation energy changes with various numbers of Mg_3N_2 nuclei units in the bulk Mg and Mg basal (0001) surfaces.

4.13(a)), which confirms that this dispersoid is a nitride. According to the Mg-N phase diagram, Mg_3N_2 forms from the reaction of Mg with N [169]. The nitrides of Y and Nd are both 50:50 compounds with N, forming YN and NdN, respectively [169, 170]. To verify the identity of the nitride, EDS was used to investigate the dispersoids composition. Observing the elemental values (Mg 95.9$wt\%$, Y 2.3$wt\%$, and Nd 1.8$wt\%$), the dispersoid rare earth chemistry is very similar to that of the bulk alloy and therefore is likely to be Mg nitride. Oxygen and nitrogen signals were also detected with EDS, however, the quantitative values are known to be unreliable on the older-model Si(Li) detectors with polymer windows such as the one utilized in this investigation.

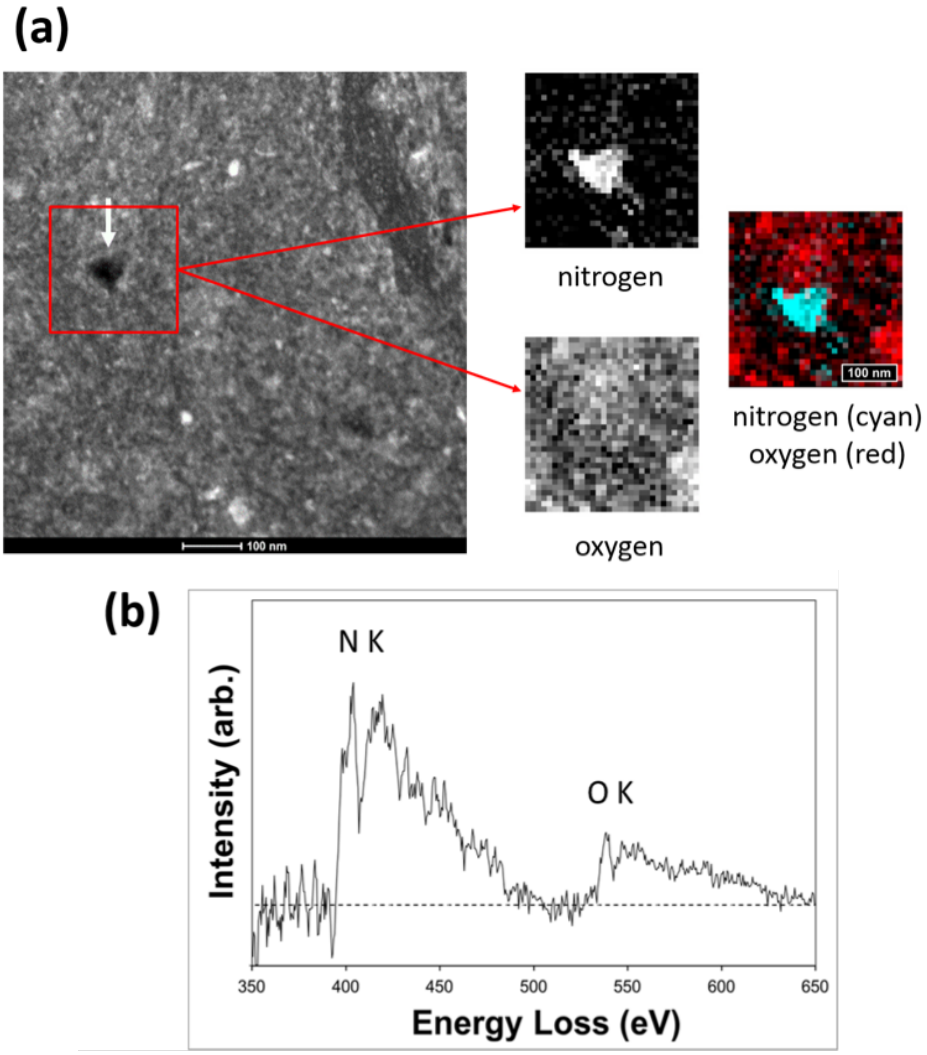

Figure 4.13: (a) HAADF micrograph of the Mg powder with EELS elemental maps to show the concentration of nitrogen and oxygen around the dispersoid and (b)EELS spectrum of the dispersoid with N and O K edges [13].

4.2 Al cryomilling

With their potential superior mechanical properties, the nanocrystalline Al alloys/composites synthesized under cryogenic environments using the cryomilling process have received widespread attention [23, 171, 172, 173] in recent years. These nanocrystalline materials are typically subject to a sequence of fabrication processes including cryomilling, degassing, hot isostatic pressing (HIP), extrusion, etc. In the cryomilling process, the powdered Al materials are routinely exposed to liquid nitrogen atmosphere to minimize the milling time, to obtain ultrafine grain sizes, and to prevent

the undesired oxidation reactions. The synthesized microstructure using this technique generally features grain sizes under 100 nm and presence of dispersoids with various sizes and compositions [174, 175]. The types, sizes, and distributions of such dispersoids embedded in the Al metal-matrix can greatly influence the mechanical properties of synthesized products. The formation of nitrogen-rich dispersoids (most likely AlN) during fabrication is very important, because these dispersoids are claimed to possibly activate the Orowan strengthening mechanism [127, 160, 174, 152]. Activation of the Orowan strengthening mechanism is strongly desired as it does not necessarily decrease the ductility while increasing the strength of materials [55]. Despite a variety of previous reports showing the nanocrystalline Al alloys/composites with improved strength, most of the examples exhibited relatively poor ductility when they were prepared from the cryomilling process [176, 177, 178, 179, 180]. Further, the distribution and the diffusion of nitrogen species introduced from the cryomilling atmosphere in Al matrix are also important because they strongly influence the grain size and the nitrogen-rich dispersoids formation, which can greatly impact the mechanical performance of samples [8]. It is, therefore, a vital importance to understand the interaction between the nitrogen species and the metal-matrix upon cryomilling process [13]. However, experimental measurements of such interaction during cryogenic cryomilling process can present a formidable challenge, therefore, the quantitative description for these liquid nitrogen adsorption, absorption, and diffusion in the Al lattice has been highly limited in the previous literatures. With this, in the present work, we systematically performed atomistic computations employing the density-functional theory (DFT) technique to examine the interaction between liquid nitrogen species and Al metal-matrix. During the cryomilling process, the liquid nitrogen molecules (N_2) in the milling tank are adsorbed onto the Al powder surface and those molecules might be dissociated into elemental nitrogen atoms (N). To systematically study such interactions, a comprehensive set of atomistic level calculations was conducted quantifying the (i) adsorption energy of liquid N_2, (ii) dissociation energy of N_2 into N atoms, and (iii) diffusion energy barrier for N and N_2.

4.2.1 Adsorption of N_2

Depending on the morphology and the composition of the adsorbent surface, the adsorption behavior of N_2 molecule can be varied. It is expected that a surface with wider hollow sites would provide favorable condition for N2 dissociation. Because a surface with lower atomic density typically ex-

hibit a higher tendency for N_2 molecule adsorption and such stronger metal-nitrogen interaction results in a weaker nitrogen-nitrogen interaction, the dissociation of N_2 into N atoms is relatively easier over a loosely packed surface. The adsorption energy (E_{ad}) of liquid nitrogen on Al-based surfaces (pure or alloy Al systems) can be estimated based on the energy state differences between the separated and the combined structures of adsorbate (i.e., nitrogen molecule) and adsorbent (i.e., Al surface), as given by $E_{ad} = \frac{1}{n}[E_{total} - E_{slab} - nE_{N_2}]$, where E_{total} is the total energy of the system, E_{slab} is the total energy of clean Al slab without N_2, is the number of N_2 molecules, and is the total energy of single N_2 molecule, respectively. Because very high energy is generally required for N_2 molecule dissociation, it is likely that the liquid nitrogen is adsorbed onto the Al surface in its molecular form (i.e., N_2) during cryomilling. Applying the computation parameters given above, the DFT calculation results showed that the N_2 dissociation energy is 998 kJ/mol, close to the experimentally measured value of 942 kJ/mol [181]. We also calculated the formation energy ($E_{f,AlN}$) of N-rich dispersoids (i.e., AlN). Assuming that the N-rich dispersoids would take an ideal wurtzite structure, the lattice parameter and $E_{f,AlN}$ were computed as a=3.134 $A°$, c/a=1.597, and = -294.32 kJ/mol, which are consistent with experimentally measured values of a=3.111 $A°$, c/a=1.601, and = -303.16 kJ/mol [**?**]. In Figure 4.14, we show the geometry optimized AlN structure.

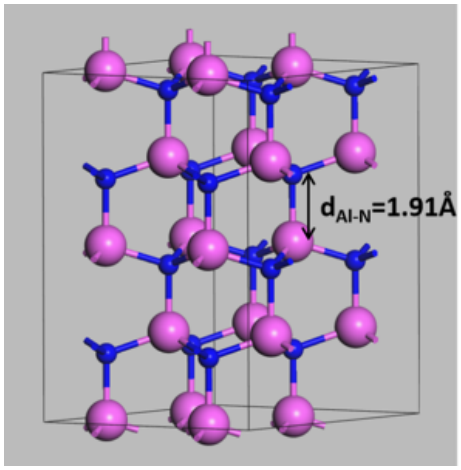

Figure 4.14: Crystal structure of AlN (wurtzite) after geometry optimization.

For the adsorption and the dissociation of N_2 molecule in contact with the Al surface, as shown in Figure 4.15(a), one N_2 molecule was positioned at the atop position with a vertical distance of$\sim$ 2 $A\circ$ from the surface, which was the lowest energy state containing one N_2 molecule with upright

configuration. The adsorption of molecular species on FCC (111) surface is generally achieved through four probable adsorption sites, i.e., atop, bridge, hollow1 (HCP hollow), hollow2 (FCC hollow) sites [182, 183]. In Figure 4.15(b), we display the contour map of the calculated over the (111) plane of pure Al surface. The calculated E_{ad} values onto the atop, bridge, hollow 1, and hollow 2 sites were -0.142, -0.136, -0.138, and -0.134 eV, respectively, which implies that the adsorption of N_2 onto the pure Al surface is thermodynamically favorable through all four adsorption sites and that the atop site is the best location for adsorption. Note that, although the adsorptions through all four probable sites are thermodynamically favorable with negative adsorption energies, these E_{ad} values correspond to physisorption ($E_{ad} < 0.2$ eV, van der Waals interactions) without forming a strong chemical bonding (i.e., chemisorption). In fact, the symmetry of the N_2 molecule can reduce the overlapping of the N_2 lowest unoccupied molecular orbital (LUMO) with the electron states of substrate Al metals, which will prohibit forming a strong chemical bonding between N_2 and the metal surface. Even with highly conductive free-electron-like metals such as Al, the interaction with N_2 molecule is predicted to be fairly weak [184]. This finding is in good agreement with the experiments by Jacobi et al. [185] and other previous DFT calculations that reported no chemical bonding would form between the N_2 molecule and pure Al (111) surface [184, 186].

We then tested the N_2 adsorption tendency at the atop site for various Al systems with different surface orientations. In Figure 4.15(c), we summarize the calculated E_{ad} values onto the atop position of pure Al, Al-Mg, Al-Mn, and Al-Fe alloy systems with (100), (110), and (111) surface planes. From the results shown in Figure 4.15(c), E_{ad} for alloyed systems all exhibited lower values compared with pure Al. It was proposed that the molecule-surface attraction could hypothetically form extra overlap between the LUMO of N_2 and some substrate electron states, which would downshift the LUMO resonance further. Downshift of LUMO will cause the molecular orbital cross the Fermi level. When combined with the d orbital in the transition-metals, these changes in the orbital states of N_2 will exhibit marginal effects for sticking, molecular adsorption, and molecule dissociation [184]. When one Al atom is substituted with an Mg atom, a stronger bonding between Mg atom and N_2 molecule is expected, because the 3s2 orbital of Mg has a slightly greater electron donation propensity to the N_2 $1pi*$ antibonding orbital. Also, the presence of larger transition metals (Mn or Fe) on the Al surface can strongly increase the thermodynamic tendency for N_2 attraction. The stronger interaction of N_2 to the surfaces alloyed with Fe and Mn can be described

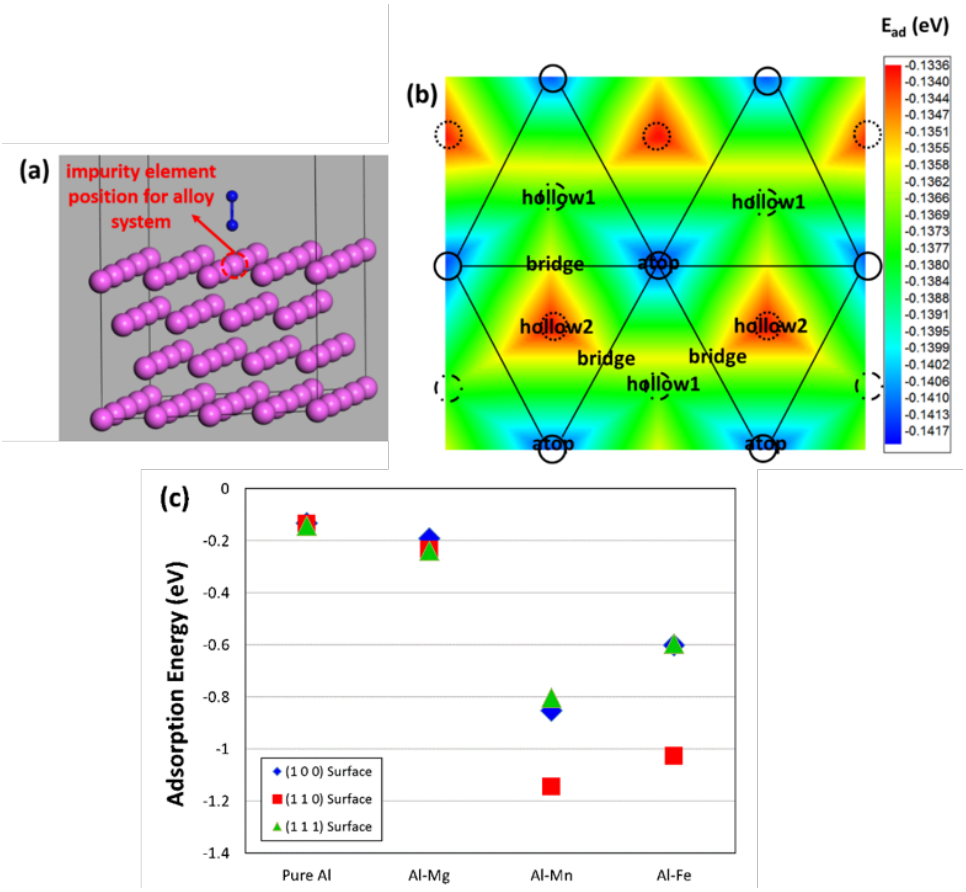

Figure 4.15: (a) Adsorption of N_2 molecule onto the (111) surface of Al, (b) contour map of calculated over the (111) surface of Al, and (c) calculated E_{ad} onto the atop position of various Al-based systems with (111), (110), or (100) surface orientations.

by the d-band center model by Hammer and Nrskov [187]. When an N_2 molecule is adsorbed onto metallic surfaces, the adsorption occurs in a two-step sequence. The initial step takes place by coupling between the adsorbate orbital levels and the itinerant sp electrons of the metals, which will result in new adsorbate levels that are broadened into resonances and are renormalized toward lower energies by the surface potential in non-transition metals. Presence of the d orbital of transition metals and noble metals, on the other hand, leads to an extra splitting of the renormalized adsorbate levels into bonding and antibonding levels. The position of the d-band center with respect to the Fermi level defines the strength of the interaction between adsorbent and adsorbate. A downshift of the d-band center of the metal results in a less adsorption of the molecule by the surface, while a shift-up of d-band center implies a more reactive surface and higher adsorption propensity [188]. For an N_2 molecule, HOMO (the highest occupied molecular orbital) and LUMO are $3\sigma_g$ and $1\pi_g^*$,

respectively. In the second step, the $1\pi_g^*$ LUMO of N_2 that was initially unoccupied then couples with the d orbital of transition metals, and this gives rise to a downshift of the mostly filled d orbital states and a similar upshift of the empty $1\pi_g^*$ LUMO. Based on the partial density of states (PDOS) distributions shown in Figure **??**(a), we evaluated the d-band center for the various Al systems with (111) surfaces and found that the d-band center shifts up from 2.04 for pure Al to 2.19, 2.56 and 2.49 eV for the surfaces alloyed with Mg, Mn, and Fe, respectively, which again confirms the results shown in Figure 4.15(c). When the d-band center shifts up in energy as in the Mn- and Fe-doped Al alloy cases, the number of anti-bonding states above the Fermi level increases, which results in less-filled anti-bonding states and subsequent stronger bonding.

Figure 4.15(c) also presents the calculated impacts of surface orientations on E_{ad} . The tendency of the surface atom i to attract a molecule can be correlated with the general coordinate number ($\overline{CN}$), $\overline{CN(i)}$=$\sum_{j=1}^{n_i} cn(j)n_j/cn_{max}$, where $cn(j)$ is the coordination number of the neighbor atom j, $n(j)$ is the number of nearest neighbor atoms, and cn_{max} is the maximum coordination number for the atoms in the bulk, respectively [111, 189]. A surface with lower $\overline{CN}$ is typically less stable, and lack of coordination atoms in such an unstable surface may result in a bond formation between the adsorbate and the metallic surface. For FCC crystals, cn_{max} is 12, and $\overline{CN}$ for the atop site in (111) plane is estimated as 7.5. On the other hand, the $\overline{CN}$ values for the atop site on (110) and (100) planes can be computed as 5.17 and 6.67, respectively. These results for $\overline{CN}$ are consistent with the E_{ad} calculations in Fig 4.15(c); the (111) surface is the most stable orientation and the N_2 molecule adsorption onto the (111) surface is less likely. Although the effects of crystallographic orientation are not discernable for pure Al and Al-Mg materials, our calculations clearly show that the (110) plane alloyed with either Mn or Fe will strongly attract N_2.

The PDOS distributions for N_2 adsorption over the (111), (110) and (100) surface planes for pure and alloyed Al systems are shown in Figure 4.16. It was shown that, because of a large HOMO-LUMO gap and a high bond order of N_2, slight change in the electronic structure is expected in N_2 when N_2 molecule is adsorbed to the metal surface [184]. Therefore, we expect that the changes in the electronic structure is mostly affected by the characteristics of the surface including the surface orientations and surface compositions. It was observed that when pure Al surface is cleaved to (111), (100), and (110) planes, 2, 5, and 16% of height contractions in the surface layers occur, respectively [190, 191, 192]. When a bulk metallic crystal is cut to form surfaces, the electrons near

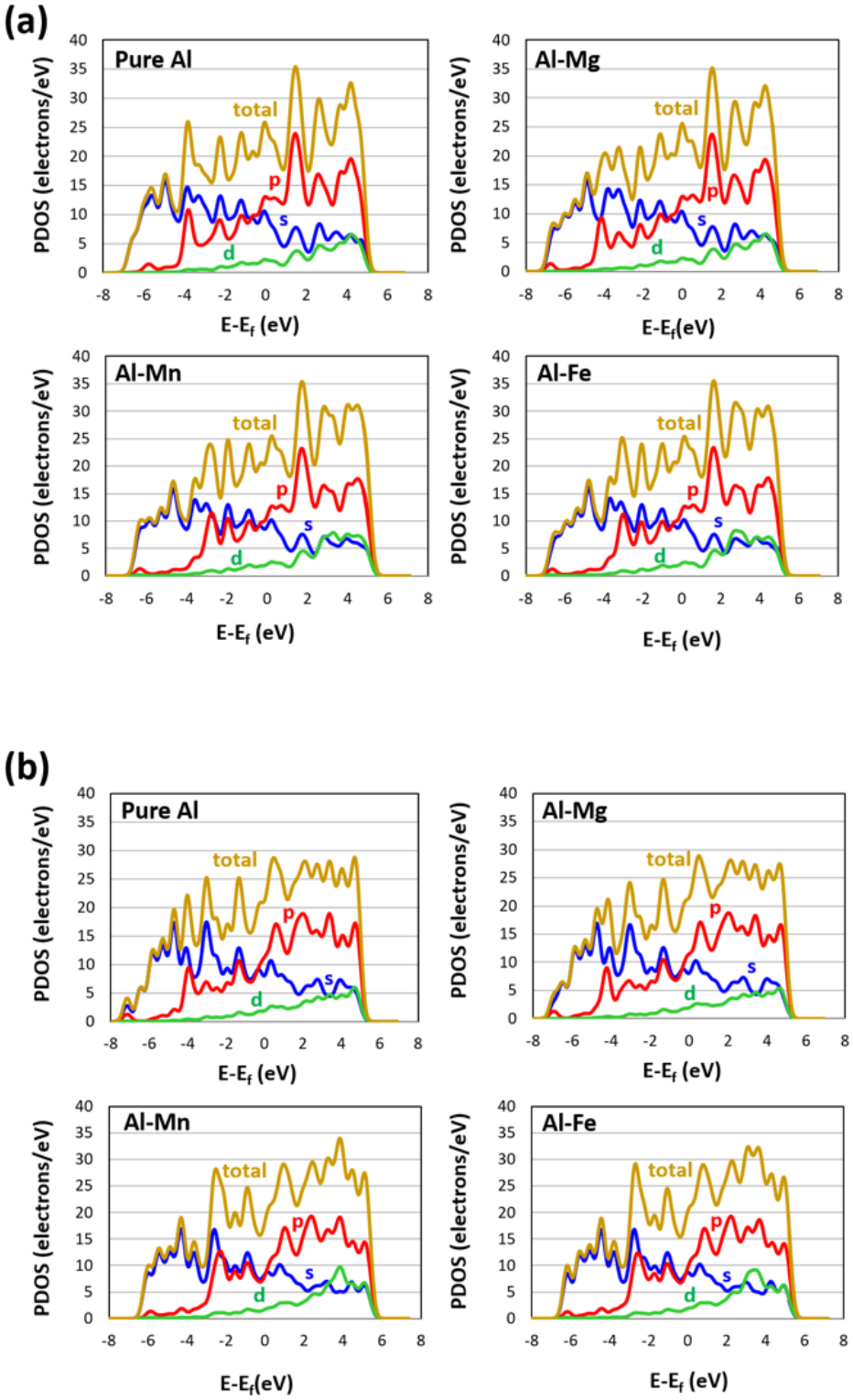

surface atoms rearrange to mitigate the charge-density corrugation and the electrons kinetic energy, and they move toward the bulk, leaving positive ions behind. If the negative charge is concentrated

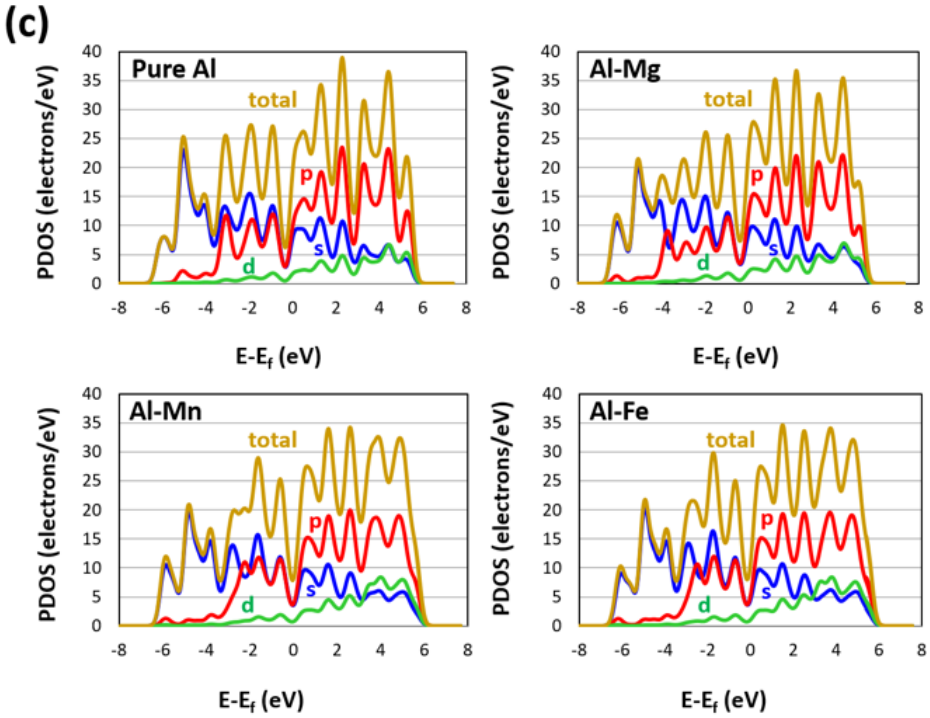

Figure 4.16: PDOS profiles over the (a) (111), (b) (110), and (c) (100) surface planes of pure Al and Al alloys with N_2 adsorption.

in the bulk, the positive ions generated in the initial stage will be attracted toward the bulk atoms due to the Coulombic electrostatic forces. Because of the relatively flat nature of the electronic corrugations for close-packed surfaces, the contraction in the height for these close-packed planes is generally smaller than those for other less compact surfaces. It is clearly seen in Figure 4.16 that the total PDOS distributions for (111) surface show less wrinkles compared with the other two less compact surfaces [193]. Also, the PDOS calculations for Al-N_2 systems including alloying elements show that the presence of Mg, Mn, and Fe does not strongly perturb the electronic structures of the systems.

4.2.2 Absorption and dissociation of N_2

Once the liquid N_2 molecules are physically adsorbed onto the Al surface, they may have a chance to dissociate into their atomic elements and to penetrate into the bulk lattice of Al materials [174, 28]. Such dissociation and/or absorption can happen depending on the degree of mechanical milling energies that will be provided from the milling balls during cryomilling, however, the mechanisms

and required energies for these dissociation and/or absorption phenomena are not well known. Thus, it is crucial to reveal the mechanisms and to assess the amount of energy required for a transformation comprised of N_2 dissociation and absorption inside the Al lattice. Here, we conducted DFT calculations to evaluate the energy barriers for surface penetration and eventually bulk diffusion of nitrogen species. Note that there must be many possibilities for the minimum energy paths (MEP) associated with N_2 absorption into the Al lattices. From the previous results for N_2 adsorption, it was predicted that the N_2 molecule will not dissociate at the adsorption stage. With this, we limit the absorption scenarios to two extreme cases, i) the N_2 molecule dissociates and simultaneously diffuse into the lattice (i.e., N absorption) and ii) the N_2 molecule does not dissociate into its elemental atoms and simply transports inside the Al lattice (i.e., N_2 absorption).

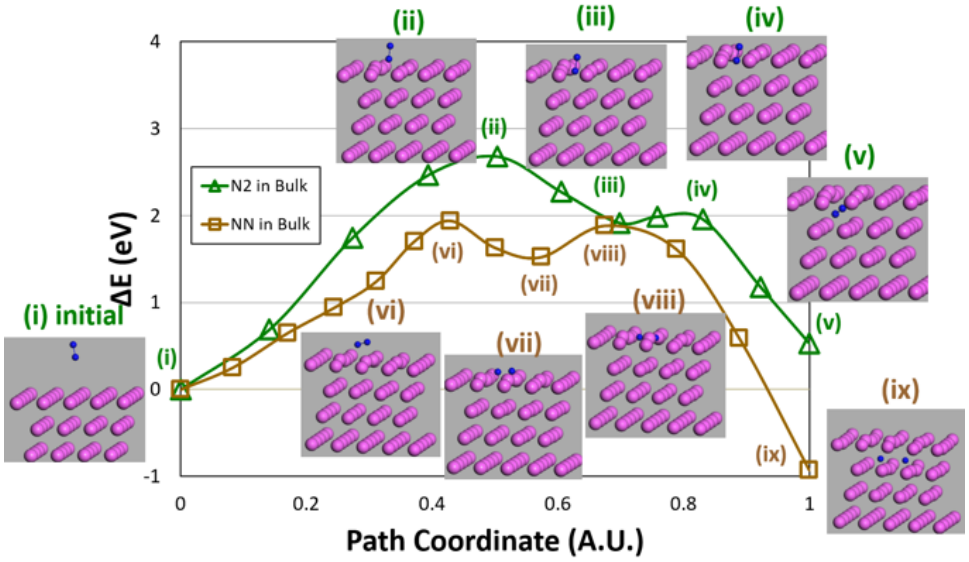

Figure 4.17: Minimum energy path (MEP) profiles upon bulk absorption of N_2 molecule and N atoms through the (111) surface of Al.

Figure 4.17 presents the calculated minimum energy path (MEP) profiles for the absorption of N_2 molecule and two separate N atoms through the (111) surface of pure Al. To set the initial configuration, an N_2 molecule was placed at the atop position. At the adsorption stage (Figure 4.17 (i)), the liquid nitrogen-metal interaction is relatively weak because the adsorption is accomplished by overlapping the N_2 $3\sigma_g$ bonding orbital and the bands of metal surface. After adsorption, donation from N_2 $1\pi_u$ bonding orbital of N_2 to the surface and subsequent back-donation from the surface to the $1\pi_g^*$ orbital occurs. Since the interactions through the π orbitals are more compelling,

the N_2-Al surface interaction becomes stronger while N-N bond becomes substantially weakened, which eventually leads to the dissociation of N_2. The dissociation energy of N_2 over (111) surface of pure Al was calculated as 1.94 eV, which is much smaller than that of isolated state (9.76 eV) [181]. In our study, two distinct representative final configurations were considered for the possibilities of N_2 molecule dissociation upon absorption through the Al lattice. The first configuration consists of N_2 molecule centered in an octahedral site in the first layer under the surface (Figure 4.17 (v)). In Figure 4.17, the MEP profile for this situation is provided using green triangle symbols with detailed atomistic structural images (see Figure 4.17 (ii)-(v)). The second configuration considered two N atoms centered in two neighboring octahedral sites under the (111) surface (Figure 4.17 (ix)), and the MEP profiles are plotted using brown square symbols along with intermediate structural images (see Figure 4.17 (vi)-(ix)). Note that these two final configurations correspond to the representative N_2 and N absorptions on the (111) surface, respectively, in the current study. From the calculated results, we see that molecular N_2 absorption needs to overcome an energy barrier of 2.68 eV while atomistic N absorption requires only 1.94 eV energy by the N_2 dissociation.

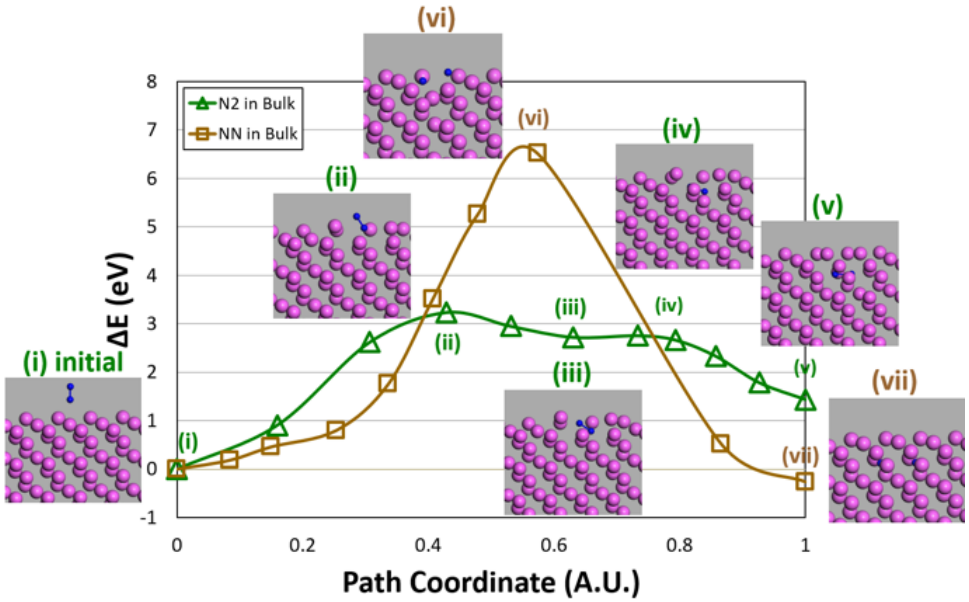

Figure 4.18: Minimum energy path (MEP) profiles upon bulk absorption of N_2 molecule and N atoms through the (110) surface of Al.

When nitrogen species are absorbed through less compact (110) or (100) planes, the dissociation and absorption energy barriers for N atoms were predicted to be much larger than that for (111)

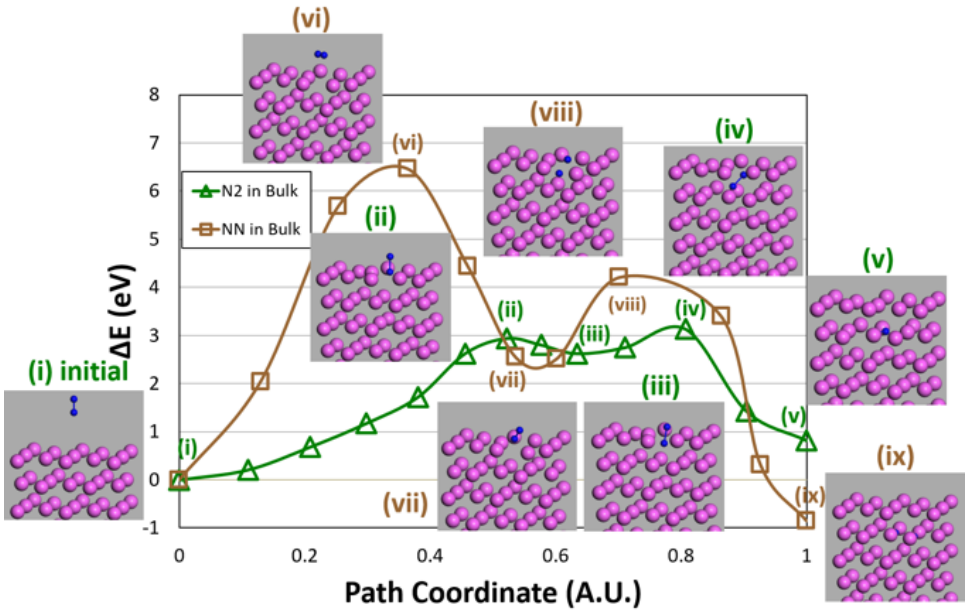

Figure 4.19: Minimum energy path (MEP) profiles upon bulk absorption of N_2 molecule and N atoms through the (100) surface of Al.

plane. Details for the MEP profiles and the atomistic structural configurations starting from physical adsorption of the N_2 molecule over the (110) and (100) surface planes of pure Al materials have been provided in Figure 4.18 and 4.19, respectively. The same symbol types and colors in Figure 4.17 have been used to indicate the N_2 and N absorptions in these figures. From the data presented in Figure 4.18, it was predicted that the molecular absorption of nitrogen over the (110) surface would have an energy barrier of 3.23 eV. On the other hand, the diffusion energy barrier for the dissociative absorption over the (110) surface was equivalent to 6.52 eV, which implies that the dissociation of N_2 would be practically not feasible. Comparable results are identified for the nitrogen absorption through the (100) surface of pure Al, as shown in Figure4.19. The energy barriers for these loosely packed surfaces were similar, and the energy required for molecular absorption through the (100) surface of pure Al was estimated to be about half of the equivalent energy for dissociative absorption with numerical values of 3.13 eV and 6.46 eV, respectively. These results could be originated from the less likelihood of the strong interaction between nitrogen and Al surface atoms upon the dissociation procedure due to the smaller atomic density on the Al surface. From Figure 4.17-4.19, it is seen that the N_2 molecule approaches with its vertical configuration if the dissociation of N_2 is not assumed (i.e., N_2 absorption in the bulk octahedral site) regardless

of the surface orientations. On the other hand, when considering the dissociation of N_2 (i.e., N absorption), the N_2 molecule horizontally approaches to the Al surface. One can readily notice that a horizontal adsorption of N_2 to a relatively compact surface such as (111) results in the dissociation of N_2 prior to the surface penetration. However, when the absorbing surfaces are (110) and (100), the dissociation of N_2 takes place below the surface, which can render the dissociation energy barrier much larger than those of the (111) system and other (110) and (100) systems without N_2 dissociation. The MEP profiles in Figure 4.17-4.19 generally exhibit two peaks. The first peak in the absorption process is associated with the energy barrier for the N_2 molecule access to the metal surface. The energy of the system becomes lower in the intermediate state by forming a thermodynamically stable adsorbate-surface combination, except one case where a bond formation was detected between the absorbing N and surface atoms (see Figure 4.18, N absorption over the (110) surface). In this case of dissociative absorption, the N_2 debonding (i.e., breaking of triple N_2 bonding) occurs at this stage, too, which can explain the high energy barrier without a local energy minimum as shown in Figure 4.18. The second peak is related to the penetration of N/N_2 to the bulk in searching for stable octahedral sites. With these, it is predicted that the N_2 dissociation and subsequent absorption over (110) or (100) planes is much less likely.

Also, one can readily find that the final energy states of N_2 absorption are higher than the initial energy states for all cases if no N_2 dissociation is assumed. On the contrary, as shown in Figure 4.17-4.19, after dissociative absorption, the relative total energies of the final system with respect to the total energies of initial configuration all decrease, which manifests the higher stability of the Al lattice containing dissociated N atoms. These results can imply that the nitrogen embedded in the Al metal-matrix is likely to take the atomic form and these can happen with relatively low energy barrier through the absorption/dissociation of N_2 over (111) plane of pure Al, which cannot be easily revealed by experimental characterization tools; although there are many previous reports regarding the nitrogen contents in nanocrystalline Al alloys/composites, however, it is still not clear whether the nitrogen contained in the bulk materials is N_2 or N.

4.2.3 Diffusion of N_2 and N in the bulk alloy

Although the absorption energy barrier for non-dissociative nitrogen is relatively high on the Al-based surfaces, it is thought that there still are chances for the presence of either atomistic or molec-

ular nitrogen inside the Al crystals, because the mechanical forces from milling during cryomilling will assist the absorption of nitrogen species. Also, note that we tested the nitrogen absorption only over the major (111), (110), and (100) surfaces, and there might be other pathways, although they are not likely to possess high probabilities. Therefore, we assumed that, depending on the adsorption surface types, both atomic and molecular nitrogen could be present in the bulk Al lattice. Considering that these two probable scenarios, we provide the calculation results regarding the diffusion energy barrier and the corresponding MEP profiles for both N and N_2 in the bulk lattices of pure and alloyed Al systems.

Figure 4.20 shows the calculated MEP profiles for (a) N atom and (b) N_2 molecule between adjacent octahedral sites along with detailed atomistic structural snapshots in various Al systems. As previously addressed, the diffusion through the octahedral sites was tested in this work because the octahedral site is the largest interstitial site in the FCC crystal with the highest stability containing interstitial nitrogen species. When travelling through sequential octahedral sites, the nitrogen (N or N_2) would take a longer but lower energy barrier path by passing through the intermediate tetrahedral site in the crystal [127]. In this case, the degree of lattice distortion is much smaller compared with the distortion resulting from the shorter path linearly linking the initial and final octahedral positions. From Figure 4.20(a), it is shown that the MEP profiles of the N atom projectiles exhibit nearly symmetric curves. The diffusion energy barrier of N atoms in pure Al was calculated as 0.71 eV, which is higher than the barrier of smaller atoms such as H (0.16 eV) [194]. In the figure, the diffusion energy barrier of N atoms in pure Al (0.71 eV) is lower than those in the alloyed systems. This can be explained by the lattice distortion induced by the presence of alloying elements; because the size of the N atom is relatively small, the transport of nitrogen species is feasible through larger interstitial sites. On the other hand, as Figure 4.20(a) presents, by increasing the size of alloying element from Fe and Mn to Mg, a greater distortion in the lattice results in less likelihood of diffusion with higher energy barriers. In contrast to the N case, the MEP profiles of N_2 through sequential octahedral sites showed double local maxima with a barrier height of 1.25 eV. The structural images provided in Figure 4.20(b) show large distortions in the Al lattice during diffusion. In these cases, such extra distortion in the lattice prior to diffusion opens the path for the relatively large N_2 molecules that can facilitate the N_2 transport. As shown in Figure 4.20(b), pure Al exhibits the highest energy barrier for diffusion,

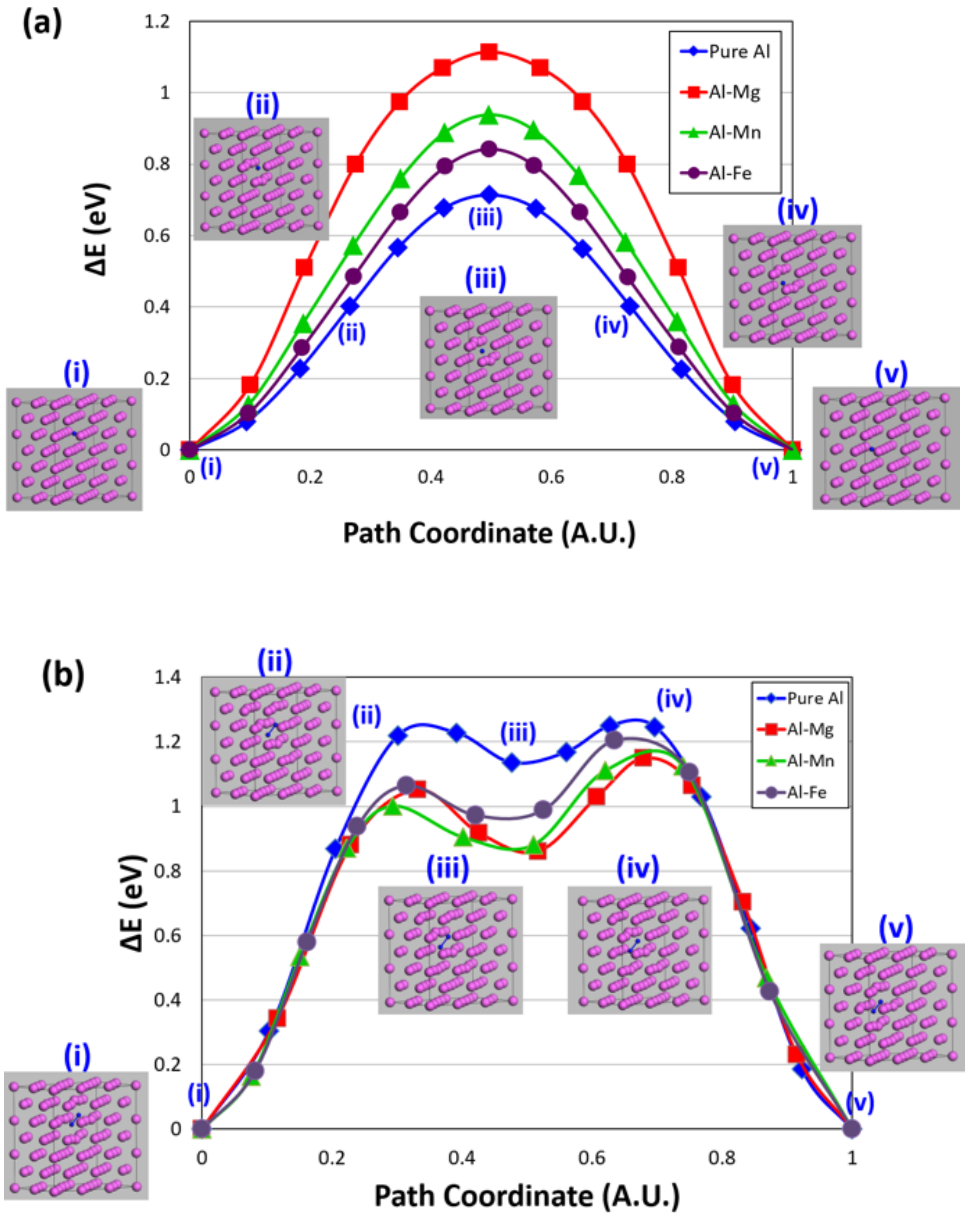

Figure 4.20: Minimum energy path (MEP) profiles for (a) N atom and (b) N_2 molecule through the octahedral sites in various Al systems.

and as the size of alloying element increases from Fe and Mn to Mg, the diffusion energy barrier consecutively decreases due to the larger lattice distortion. When the N_2 molecule starts to diffuse from one octahedral site to the adjacent octahedral site, the N atoms in N_2 can form some meta-stable bindings with the Al lattice atoms, and as the molecule diffuses, the old meta-stable bonds are disconnected and newer meta-stable bonds can form. This can explain the double local maxima with two peaks in the MEP profiles shown in Figure 4.20; the two peaks are associated with the

breaking of the meta-stable bonds. Because the bonding strengths of these two meta-stable bonds are similar in pure Al, the two MEP profile peaks in pure Al display similar heights. Note that the intermediate minima correspond to the state that the two N atoms of N_2 are bonded to a shared middle atom. In the alloyed systems, this shared atom is modelled as the alloying element, and breaking of the two N bonds (i.e., 2nd peaks for alloyed systems in Figure 4.20(b)) with the alloying element is more difficult compared with breaking of the N bonds (i.e., 1st peaks for alloyed systems in Figure4.20(b)) with Al atoms. Therefore, the MEP profile heights for the 2nd peaks are larger than those for the 1st peaks in the alloyed systems. Although a local minimum is observed in the N_2 MEP profile, it is predicted that a relatively higher amount of energy is required compared with N diffusion, therefore, molecular diffusion of N_2 is less likely to occur and the dissociation of N_2 may be accompanied for the diffusion process of nitrogen in Al lattice. It must be again noted that the general consideration for the diffusion of nitrogen species in this work is based on the octahedral interstitial configurations with higher energetic stability of Al lattices. Although it is highly unlikely due to relatively high energies of other structures, there might be other avenues for the transport of N/N_2 in the Al crystals.

4.3 Mg corrosion behavior

4.3.1 Surface energies

The surface energies of Mg/Mg alloys were first calculated to examine the impacts of surface crystal orientation and the impurity elements. The surface energy, γ, for pure Mg materials can be typically calculated by the following equation,

$$\gamma_{pure} = \frac{E_{Mg}^{slab,relaxed} - 0.5 n_{Mg} E_{Mg}^{bulk} - 0.5 E_{Mg}^{slab,unrelaxed}}{A} \tag{4.4}$$

Where $E_{Mg}^{slab,relaxed}$ is the total energy of the vacuum slab after the geometry optimization, E_{Mg}^{bulk} is the total energy of bulk Mg unit cell, n_{Mg} is the ratio of the number of atoms in the slab to the Mg unit cell, $E_{Mg}^{slab,unrelaxed}$ is the total energy of the vacuum slab without geometry optimization (i.e., all atomistic positions are fixed), and A is the surface area in the slab, respectively. Note that Eq. is used to calculate γ of relaxed surface only, while $\gamma_{pure} = \frac{E_{Mg}^{slab,relaxed} - n_{Mg} E_{Mg}^{bulk}}{2A}$ is typically used

to calculate the average γ of unrelaxed and relaxed surfaces. For the surface energy computations including an impurity element (e.g., Al, Zn, or Y) on the surface, one middle Mg atom on the surface was replaced by one of the three alloying elements. When an alloying element is incorporated onto the Mg surface, the expression for the surface energy, γ, of the alloyed surface must be modified and is expressed in Eq. 4.5,

$$\gamma_{pure} = \frac{E_{Mg-alloy}^{slab,relaxed} - 0.5n_{Mg}E_{Mg}^{bulk} - 0.5n_{alloy}E_{alloy}^{bulk} - 0.5E_{Mg-alloy}^{slab,unrelaxed}}{A} \tag{4.5}$$

Where $E_{Mg-alloy}^{slab,relaxed}$ is the total energy of the vacuum slab including an alloying element after the geometry optimization, E_{Mg}^{bulk} is the total energy of bulk Mg unit cell, n_{Mg} is the ratio of the number of atoms in the slab to the unit cell, E_{alloy}^{bulk} is the total energy of bulk unit cell of alloying element, n_{alloy} is the ratio of the number of atoms in the slab to the unit cell of alloying element, $E_{Mg-alloy}^{slab,unrelaxed}$ is the total energy of the vacuum slab including an alloying element without geometry optimization (i.e., all atomistic positions are fixed), and A is the surface area in the slab, respectively.

Table 4.6: Calculated surface energies (kJ/mol) of Mg systems with different surface planes and alloying elements.

Surface planes	Alloying elements	Surface energies (kJ/mol)
Basal	None	33.02
	Al	31.07
	Zn	31.46
	Y	31.51
Prism	None	102.14
	Al	100.48
	Zn	100.71
	Y	100.57
Pyramidal	None	124.11
	Al	120.39
	Zn	120.65
	Y	122.63

The calculated surface energies (in kJ/mol) of the pure Mg and Mg alloys using Eq. 4.5 is provided in Table 4.6. The calculated surface energy of the pure Mg system with basal surface plane orientation was 33.02 J/mol and this can be converted into 0.62 J/m^2, which shows a good agreement with the previously calculated value (0.64 J/m^2) based on a pseudopotential approach

[195]. It is in-between other two previously reported surface energies of Mg basal plane, i.e., 0.29 J/m^2 based on the valence electron structure by empirical electron theory (EET) [128] and 0.76 J/m^2 from experimental measurements [196]. As discussed in [128], the result from EET calculation requires some modifications for the additional value of the free energy with forming of new surface. As shown in Table 4.6, the calculated surface energies exhibit a reverse relationship with the atomic density of the surface plane; the atomic densities of basal, prism, and pyramidal surface planes of Mg are 0.041, 0.060, 0.112 $atoms/A^{\circ 2}$, respectively. It was also found that all of the alloying elements lower the surface energies, which implies that addition of the alloying elements of Al, Zn, and Y would result in more stable surfaces. However, given the scales of the calculated surface energies, the crystallographic surface orientation is the most influential factor in determining the surface energy values of the Mg/Mg alloy systems.

4.3.2 Water adsorption on Mg/Mg alloys surfaces

The degree to which the water molecule gets adsobed to the metal surface signifies the vulnerability of metal for corrosion and it is the starting point of the degradation/corrosion process in an aqueous environment. Knowledge on the interaction of water molecule with the surface, thus, would be essential to understand the hydrolysis process of metals. Although the bulk formation energy of hydroxide films is an important factor in determining the degradation rates of Mg/Mg alloys and the quantitative relationship between the water molecule adsorption and metal surface degradation is not firmly established, the extent of attraction or repulsion of a water molecule to the surface is also one of the important factors to elucidate how much the surface could be passivated against the water molecule interactions. As the first effort, to study the hydrolysis behavior of the Mg/Mg alloy, we analyzed the respond of metal surface to the approach of water molecule. With this concern we tested the stability of a water molecule for various molecular configurations and orientations. Figure 4.21 shows two examples of unstable water molecule over the 'atop' position of the (0001) Mg surface. In the figure, the green, red, and white spheres represent Mg, O, and H atoms, respectively. Note that the same color notation is used through the structural images contained in the entire manuscript. In the figure, the initial water molecule contains an O-H bond in parallel to the Mg surface and another O-H bond tilted either away from or towards the Mg surface. After geometry optimization, these water configurations are changed to the upright or the downward

orientations, respectively, indicating that the initial configurations are unstable. Based on various initial configuration tests, it was found that the upright orientation is one of the most stable water molecule configurations; e.g., the total energy of upright configuration was much lower than that of downward configuration. Figure 4.22 (a) presents such upright configuration of a water molecule adsorbing to the atop position of the (0001) Mg surface. The average equilibrium distance from the surface for this upright configuration over atop position was 2.00 $\mathring{A}$, which could be varied depending on either the types of the alloying elements on Mg surface or the sites of adsorption. Figure 4.22 (b) is the schematic illustration of the side view of adsorption, where α is the tilting angle between the Mg surface plane and the molecular dipole moment plane (i.e., the plane consists of two H atoms and one O atom). It is crucial for the water molecule to appraoch the metal surface with certain orientation, because this orientaion will affect the response of water molecule to an applied electrochemical field, metal dissolution, and molecular dissociation of adsorbent. These water molecule configurations with simultaneous tilted O-H bonds were also found to be stable. Calculations reported in Figure 4.22 (c) show the dependence of the adsorption energy on the tilting angle (α). In this calculation, when the dipole moment plane of the water molecule is parallel to the Mg surface, the tilting angle was set as $\alpha = 90^\circ$ (see Figure 4.22 (b)). The upright configuration with the O atom pointing to the surface is therefore defined as $\alpha = 0^\circ$. The following Eq. 4.6 quantifies the adsorption tendency of the surface for a water molecule.

$$E_{ad} = E_f - E_{slab} - E_{water} \tag{4.6}$$

Where E_{ad} is the adsorption energy, E_f is the total energy of the Mg/Mg alloy systems containing a water molecule, E_{slab} is the total energy of Mg/Mg alloy slab system without a water molecule, and E_{water} is the energy of an isolated water molecule. The alignment of the water molecule over the atop position was geometry optimized and a tilting anlge of $\sim 10^\circ$ was calculated for the configuration with the highest stability. It was found that the adsorption energy variations for the tilting angles between 10-47° ranges are very small but E_{ad} increases as α increases to 90° after $\sim 47^\circ$. The water molecule mixes with the Mg surface through its higher energy occupied molecular orbitals, $3a_1$ and $1b_1$, which are the molecular orbital (MO) from mixing the O $2p_z$ atomic orbital (AO) and the H σ MO, and the nonbonding MO from oxygen $2p_x$ AO, respectively. Comparing the

electron density for the equilibrium configurations with 10° tilt angle and the upright ($\alpha = 90°$) in Figure4.22 (d) reveals that the upright water molecule will favor the interaction through the $3a_1$ orbital because it is in the C_{2v} symmetry plane of the molecule, while the $1b_1$ orbital, which is orthogonal to this and antisymmetric about a mirror plane in the molecule, is the preferred orbital for flat adsorption of the water molecule. Also, it is seen that the partial density of states (PDOS) of the electrons for the upright configuration varies through a wider range of energies compared to that of the 10° tilting angle configuration. From these results, it is likely that a water molecule would have a tilted ($10-47°$) configuration when it is adsorbed onto the atop position of the (0001) Mg surface.

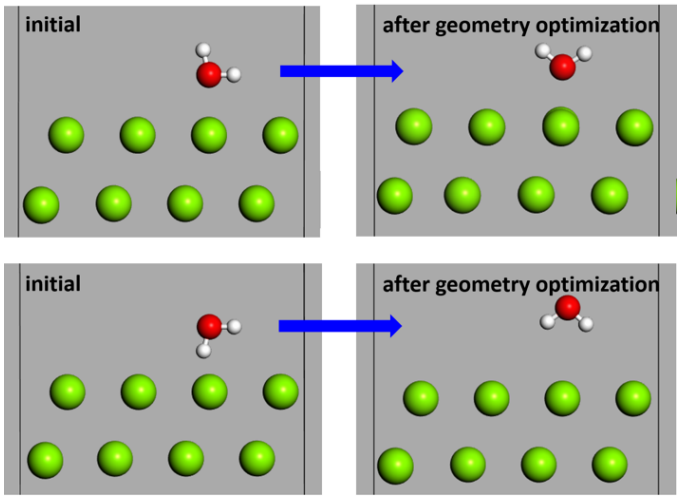

Figure 4.21: Examples of unstable configurations of a water molecule over the atop site of Mg surface

After analyzing the adsorption behvaior on the atop posirion, we tested the adsorption energies over different sites (i.e., bridge, hollow 1, and hollow 2 positions) of the basal Mg surface with various water molecule tilting angles. These low-index high-symmetric positions are defined using Figure4.23(a). The hollow 1 site differs from the hollow 2 site by having an underlying Mg atom of the 2^{nd} layer from the surface. Although the adsorption of a water molecule with a tilting angle of $10-47°$ was thermodynamically preferred over the atop site, the geometry optimization of a water molecule with tilting angles less than 90° over the bridge, hollow 1, and hollow 2 sites of the Mg surface showed high instability. Therefore, for in-plane tracking of a water molecule over the Mg surface, we considered the vertical orientation (i.e., upright configuration) of a water molecule for direct comparison. Upon adsorption, the water molecule acts as an electron donor

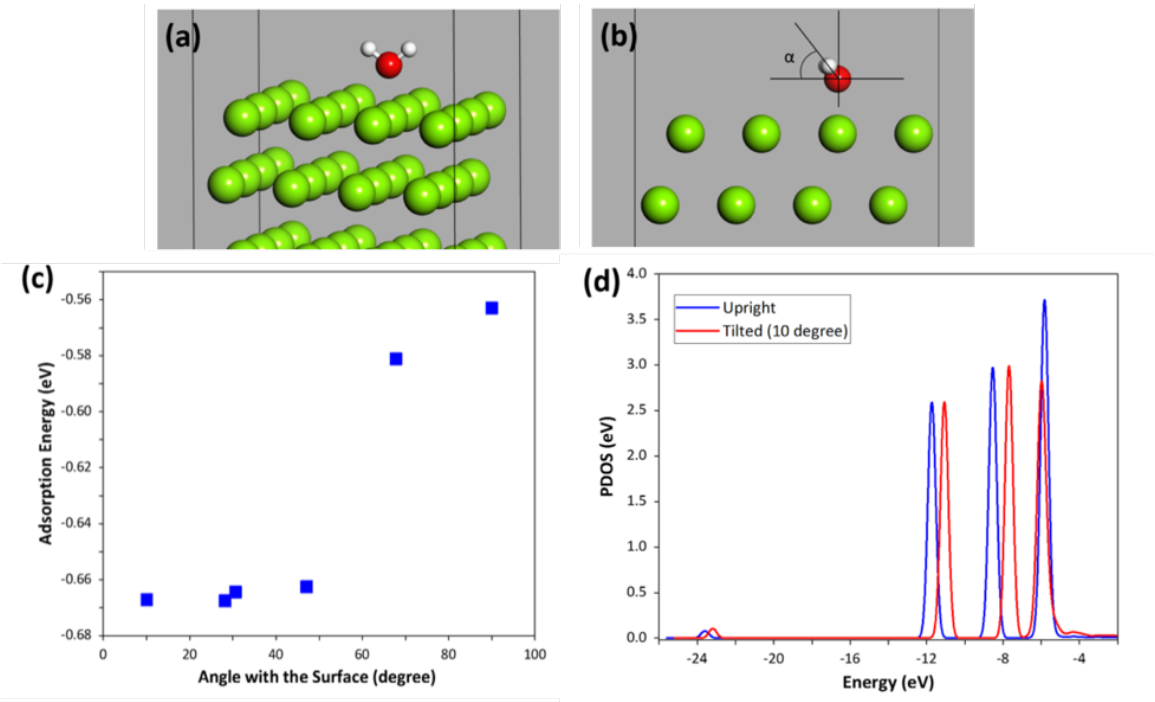

Figure 4.22: Schematics of (a) water molecule adsorption over the atop position of pure Mg surface and (b) the side view to illustrate the tilting angle (α) between water molecule and pure Mg surface, (c) calculated adsorption energies with various tilting angles (α), and (d) partial density of states (PDOS) for p orbital of water molecule with upright and 10 tilted configurations.

and the substrate serves as an electron acceptor; the Mulliken population analysis confirms that a water molecule provides $0.1e^-$ to the metal. The potential energy surface is relatively smooth for adsorption energy of a water molecule on the basal plane of pure Mg; transferring between the bridge site and both of the hollow sites requires small activation energies. The energy barrier considerably increases only when a water molecule travels from any of these three sites to the atop position. The energy barrier for such transformation was approximately ~ 0.14 eV. For the more stable system with a water molecule with a tilting angle of $10-47°$, the adsorption energy difference between the atop site and the other sites is ~ 0.25 eV. The data presented in Table 1 and the contour map of Figure 3(b) show the adsorption energy changes with the upright water molecule configuration in different adsorption sites of the Mg surface, implying that the atop position is the most preferred site and the bridge site exhibits a similar level of energy with the hollow sites. These results are in agreement with previous studies that reported favoring adsorption of a water molecule on the atop position of close-packed surfaces of HCP and FCC metals (i.e., Au, Ag, Cu and Ru) [197, 126]. We also observe that the geometry of the water molecule changes upon adsorption; the intramolecular

H-O-H angle (θ) increases from 104.4 before adsorption to $\sim 109°$ for the atop site and to $\sim 107°$ for the rest of the adsorption sites. In addition, it was found that the O-H bond length does not noticeably elongate for the molecule adsorbed to the surface compared to the water molecule in the gas phase (i.e., isolated molecule).

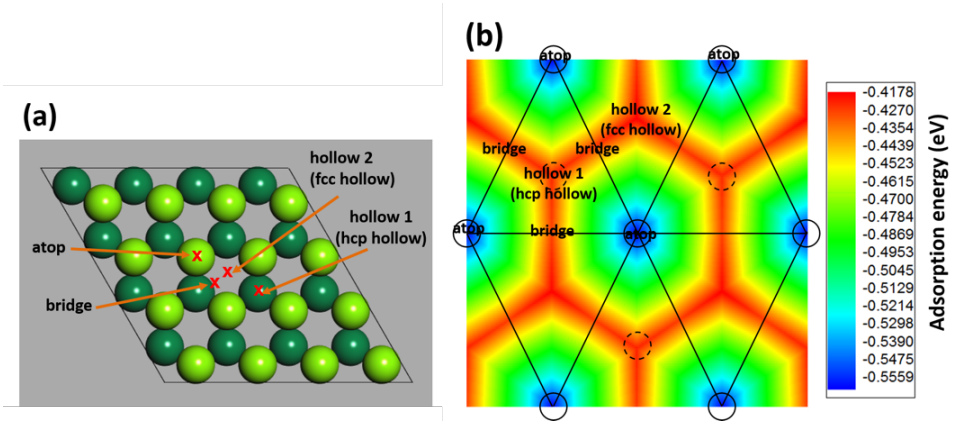

Figure 4.23: (a) High-symmetric adsorption sites on the basal (0001) surface of Mg and (b) in-plane contour map to show the adsorption energy on the basal (0001) surface of Mg.

Table 4.7: Calculated adsorption energies (E_{ad}), surface-oxygen distances (d_{O-S}), O-H bond distances (d_{O-H}), and H-O-H angles (θ_{H-O-H}) for a water molecule adsorbing onto the basal plane of pure Mg system.

Mg surface plane	Alloying elements	Adsorption sites	$E_ad(eV)$	$d_{O-S}(\AA)$	$d_{O-H}(\AA)$	$\theta_{H-O-H}(\circ)$
Basal	None	Atop	-0.5629	2.189	0.976	109.045
(0001)		Bridge	-0.4265	1.97	0.985	107.914
		Hollow 1 (hcp hollow)	-4177	2.157	0.983	107.128
		Hollow 2 (fcc hollow)	-0.4229	2.0881	0.985	107.321

The calculated partial density of states (PDOS) of the adsorbing water molecule for these adsorption sites over the (0001) surface are reported in Figure 4.24. In this figure, the curves correspond to the PDOS projected onto the p orbitals of the water molecule. The adsorption of a water molecule with upright configuration involves the $3a_1$ orbital of which energies are located at about -6 eV. The density of electron states for this energy varies depending on the in-plane position of the O atom. The corresponding peaks in Figure 4.24 approach -6 eV for the atop case and shift toward more negative energy levels for the bridge site (-7 eV), indicating a more stable configuration of electron states in the atop position with more compact distribution of PDOS. The density of electron states does not change significantly from the bridge site to the hollow sites.

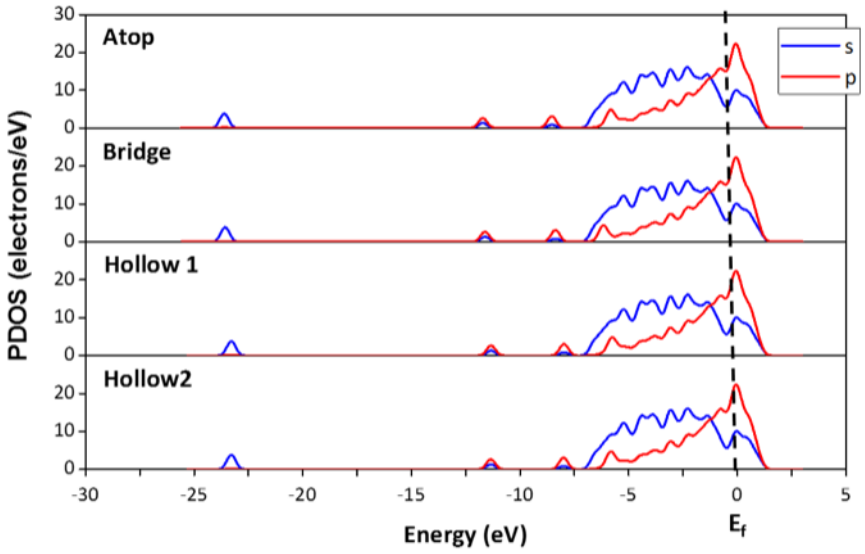

Figure 4.24: Partial density of states (PDOS) for the water molecule adsorbing on different sites of pure Mg (0001) basal plane. The curves correspond to PDOS of the p orbitals. E_f indicates the Fermi energy level.

The water/metal adsorption energy for pure Mg and Mg alloys with Al, Zn, Ca, and Y with different surface crystallographic orientations were calculated as the next step. In this set of computations for alloyed systems, we replaced one of the surface atoms with an alloying element and observed the adsorption behavior based on the energy changes from the interaction of the alloying atom and the water molecule. To better examine the interaction between the alloying elements and a water molecule, the upright configuration was chosen for the water molecule to minimize the direct influence of Mg atoms. These initial configurations were geometry optimized without any constraints for the water molecule to find local energy minima.

In Figure 4.25, we show the calculated adsorption energies for the systems with various alloying elements and surface plane orientations. For the Mg surface orientations, the same three low-index planes of the basal , prism , and pyramidal surfaces were considered. From the figure, it is clearly seen that the adsorption energies are higher in the systems with a more compact basal orientation surface and the adsorption energies in the prism and pyramidal surface systems are nearly similar for most of the cases except the Mg-Zn alloy. In the Mg-Zn alloy, the adsorption energy in the less compact pyramidal surface was lower than that in the prism surface. For all the compositions of the Mg/Mg alloys, the basal plane would weakly attract the water molecule, and the other planes with lower atomic density interact with the water molecule more significantly. This tendency is in

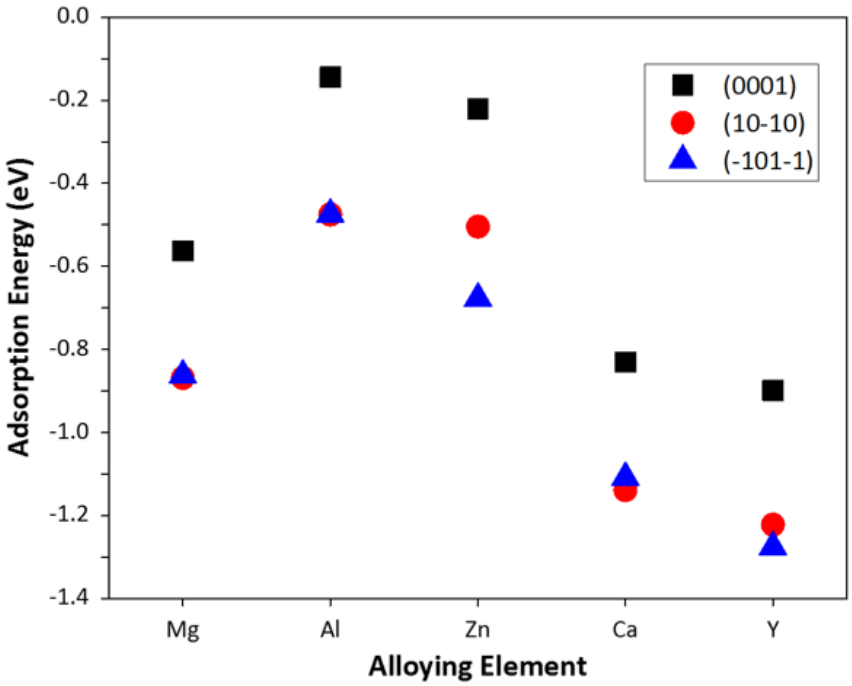

Figure 4.25: Calculated adsorption energies of water molecule on Mg-based surfaces with various alloying compositions and crystallographic surface orientations.

line with the experimental observations for the texture effect on the corrosion behavior of AZ31 Mg alloys [87]. Furthermore, the trend of this adsorption energy could be highly correlated with the general coordination number ($\overline{CN}(i)$ of the basal(0001), prism ($10\bar{1}0$), and pyramidal ($\bar{1}01\bar{1}$) surfaces. Lower $\overline{CN}$ surface is typically less stable, which attracts the adsorbent more strongly. $\overline{CN}$ of surface atom i (i.e., $\overline{CN}(i)$) can be quantified by the following Eq. (2) [111].

$$\overline{CN}(i) = \sum_{j=1}^{n_j} \frac{cn(j)n_j}{cn_{\max}} \tag{4.7}$$

Where $cn(j)$ is the coordination number for the neighbor atom j, n_j is the number of nearest neighbor atoms, and cn_{max} is the highest coordination number of the system for the atoms in the bulk, respectively. The $\overline{CN}$ values for (0001), ($10\bar{1}0$), and ($\bar{1}01\bar{1}$) surfaces are calculated as 7.5, 5.33, and 5.3, respectively, which clearly manifests that the adsorption energy for more compact (0001) surface with higher $\overline{CN}$ is much higher than those for other low-index surfaces.

The composition of Mg surface also influences the degree of attraction to the Mg-based substrate. As the data summarized in Figure 4.25 portrays, Al and Zn increase the resistance of the alloy in

adsorbing the water molecule, while other elements including Ca and Y bring the adsorption energy down to more negative values in comparison to the pure Mg system, which can render the alloy relatively vulnerable to degradation in water environments. Also, from Figure 4.25, it could be inferred that, qualitatively, the variations in the degree of water attraction from systems with different low-index surface planes are comparable to those from the systems with different alloying elements. Table 4.8 summarizes the calculated adsorption energies (E_{ad}), surface-oxygen distances (d_{O-S}), O-H bond distances (d_{O-H}), and H-O-H angles (θ_{H-O-H}) for a water molecule adsorbing onto the atop position of various low-index planes in pure Mg and Mg alloy systems. The water molecule orientations mostly maintained the upright configuration except the pyramidal plane cases doped with Zn and Y. From the table, one can easily find that d_{O-S} decreases as E_{ad} decreases with a stronger interaction between the water molecule and the surface.

Table 4.8: Calculated adsorption energies (E_{ad}), surface-oxygen distances (d_{O-S}), O-H bond distances (d_{O-H}), and H-O-H angles (θ_{H-O-H}) for a water molecule adsorbing onto various low-index planes of pure Mg and Mg alloy systems.

Mg surface plane	Alloying elements	$E_{ad}(eV)$	$d_{O-S}(\AA)$	$d_{O-H}(\AA)$	$\theta_{H-O-H}(\circ)$
Basal	None	-0.5629	2.189	0.976	109.045
(0001)	Al	-0.1443	3.972	0.972	103.942
	Zn	-0.2207	3.249	0.971	105.1
	Ca	-0.8304	2.373	0.974	107.145
	Y	-0.8985	2.422	0.972	108.34
Prism	None	-0.8683	2.186	0.975	108.511
$(10\bar{1}0)$	Al	-0.4752	3.422	0.971	105.79
	Zn	-0.5043	4.069	0.97	104.864
	Ca	-1.1383	2.381	0.974	107.37
	Y	-1.2214	2.422	0.972	108.561
Pyramidal	None	-0.8623	2.202	0.975	107.729
$(\bar{1}01\bar{1})$	Al	-0.4748	2.389	0.974	107.904
	Zn	-0.6771	2.725	0.974	103.67
	Ca	-1.1088	2.395	0.974	106.561
	Y	-1.2753	1.539	0.979	107.756

A polar water molecule has a dipole moment in which there exist partial negative charges on its O side and partial positive charges on the H atoms. Calculating the Coulombic forces between the alloying elements and the O side of the water molecule can qualitatively dictate the relative

attraction force between the adsorbing water molecule and the alloyed surface. The Coulombic attraction force between Al atom and the water molecule is weaker than the attraction force in pure Mg. This force even becomes repulsive in the case of containing Zn as an alloying element. Although the Zn atom on the Mg surface possess partial negative charges that can cause repulsion of the adsorbing water molecule, it was calculated that the adsorption to the Mg surface is still favorable, as the adsorption energy is negative (as shown in Figure 4.25). The Coulombic forces between alloying elements and the water molecule are either stronger or similar to the pure Mg case when Ca or Y were employed as alloying atoms, which may result in higher attraction of the water molecule toward the Mg surface. It was found that the partial charges for Mg, Al, Zn, Ca, and Y are 0.13, 0.08, -0.16, 0.35, and 0.14 eV, respectively, at the equilibrium state of water adsorption over the atop site. The partial charge of corresponding O atoms was in the range of -0.90 to -0.94 eV. As Figure 4.25 presents, all of the studied compositions demonstrate negative adsorption energies. Therefore, attraction of a water molecule to the Mg surface is thermodynamically favorable. The binding energies to the water molecule are in the range of -0.14 eV and -1.24 eV. Since the hydrogen bonding energy between two or more water molecules is in the upper band of this range (about -0.25 eV [110]), the water-substrate interactions could be energetically competitive with the water-water bonding especially when the adsorption energy is relatively small (such as adsorption in the Mg-Al or Mg-Zn systems). With highly negative adsorption energies, on the other hand, it is likely that the water-substrate interactions would be dominant and adsorption would not be strongly affected by the hydrogen bonding among multiple water molecules.

In Figure 4.26, we show the calculated distributions of partial density of states (PDOS) of the adsorbing water molecule onto the basal plane of the Mg surface containing various alloying elements. The blue, red, and green colors represent PDOS of s, p, and d orbitals, respectively. The results in Figure 4.26 can explain the reason for a higher adsorption propensity of the water molecule onto the Mg-Ca and Mg-Y surfaces. The PDOS profiles from s orbitals in the figure show nearly similar distributions for all of the systems. However, it is seen that the differences in the adsorption behavior of the alloys primarily arise from the changes in the PDOS of p orbitals. In this figure, the systems including a water molecule adsorbing to Mg-Al and Mg-Zn surfaces exhibit relatively prominent peaks of p orbitals at around -5 eV, which is related to the energy state of $1b_1$ orbital. Further, both Mg-Ca and Mg-Y alloys in contact with the water molecule show sharper

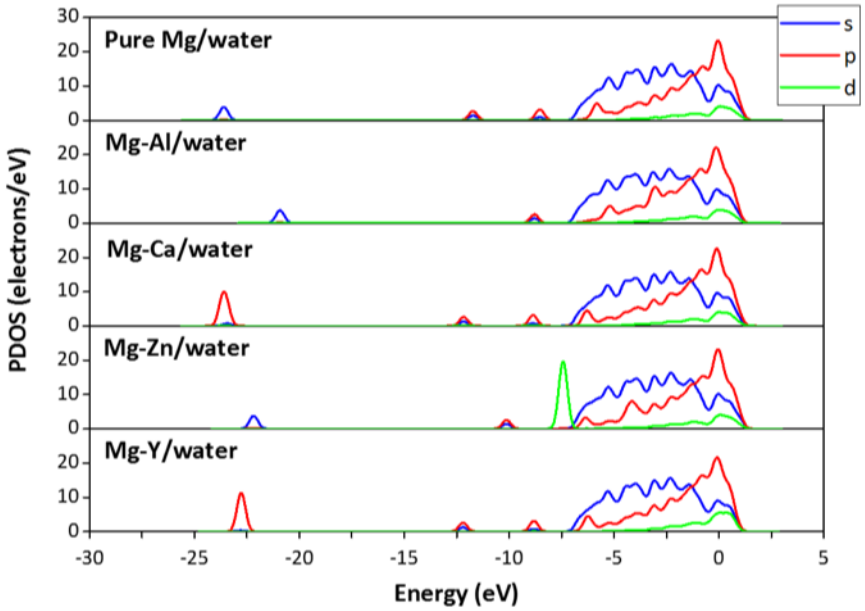

Figure 4.26: Partial density of states (PDOS) for the water molecule adsorbing on the atop sites of Mg/Mg alloy basal plane. The blue, red, and green curves correspond to PDOS of the s, p, and d orbitals. E_f indicates the Fermi energy level.

peaks at around -23∼24 eV, which is the energy state associated with the $2a_1$ orbital (MO from mixing of the oxygen 2s AO and the hydrogen σ MO). In addition, adsorption of a water molecule to the Mg-Al and Mg-Zn surfaces shifts the position of the PDOS peak at -10 eV toward more negative energy states, which is the typical characteristics of the $1b_2$ orbital (MO from mixing the oxygen $2p_y$ AO and the hydrogen σ^* MO).

4.3.3 Surface energy and electrode potential shift of Mg/Mg alloys

Depending on the stability and response of the surface to the attraction forces, when the metal surface interacts with a water molecule, the hydrolysis behavior of the alloy could be varied. Other than these water molecule adsorption perspectives, the degradation rates of Mg surface can be correlated with the surface energy [87, 115]. The calculated surface energies with various alloying elements and surface planes are listed in Table 4.9. Due to a higher stability of the surfaces with higher packing densities, the activation energy for dissolution in close-packed surfaces is higher and removing metallic ions from these surfaces is more difficult. The table also contains the calculated relative Δd_{12} (i.e., the relative difference in the 1^{st} and 2^{nd} layers of a surface plane with respect to the pure Mg system) values. The trends in Δd_{12} for the low-index surface planes with various

alloying elements are in general correlated to the corresponding surface energies; when the surface energy of an alloy is lower, then the calculated relative Δd_{12} is mostly negative, which supports a higher stability of the corresponding surface.

Table 4.9: Calculated surface energies (kJ/mol) and relative Δd_{12} (%) of Mg systems with different surface planes and alloying elements.

Surface planes	Alloying elements	Surface energies (kJ/mol) [127]	Relative Δd_{12}%
Basal	None	33.02	0
(0001)	Al	31.07	-0.034
	Zn	31.46	-1.48
	Ca	34.05	0.09
	Y	31.51	0
Prism	None	102.14	0
$(10\bar{1}0)$	Al	100.48	-8.93
	Zn	100.71	-8.37
	Ca	109.12	15.42
	Y	100.57	1.80
Pyramidal	None	124.11	0
$(\bar{1}01\bar{1})$	Al	120.39	0.57
	Zn	120.65	-1.85
	Ca	127.16	11.31
	Y	122.63	-6.05

The electrochemical dissolution rate (I) of metallic materials is often estimated by the Tafel-type expression as given by Eq. 4.3.3 [86, 198].

$$I = k \exp\left(\frac{Q}{RT}\right) = k \exp\left(\frac{\beta\gamma}{RT}\right) \tag{4.8}$$

where I is the dissolution rate, k is the reaction constant, Q is the activation energy to remove a metallic ion from the lattice and to dissolve it in the solution, R is the gas constant, T is the prescribed absolute temperature, β is the proportionality coefficient when the surface energy, γ, is used as the activation energy for dissolution. Assuming that the reaction constant k is same for the Mg systems with different surface planes in contact with corrosive media, it is feasible to evaluate the ratios of degradation rates for two different surfaces using

$$\frac{I_{\text{Mg alloy}}}{I_{\text{ref}}} = \exp\left(\frac{\beta\left(\gamma_{\text{Mg alloy}} - \gamma_{\text{ref}}\right)}{RT}\right) \tag{4.9}$$

that can in principle provide an estimation of the effect of an arbitrary $(hkil)$ plane of Mg/Mg alloy on the dissolution rate with reference to the rate from the basal plane of pure Mg. Here, $I_{Mg\ alloy}$, I_{ref}, $\gamma_{Mg\ alloy}$, and γ_{ref} are the dissolution rate of Mg alloy, the dissolution rate of reference (i.e., pure Mg with identical orientation as Mg alloy) system, the surface energy of Mg alloy, and the surface energy of reference system, respectively. These dissolution rate analyses have been previously implemented in many metallic systems to describe the corrosion behaviors [128, 130]. In the above expression, the proportionality coefficient,β, was set to 0.5 [85]. Note that this calculation is based on the assumption that the surface energy primarily determines the electrochemical dissolution rate ignoring the interaction between the aqueous environment and the metallic surface, and the proportionality coefficient, , is a constant irrespective of the surface plane orientations. Song et al. [86] used this approach to show that the dissolution rate of the prism plane is 20 times faster than that of the basal plane for pure Mg. Considering this calculation for the pure case, we estimated the effect of alloying elements as presented in Table 4. It is noticeable in Table 4.10 that the relative dissolution rate ratios of the alloyed surfaces are less than one except the Mg-Ca system. When the relative effects of surface orientations and surface alloying compositions on the corrosion rates are compared using the same Tefal-type approach, it was calculated that the crystallographic surface types have a more critical effect since the surface energies with different surface orientations are crucially different as summarized in 4.9. It should be emphasized that these calculations solely rely on the consideration of the influence of surface energy on the dissolution rates of surface using the Tefal-type expression. However, the surface energy is only one of the parameters influencing the dissolution behavior of the metal. For a more comprehensive understanding, other factors including oxide film formation, charge transfer, precipitation formation, etc. must be considered as well. Because of this, the estimation of the degradation of metals based on the surface energies is limited, and it often overestimates the overall degradation rates that are experimentally measured by hydrogen evolution or Nyquist-type dynamic polarization analyses. Earlier in this study we demonstrated that the adsorption energy of the water on Mg-based surfaces is influenced by the composition, and adding Ca or Y to the

Mg system would potentially increase the degradation rates. However, unlike the surface energy, when the dissolution rates are estimated solely by the surface energies, only Ca would promote the surface degradation.

Table 4.10: Estimated relative hydrolysis rate ratios using Tafel-type expression for the systems with various alloying elements and surface orientations.

	Surface planes		
Alloying elements	Basal (0001)	Prism $(10\bar{1}0)$	Pyramidal $(\bar{1}01\bar{1})$
None	1	1	1
Al	0.67	0.72	0.47
Zn	0.73	0.75	0.5
Ca	1.23	4.09	1.85
Y	0.74	0.73	0.74

4.3.4 Dissolution potential difference

Electrode potential difference could be an indicator of dissolution tendency that can be calculated from the difference in the rate of detachment of atoms. The trends of electrode potentials in different alloy systems can be highly correlated to their surface degradation behavior. Taking into consideration of the definition of free energy changes (i.e., chemical potential, $\mu = \left(\frac{\partial G}{\partial n}\right)_{T,P}$, where G, n, T, and P denote the free energy, the number of atoms in the system, and prescribed temperature and pressure, respectively) in a thermodynamic system, the chemical potential (μ) can be obtained by Refs. [199, 200, 131],

$$\mu \approx \frac{E_{slab} - E^{v}_{slab}}{\Delta n} \tag{4.10}$$

Where E^{v}_{slab}, E_{slab}, and Δn represent the total energies of Mg/Mg alloy slab with missing Mg atom (i.e., slab with vacancy) and the slab without missing Mg atom (i.e., perfect crystal), and the number difference of Mg atoms between these two systems, respectively. The relative electrode potential differences of Mg in an alloy (ΔU) with respect to the clean Mg can then be expressed by,

$$\Delta U = U_{alloy} - U_{pure} = \frac{\mu_{pure} - \mu_{alloy}}{2e} \tag{4.11}$$

In Equation (5)U_{alloy}, U_{pure}, μ_{alloy}, and μ_{pure} stand for the electrochemical potentials and free energy changes (i.e., chemical potentials) of alloyed and pure Mg materials, respectively. Note that the electrode potentials (U_{alloy} and U_{pure}) given in Eq. 4.3.4 take the form of including the anodic electrode reaction, i.e., $Mg = Mg^{2+} + 2e^{-}$, with the units of [V]. The sign of ΔU can dictate the extent of propensity for losing Mg atoms. It is interpreted that, when ΔU is negative, the Mg-based alloy system is more likely to lose an Mg atom compared with pure Mg materials, whereas positive implies that the Mg-based alloy system is less likely to lose an Mg atom with reference to pure Mg.

Figure 4.27 shows examples of vacancy formation energy ($E_{f,v}$) changes for (a) pure Mg and (b) Mg-Al systems with different dissolution sequence on the basal (0001) surface. A higher formation energy represents a lower tendency for formation of vacancy. The expression reported in Gao et al.s work [201] was used for calculating the vacancy formation energy of Mg surface.

$$E_{f,v} = \left(E^{N} - E^{N^0}\right) - \left(N_{Mg} - N^0_{Mg}\right)\epsilon_{Mg} \tag{4.12}$$

Where E^N and E^{N^0} are the total energies of the defective and perfect systems,N^0_{Mg} and N_{Mg} are the numbers of Mg atoms before and after vacancy formation, respectively, and ϵ_{Mg} is the energy per atom in pure Mg. It was calculated that $E_{f,v}$ of pure Mg surface is 0.49 eV, which is smaller than of pure bulk Mg lattice (0.86 eV) [13]. Such difference clearly presents that formation of vacancy on the surface is much easier compared with the bulk lattice of pure Mg metal. In the figure, as the dissolution process takes place (i.e., removal of surface atom), the vacancy formation energy level of a system is qualitatively indicated using a horizontal bar with the corresponding surface structural image. The purple sphere in Figure 4.27(b) represents Al atom. From Figure 4.27(a), it is seen that the energy state of the perfect surface (i.e., no vacancy, the far-left side image of Figure 4.27(a)) is the lowest because forming a vacancy site is thermodynamically unfavorable on the Mg surface; after dissolution of one Mg atom, the energy state and the stability of the system increases and decreases, respectively (middle image of Figure 4.27(a)). Removal of the second atom

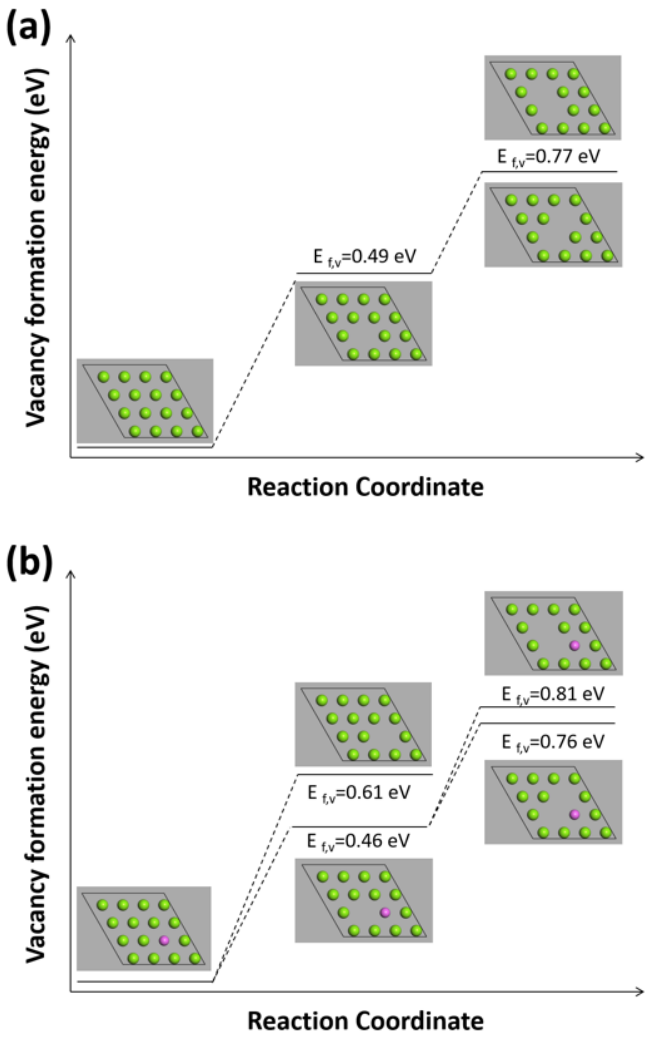

Figure 4.27: Vacancy formation energy changes for (a) pure Mg and (b) Mg-Al systems with different dissolution sequences on the basal surface.

increases the energy level to higher values (far-right side image of Figure 4.27(a)). A similar trend was found for the Mg surface alloyed with Al, as shown in Figure 4.27(b). To examine the impact of Al, the 1st nearest neighbor Mg from the Al site was removed first (middle image of Figure 4.27(b)). Next, one of the two candidate Mg atoms on the surface, the 1_{st} or 2_{nd} nearest neighbors from the Al site, were considered for dissolution of the 2_{nd} Mg atom (far-right image of Figure 4.27(b)). The results show that the energy state is slightly higher when the 2_{nd} nearest neighbor of the Al atom is dissolved compared with the dissolution of the 1st nearest neighbor of Al. In Figure 4.27 (b), we also show that the dissolution of Al impurity by forming a vacancy site at the Al position on the Mg surface. As seen in the results, it is less likely that the dissolution of Al

impurity would take place because $E_{f,v}$ (0.61 eV) for Al impurity is much higher than (0.46 eV) for nominal Mg atoms on the Mg-Al surface.

Table 4.11: Total energies and electrode potentials for the Mg alloy systems with different surface planes and alloying elements.

	Surface planes	Alloying element	$E_{slab,alloy}$ (eV)	$E^{v}_{slab,alloy}$ (eV)	U_{pure} (eV)	U_{alloy} (eV)
$1^{st}Mg$	Basal (0001)	Al	-349659.90	-344201.26	-5445.82	-5458.64
		Zn	-391490.01	-386029.89		-5460.12
		Ca	-361501.12	-356042.18		-5458.93
		Y	-433785.18	-428323.38		-5461.81
	Prism ($10\bar{1}0$)	Al	-349654.15	-344195.75	-5445.58	-5458.40
		Zn	-391484.26	-386024.36		-5459.90
		Ca	-361495.41	-356036.59		-5458.83
		Y	-433779.52	-428317.89		-5461.63
	Pyramidal ($\bar{1}01\bar{1}$)	Al	-349650.19	-344191.60	-5445.82	-5445.75
		Zn	-391480.30	-386020.25		-5460.08
		Ca	-361496.64	-356032.65		-5458.99
		Y	-433775.24	-428313.54		-5461.70
$2^{nd}Mg$ ($1^{st}NN$)	Basal (0001)	Al	-344213.91	-338755.64	-5445.61	-5458.28
		Zn	-386044.08	-380584.39		-5459.69
		Ca	-356055.27	-350596.61		-5458.66
		Y	-428339.12	-422877.61		-5461.51
$2^{nd}Mg$ ($2^{nd}NN$)	Basal (0001)	Al	-344213.91	-338755.59	-5445.61	-5458.32
		Zn	-386044.08	-380584.24		-5459.84
		Ca	-356055.27	-350596.55		-5458.72
		Y	-428339.12	-422877.70		-5461.42

We carried out similar DFT calculations for the rest of Mg surface orientations with different alloying elements. For the 2^{nd} Mg atom removal, we only considered the systems with the basal surface orientation. Table 4.11 provides the details of the calculated total energies and electrode potentials for the Mg alloy systems with different surface planes and alloying elements. Using this data,ΔU calculation results with reference to the pure Mg for different Mg alloys are presented in Figure 4.28. All of the solid symbols in the electrode potential difference plot in Figure 4.28 corresponds to the ΔU for the 1^{st} Mg atom dissolution. From this electrode potential difference point of view, it was predicted that addition of Al, Zn, and Ca will initially decrease the electrode potential difference with reference to the pure Mg and that the surface would show higher tendency to lose one of the Mg surface atoms. On the other hand, as Y has an electrochemical reduction

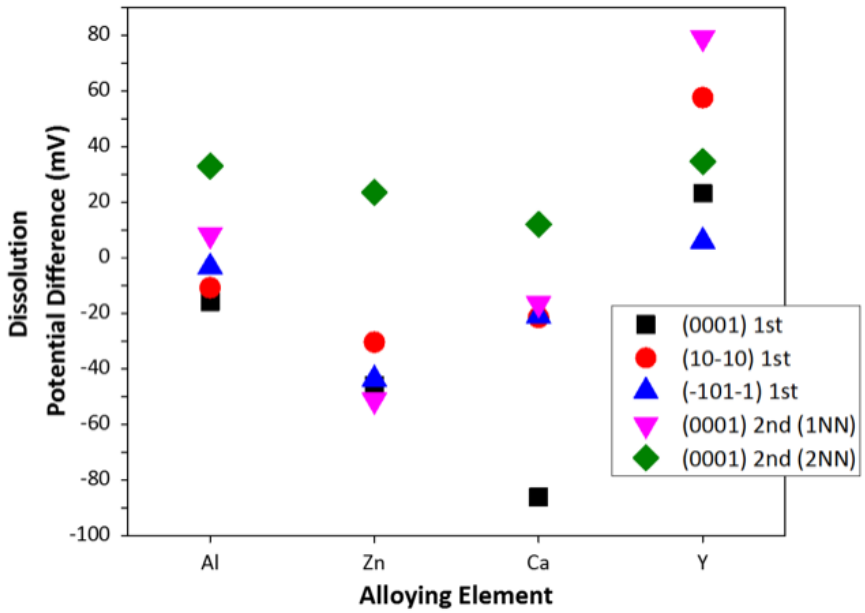

Figure 4.28: Relative electrode potential differences (shifts) with reference to the pure Mg system with various surface orientations.

potential value close to that of Mg, existence of Y on the surface reduces the dissolution tendency of the pure Mg; Y would improve the initial dissolution resistance of the Mg alloy as the electrode potential difference for all of the model systems including Y is positive. When the electrode potential shifts of the 2^{nd} dissolved Mg atoms are taken into consideration, these initial results from different alloyed systems are mitigated. The calculated results are shown in Figure 4.28 using the open and hatched symbols. Here, the open and hatched symbols represent the results of removing the 1^{st} and 2^{nd} nearest-neighbors from the alloy element site, respectively. It was generally found that the electrode potential difference for the removal of the 1^{st} nearest-neighbor Mg atom (i.e., solid symbols in Figure 4.28) follows a similar trend to of the first Mg atom, but they show a higher potential difference values. This difference is slightly positive for the Mg-Al system, which will render the dissolution more difficult compared to dissolution of the 1^{st} Mg atom. In the Zn and Ca cases, on the other hand, the dissolution potential differences are still negative. The electrode potential shift is all positive and it reaches as high as 80 mV for the Mg-Y system, which indicates that presence of Y on the surface may contribute to a stronger interaction between the surface and sublayer atoms. The types of alloying elements affect the tendency of the surface to lose the 2^{nd} neighbor Mg atom (i.e., hatched symbols in Figure 4.28), and all of the calculated values are

positive with relatively narrow variations. Therefore, it is likely that, once the first Mg atom is removed from the surface, removing the second one becomes more challenging if it is not the 1^{st} nearest-neighbor of the impurity elements (Al, Zn, or Ca). However, for Mg-Y system, expulsion of the 1^{st} nearest-neighbor of the alloying site is the most difficult compared to the equivalent atom on the pure Mg surface.

It must be noted that the electrode potential shifts are influenced by the contents and segregation of alloying elements, therefore, the trend of the Mg dissolution in Mg alloy surfaces could be varied. Also, the actual degradation behavior of surface will be affected by the interaction between the surface and the media. Here, we considered the degradation of Mg surface ignoring the impacts of the degrading media. However, it is likely that addition of Y in the Mg alloys would not generate the negative shift in the electrode potential difference from the general surface stability aspect, thus, as long as any deleterious intermetallic phases such as Mg_24Y_5 are formed, the corrosion resistance of Mg-Y alloy would not be decreased. These results are consistent with previous experimental observations [100]. On the other hand, although the tendency is decreased as the dissolution of Mg proceeds, including other elements (Al, Zn, and Ca) even without formation of intermetallic phases can shift the anodic electrode potential to a lower value, which would polarize the electrode potentials more, thereby promoting the dissolution of Mg from the alloyed surface. For Mg-Al alloy case, therefore, the improvement in corrosion resistance is majorly resulted from the formation of β-phase as a degradation barrier, not from the solid solution effect on the surface. It has been reported that adding Ca affects the solubility chemistries that reduces the fraction of other intermetallic compounds in Mg alloys, which will retard the corrosion from micro-galvanic mechanism [98]. Formation of Mg_2Ca compounds is also known to increase the corrosion resistance of Mg-Ca alloys. However, from an atomistic perspective, it is predicted that presence of Ca on the Mg surface would increase the degree of interaction with a water molecule and decrease the electrode potential. Finally, it is mentionable that, the application of current model is limited because the adsorption energies have been described based on a water molecule rather than water frameworks comprised of multiple water molecules. Also, the current model does not consider the probable oxidized states of the Mg surfaces. However, although the analyses presented here focuses on the dissolution-type surface degradation mechanism without consideration of the formation of various hydroxide layers, it is thought that they can provide important insights for the dissolution behaviors

of Mg-based alloy systems from the atomistic surface degradation point of view understanding the solid solution effects.

4.4 Selective laser melting

Distribution of particles in metal matrix composites has a crucial effect on the efficiency of the mechanical reinforcing process. Re-melting and solidification of the matrix due to laser energy input during selective laser melting increases the probability of the secondary phase agglomeration. Reinforcement particles reallocate locally based on the velocity of the solidification front moving forward through formation of the melt pool. Adequate energy input and especially optimized scanning speed is required, not only to assure consolidation of the product, but also to control the melt pool geometry and solidification rate and consequently avoid particle pushing and clustering. A finite volume model is developed to exhibit the interaction of aluminum nitride particles with the AlSi10Mg melt pool with respect to the solidification front. The model shows that the critical solidification conditions define whether particle engulfing or particle pushing take place; as an essential consideration when manufacturing metal matrix composites through selective laser melting.

Melting and re-solidification of the powder via moving laser heat source may push the reinforcement particles causing uneven distribution and decreasing the reinforcement efficiency. This study analyzes the behavior of melt pool in the AlSi10Mg/AlN composite to provide comprehensive understanding of the particle matrix interaction during the SLM process of the composite.

Geometry of melt pool and the shape of proceeding fluid are the starting points to check the quality of the SLM process. For this purpose the top view of all the 9 studied cases are compared in Figure 4.29. The melt pool in all the SLM processes is expected to be an elongated oval shape with wider tip and sharper tail. The shape of the melt pool and the heat effected area around it are clearly influenced by the input energy parameters. It is observed that a sharper end is more common when the scanning speed is high and as the speed decreases the tail is smoother and less sharp. As it was mentioned earlier the laser input energy density has direct dependency on the power and reverse relationship with the laser scan velocity. Since the scanning hatch distance and the powder thickness are constant during the SLM process in this study the case with 200 W power and velocity equal to 100 mm/s has the highest energy input density followed by 150 W power and

100 mm/s velocity and then 200 W power and 150 mm/s laser scanning velocity. Comparing the shape of melt pool highlights that the melt pool and the heat effected zone are larger when the density of the input energy is higher. Also it is noticed that the shape of the heat effected zone and the melt pool are less elongated and closer to circular shape when the energy input density is higher and as it decreases, the heat effected zone area and the melt pool shrink and become narrower.

To obtain a sound final product it is essential to assure continuity in the structure and therefore overlapping between sequential layers and tracks during laser scanning. Optimizing the depth of the melt pool results in the connection between previously processed layers and newly formed layers. Also the hatch distance can be adjusted to minimize the used energy and guarantee connection between tracks by varying the width of the melt pool. A longer melt pool tail corresponds to relatively slower solidification speed which affects the microstructure and mechanical properties of the final product. Figure 4.30 compares the dimensions of the melt pool in different laser scanning conditions. Results show that the length of the melt pool is directly influenced by the laser power. For a constant scanning speed as the laser power increases from 100 W to 150 W and then 200 W the length of the melt pool increases. However the effect of scanning speed for constant laser power is reverse and also causes less changes in length of the melt pool. An increase in the length of the melt pool due to increasing the laser power can be as high as 0.24mm, while increasing the scanning speed from 100 mm/s to 200 mm/s has its maximum effect when the laser power is higher and is about 0.10 mm. On the other hand the trend for depth and width of the melt pool can be explained more specifically by the energy input or the P/V ratio than the individual parameters. When the P/V ratio for input energy density is higher than one the melt pool width reaches its maximum which is equal to 0.15 mm and the width decreases to 0.1 mm, if the P/V value is equal or lower than one. The same pattern is observed for the melt pool depth and the depth of the formed melt pool is deepest and equal to 0.075 mm and when the ratio is equal to or below one the melt pool penetrates to 0.05 mm deep in powder with one exception when the P/V ratio is reduced to 1/2 at the scanning speed of 200 mm/s and laser power equal to 100 W the depth of the melt pool is minimum and equal to 0.02 mm. Considering the geometry of the melt pool in order to have a sound final product it is necessary to design the processing procedure in a way that the thickness of the deposited powder is less than the minimum melt pool depth which is 0.02 mm or 20 μm and to assure that the laser is scanning the surface with hatching distance smaller than

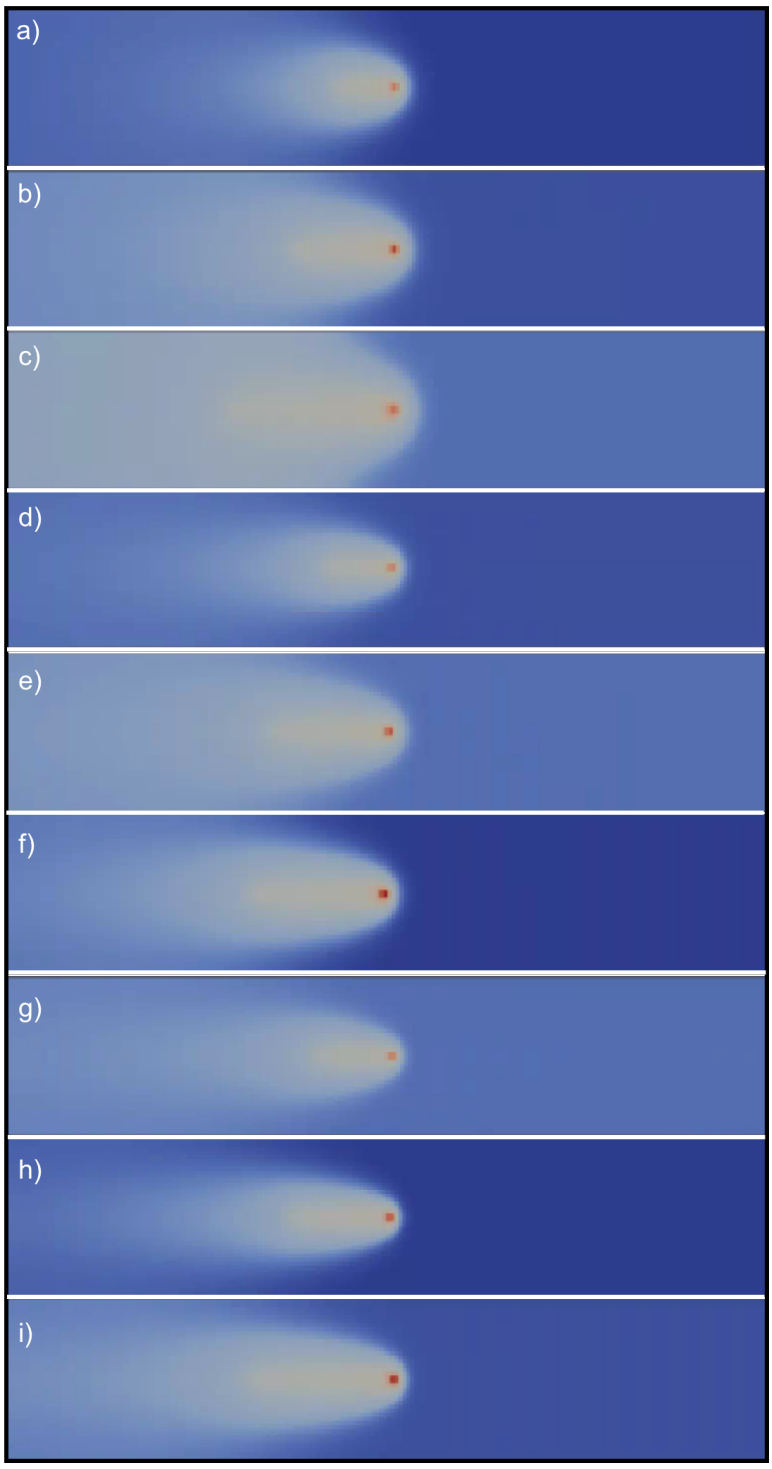

Figure 4.29: Top view of the temperature profile during laser scanning a)100 W power, 100mm/s speed and initial temeprature 298K , b)150 W power, 100 mm/s speed and initial temeprature 373K c)200 W power, 100 mm/s speed and initial temeprature 473K d) 100 W power, 150 mm/s speed and initial temeprature 373K e) 150 W power, 150 mm/s speed and initial temeprature 473K, f) 200 W power, 150 mm/s speed and initial temeprature 298K g)100 W power, 200 mm/s speed and initial temeprature 473K h) 150 W power, 200mm/s speed and initial temeprature 298K i) 200 W power, 200mm/s power and initial temeprature 373K.

0.1 mm or 100 μm or the minimum width of the melt pool. Preheating the surface prior to laser scanning does not show any specific effect on the geometry of the melt pool as far as the results of this work show. Laser input energy density with ratio of the power over scanning speed and also each of the laser power and speed individually seem to have more recognizable effect on the geometry of the melt pool than preheating up to 473K.

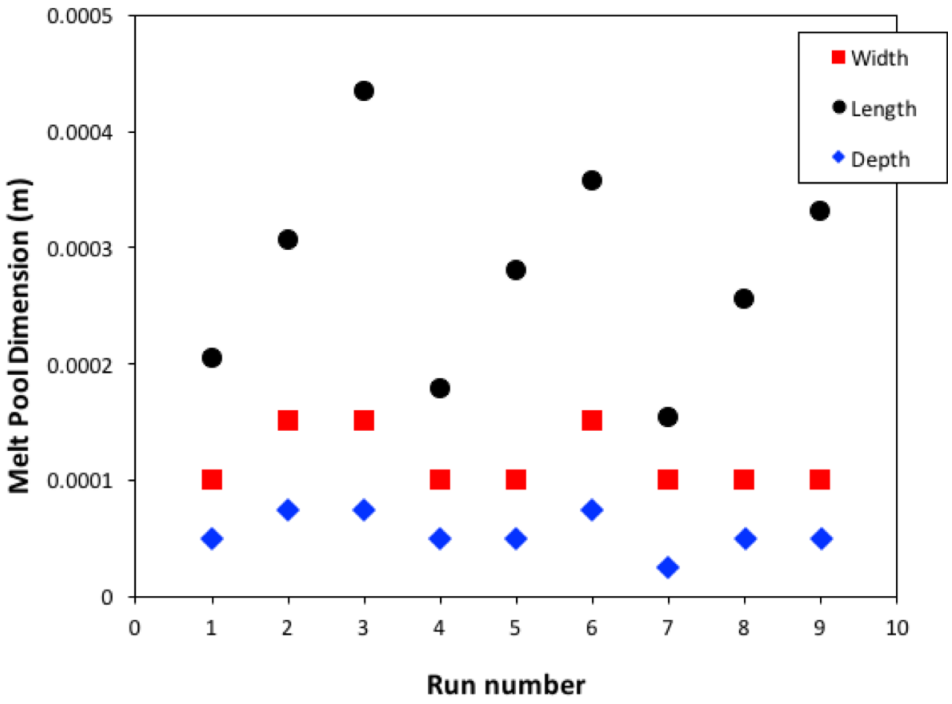

Figure 4.30: Dimensions of the melt pool during the SLM processing of AlSi10Mg/AlN composite.

As it was mentioned earlier, distribution and size of the reinforcement particles are significantly important to guarantee the efficiency of the metal matrix composites. When melting the powder for SLM process it must be checked that only the metal powder melts and the reinforcement particles, AlN in this case, do not change phase or interact with the matrix alloy or AlSi10Mg. To make sure that the temperature does not exceed the melting temperature of AlN, the maximum temperature reached under each condition is investigated. Figure 4.31 reports the maximum temperature in the SLM process in all the different studied conditions in this work. Knowing that the melting temperature of AlN is equal to 2473 K [202] and comparing the results in Figure 4.31 it can be confirmed that the AlN powder will melt in none of the tested conditions, as the highest temperature reached in all the simulations is 1710 K. Since the AlSi10Mg powder in all the cases passes its melting

temperature, it is granteed that the final product is continuous. The maximum temperature of the melt pool is also influnced by laser power and the scanning speed. As the laser power increases at a constant scanning speed the maximum temperature also increases as it is expected due to increase in the input energy density. However the preheating temperature overwrites the slower motion of the scan and the temperature is higher in the cases that have been preheated to 473 K.

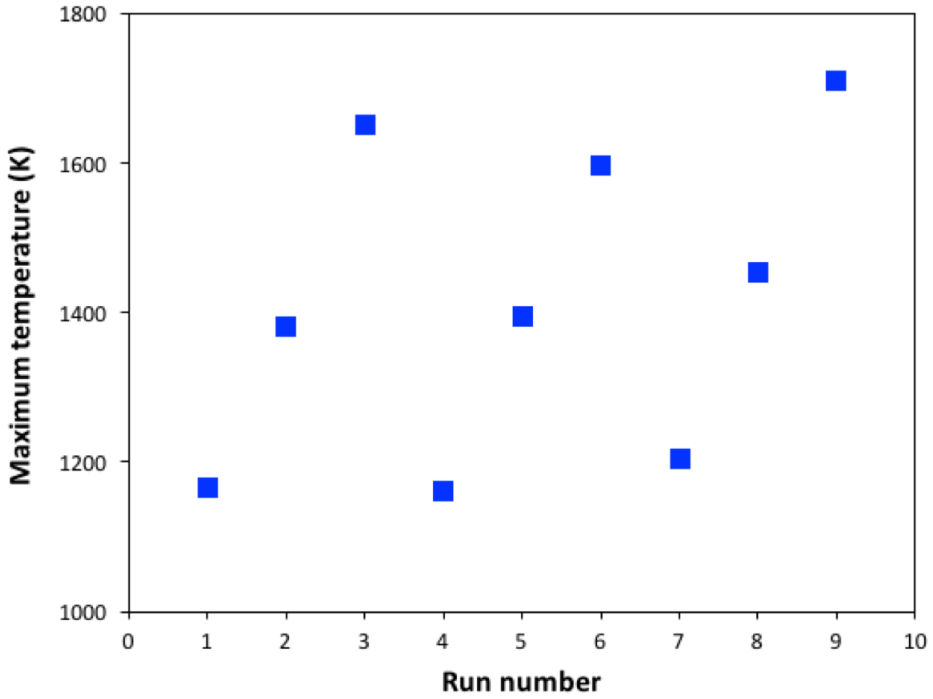

Figure 4.31: Maximum temperature of the part during the scanning process.

Figure 4.32 shows the temperature profile along the scanning path for a frame captured after 15 ms of scanning. All the 9 profiles have a step at the melting range of the AlSi10Mg alloy. This range is between 830 K to 867 K where the mushy zone is formed. The length of this step varies in different cases and it seems to have direct relationship with the input energy density. In other words by increasing the laser power at a constant scanning speed length of the region which is under transition expands. It should be noticed that this length is the region that contains a mixture of solid and liquid and should be differentiated from the melt pool which is fully liquid phase containing only reinforcement particles as the solid phase. The peak in this plot indicates the position of the laser tip where the laser beam is focused and results in the highest temeprature. Preheating the powder prior to the SLM process increases the length of the mushy zone as the

results show.

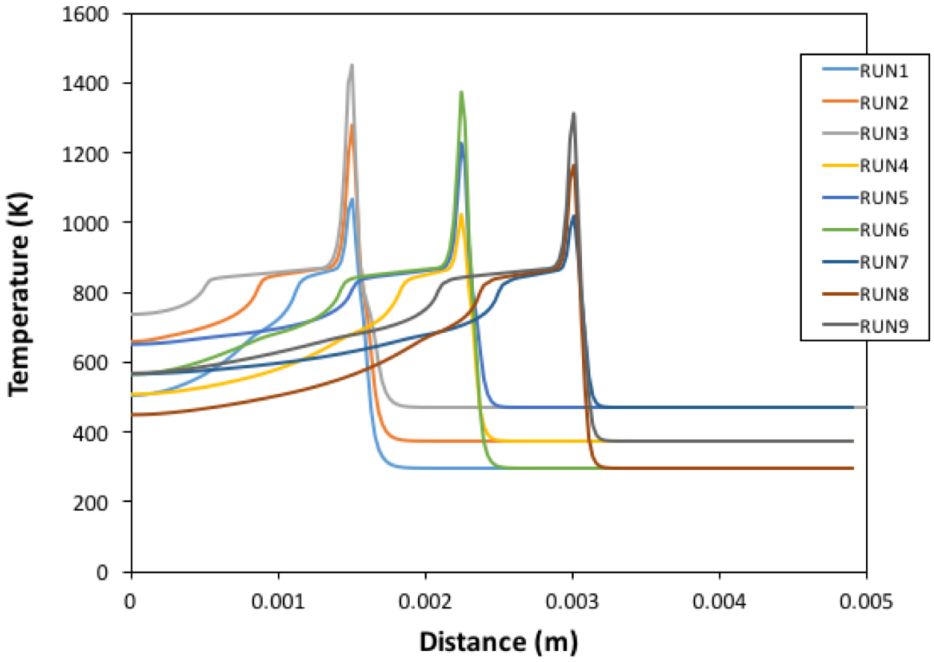

Figure 4.32: Temperature profile on the top surface along the scanning path after 15 ms of scanning.

As the scanning heat source moves along the length of the surface it is essential to track and observe the temperature and phase changes occurring in the system. To fulfill this purpose, the center point on the top surface of X-Y plane with coordinates, x=0.5 mm, y=2.5 mm and z=0.7 mm, is chosen as the representative of the points on the surface that experience the heat absorption from the source. This point is selected on the top most surface because it is believed that the highest concentration of energy from the heat source is placed on this plane and it provides an understanding of an extreme situation in the system. Figure 4.33 shows the temperature variation with time at the center of the top most layer on X-Y plane during the SLM of AlSi10Mg/AlN powder. Initially the temperature of center point is constant and equal to the preheating temperature. The moment that the laser beam passes over the center point a sharp peak is observed, and as the laser passes, the mushy zone forms behind the melt pool. The mushy zone will be stable for a period of time after the beam leaves the center point. The stability of the mushy zone depends strongly to the energy input density and is independent of the preheating temperature. The solid/liquid region is stable for the longest period of time when the P/V ratio is equal to 2 and it decreases as the ratio

decreases.

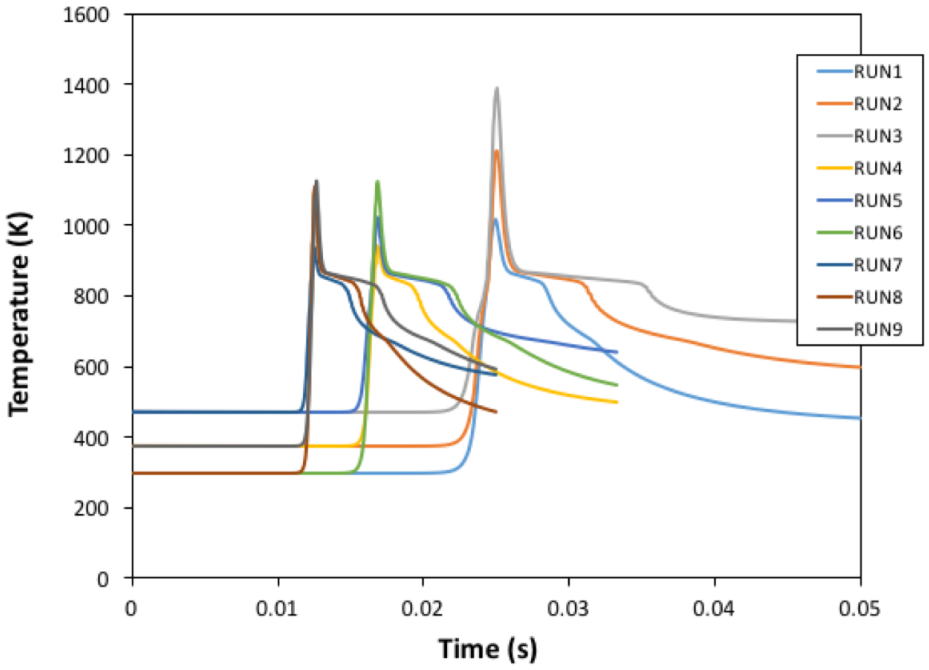

Figure 4.33: Temperature profile during the scanning period at the center point of the powder surface x=0.5 mm, y=2.5 mm and z=0.7 mm.

4.4.1 Particle Pushing

Melting and re-solidification of the composite increases the risk for agglomeration and segregation of the reinforcement particles. The theory suggests that as the melt pool advances the reinforcement particles in the melt are pushed forward, if the solidification front moves in a slow rate. A critical value has been suggested by previous scientist for velocity of the solid/liquid interface below which the particle will be pushed. At advancing rates higher than this critical value the particle will be trapped and encaptured by the solidifying front. Table 4.12 summarizes the most popular analytical models for prediction of the critical velocity of the solid/liquid interface.

Considering an ideal spherical geometry for the AlN reinforcement particle and a planar interface between solid and liquid, Figure 4.34 schematically presents the interaction between the solidification front and the particle based on the model suggested by Rohatgi and Kim [207]. The solidification front advances with a velocity equal to V and the thermal gradient in solid/liquid interface far from the particle is denoted as G. Their analytical model suggests that, if the solidifi-

Table 4.12: Predictive equations for calculated critical velocity of solidification front based on previous studies

Model	Formula		Reference
Uhlmann	$V_{cr} = \frac{(n+1)}{2}\left(\frac{La_0V_0D_1}{KTR^2}\right)$		[203]
Chernov	$V_{cr} = \frac{0.14B_3}{\eta R}\left(\frac{\sigma_{sl}}{B_3}R\right)^{(1/3)}$	$\frac{\lambda^2}{l} > R$	[204]
	$V_{cr} = \frac{0.15B_3}{\eta Rl}$	$\lambda^2 < R$	[204]
Shangguan	$V_{cr} = \frac{\Delta\sigma a_0}{3(n-1)\eta\alpha R}\left(\frac{n-1}{n}\right)^n$		[205]
Stefanescu	$V_{cr} = \frac{a_0\Delta\sigma}{6\eta R(n-1)}\left(2 - \frac{K_p}{K_l}\right)$		[206]
Kim & Rohatgi	$V_c = \frac{\Delta\sigma a_0(kR_1+1)}{18\eta R_1}$		[207]
Kaptay	$V_cr = \frac{0.157}{\eta}\Delta\sigma_{cls}^{2/3}\sigma_{SL}(\frac{a}{R})^{4/3}$		[208]
Mao	$V_{cr}\frac{\frac{2}{9\eta}a^2(\rho_p-\rho)g}{\frac{\lambda G}{2\Delta T'}[1-tan(\theta/2)]\left(\frac{1+ftan\theta}{tan\theta-f}+tan\theta\right)-1}$		[209]
Tao	$\frac{\rho_s L\lambda^{9/4}G^{1/4}}{6\eta T_{mp}^{1/4}R}$		[210]

cation front moves at velocities higher than the critical value of V_{cr} the particle will be encaptured, otherwise pushed and agglomeration of reinforcement particles is expected due to the particle pushing effect.

$$V_{cr} = \frac{\Delta\sigma a_0(kR_1+1)}{18\eta R_1} \tag{4.13}$$

Here $\Delta\sigma$ is the interfacial energy difference, a_0 is particle/interface separation behind the particle, k, R_1 and η are the curvature of solid/liquid interface behind the particle, particle radius and liquid viscosity respectively. The curvature is defined as:

$$k = \frac{Ga}{\Gamma}(\frac{\alpha-1}{3}) \tag{4.14}$$

α is the ratio of thermal conductivity of particle to liquid metal and is estimated from averaging the thermal conductivities in plots in Figure 3.3 over the processing temperature range. As ex-

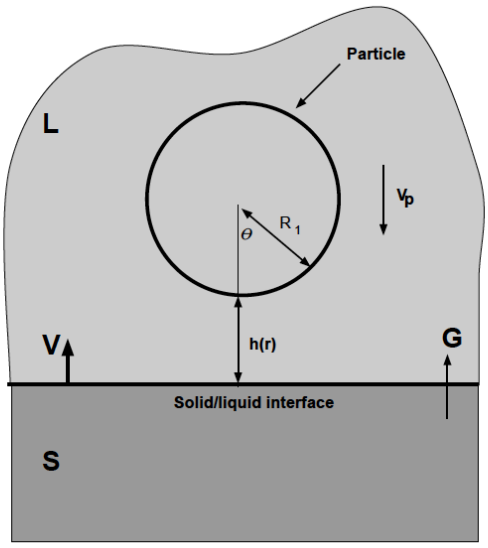

Figure 4.34: Schematic of particle interacting with solidification front

pressed below Γ depends on the solid/liquid surface tension σ_{SL}, melting temperature T_m, density ρ and heat of fusion H. Table 4.13 reports numerical values of the parameters used in the model.

Table 4.13: Materials properties and theoretical parameters for particle pushing process

Parameter	Value	Reference
Particle radius, R_1,	10×10^{-6} m	
Particle/interface separation behind particle, a_0	3 $m \times 10^{-10}$ m	
Surface energy of the interface, σ_{SL},	0.09 N/m	[145]
Interfacial energy differences, $\Delta\sigma$,	4.56 N/m	[211]
Viscosity, η	1.3×10^{-3} $Pa.s$	[145]
Temperature gradient, G,	3.8×10^3 K/m ,	[143]

$$\alpha = \frac{K_p}{K_l} \tag{4.15}$$

$$\Gamma = \frac{\sigma_{SL} T_m}{\rho H} \tag{4.16}$$

Comparing the solidification front velocity from the FVM model presented in table 4.14 with the analytical calculations based on previous models (5900 μm), reveals that the velocity of the solidification interface is much higher than the calculated critical value, suggesting that the particles present in the melt pool will be engulfed by the solidifying front. Homogenous distribution

Table 4.14: Taguchi design of experiment. L9 orthogonal array.

Run No.	Speed (mm/s)	Laser power (W)	Powder bed temperature (K)	S/L interface velocity (mm/s)
1	100	100	298	97
2	100	150	373	97
3	100	200	473	97
4	150	100	373	148
5	150	150	473	148
6	150	200	298	148
7	200	100	473	196
8	200	150	298	196
9	200	200	373	196

of the AlN particles in the AlSi10Mg is expected and the SEM image of the microstructure of AlSi10Mg/AlN composite produced through SLM process with energy input density with P/V ratio less than one illustrated in Figure 4.35 confirms that the reinforcement particles will not be pushed by the advancing solidification front. In Figure 4.35 the particles have an average size of 0.45 μm and homogeneous distribution of particles in the AlSi10Mg matrix is demonstrated with white arrows. As the theoretical model suggests the critical velocity is a function of particle size. Further calculations for the critical particle size shows that reinforcement particles smaller than 0.29 μm will be pushed by the solidification front and agglomerate. Also, estimations show that the velocity of solidification front requires to be about 50m/s to engulf the particle with 1 nm size, emphasizing that the size of reinforcement particles is a crucial parameter for a homogeneous microstructure in the final product.

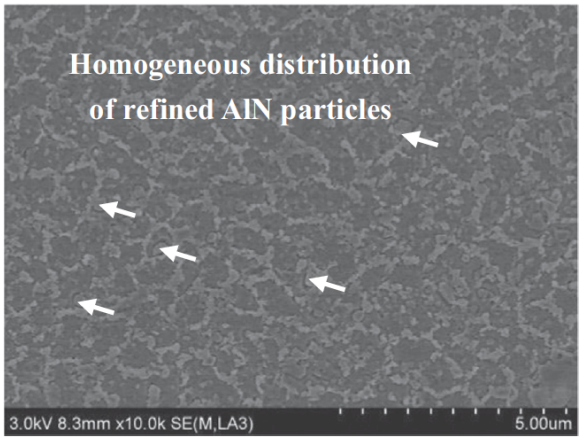

Figure 4.35: SEM image showing typical distribution of the AlN particles in AlSi10Mg matrix where P=180 W and V=400mm/s [14]

4.4.2 S/N Analysis

Table 4.15 illustrates the S/N results of the 9 modeled conditions after measuring the geometry of melt pool. According to range analysis from S/N, the influence of each factor on the geometry of the melt pool is Laser power>Scanning speed>initial temperature.

Figure 4.36 shows the change curve of the orthogonal experiment average value, and the change trend geometry with various factors and S/N. With increasing the laser power the size of melt pool increases in all directions while the effect of laser speed is reverse as the slope of the plot is negative and the initial temperature does not demonstrate any effect on the melt pool geometry as the main effect line is almost horizontal. Also to confirm this statement the analysis of the variables is summarized in table 4.15. Considering a confidence level with $\alpha = 0.01$ the $F_{(2,6)} = 10.93$ meaning that, the F value from a factor needs to be higher than this value for the factor to be significant. Results show that the laser scanning speed and laser power show significance while the initial temperature has insignificant effect which explains the horizontal angle of main effect plot.

Table 4.15: Analysis of the variance for geometry of the melt pool

Factor	Sum of squares	Degree of freedom	Mean square	F value	
Laser speed	26.11	2	13.05	13.43	significant
Laser power	28.05	2	14.02	14.43	significant
Initial temperature	5.83	2	2.91	3.00	insignificant
Error	1.94	2	0.97		
Total	61.93	8			

Figure 4.37 shows that based on Taguchi analysis the laser power and laser speed have significant effect on the maximum temperature of melt pool while the initial temperature does not show a significant effect on the melt pool maximum temperature. These factors have effect on the maximum temperature of the melt pool with the order Laser power>Scanning speed>initial temperature. Figure 4.38 demonstrate that the laser power and preheating are not main factors when it comes to the velocity of the solidification front and the laser moving speed is the only main effect. This statement is aligned with the previous experiments analyzing the solidification fo SLM process [142].

Figure 4.36: Main effect plot for the geometry of melt pool during the SLM process

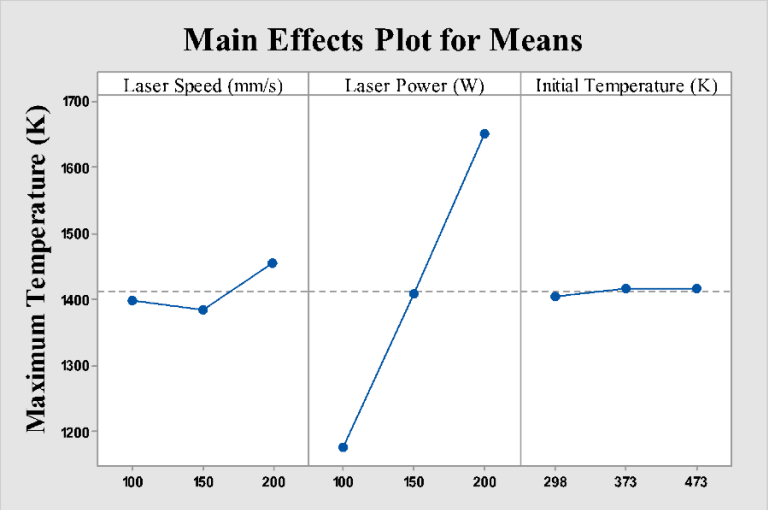

Figure 4.37: Main effect plot for the maximum temperature of melt pool during the SLM process

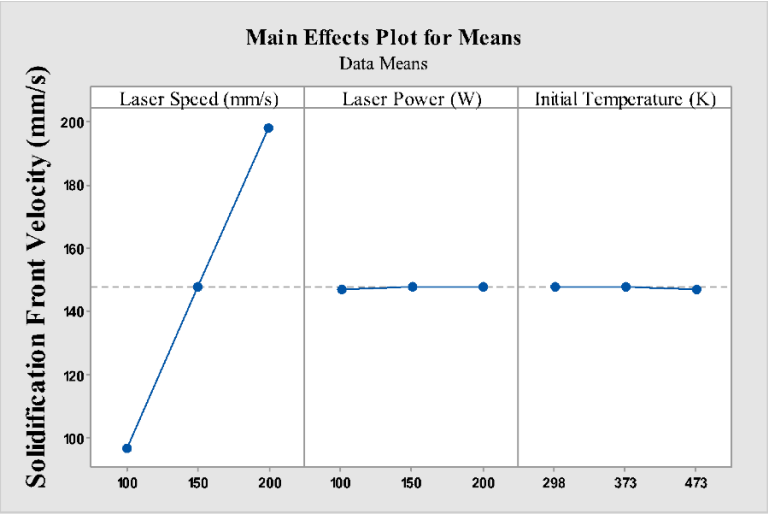

Figure 4.38: Main effect plot for the velocity of solidification front considering the effect of laser speed, laser power and initial temperature

Chapter 5

Summary and conclusion

The computational and analytical results in this work are organized in two major parts. In the first part focusing on the preparation of the initial powder for manufacturing products made of Al and Mg based metal matrix composites and nano composites a closer look is taken to the interaction of metal powder with the highly abundant molecules in the process. Cryomilling is selected as the powder preparation technique and interactions of N and N_2 as the most abundant species in the processing media are analyzed with the base metals. Then, as one of the most important concerns, corrosion behavior of Mg matrix is inspected through observing the interaction of water molecule with the Mg metal surface. In the second part of the study shaping the powder into a sound final product is the main objective. In this part a finite volume model analyzes the AlSi10Mg/AlN composite while being processed via selective laser melting. The major findings obtained in this work are summarized as following.

- The DFT calculation revealed that addition of 0.0625 alloying element to the Mg surface does not significantly change the surface energies.
- The structural configurations of pure Mg and Mg-Al systems containing an N atom or an N_2 molecule show high thermodynamic stability.
- The binding strength of N_2 molecule over different crystallographic surface planes ($basal < prism < pyramidal$) exhibits a positive relation to the value of surface energies of the corresponding planes.

- Incorporation of an Al impurity in the Mg matrix will reduce the diffusion energy barriers of N atoms and N_2 molecules by furnishing more spaces in the diffusion pathway.
- If dissociated N atoms are available near the surface/grain boundary area, they can easily form the N-rich dispersoids underneath the Mg surface.
- A 100 nm dispersoid was found in cryomilled Mg powders, EELS confirmed the dispersoid is a nitride, and EDS determined the nitrides identity to be Mg_3N_2.
- If dissociated N atoms are activated for further diffusion into the inner bulk lattice without forming the nucleus of N-rich dispersoids, the diffusion would be achieved by the interstitial mechanism through the tetrahedral sites with diffusion energy barriers of ~ 0.96 and ~ 0.42 eV for pure Mg and Mg-Al materials.
- For the pure Mg system, the substitutional diffusion mechanism of an N atom is probable, because the energy barrier is only ~ 0.58 eV, and as long as vacancy sites are readily available near the travelling N atoms.
- Because the strain energy estimation during milling process shows a wide range of variations, it is currently uncertain that such high energy in the form of introduced and/or stored strain energies (U_i and/or U_s) could be provided during conventional, low energy cryomilling.
- If the molecular N_2 species are pushed into the Mg lattice during milling, it is likely that the bulk diffusion would occur by the interstitial octahedral mechanism with energy barriers of ~ 2.10 and ~ 0.40 eV for pure and Mg-Al materials, respectively. However, it is again dubious that this energy level could be delivered during these conventional milling processes to avoid a high concentration of N-rich precipitates near the powder surface/ grain boundary.
- the adsorption of liquid N_2 is thermodynamically favorable onto the surface of Al powders with E_{ads} values of in the range of -0.134 to -0.142 eV/molecule.
- The tendency for N_2 adsorption can be strongly increased by adding transition metallic elements such as Mn or Fe.
- The dissociation of N_2 molecule over the Al surface will necessitate overcoming at least 1.93 eV/molecule when it is absorbed into the octahedral sites under the Al surface. Such

dissociation energy may be provided in the form of mechanical energy during the cryomilling process.

- After absorption of N/N_2, it was predicted that the diffusion energy barriers between the adjacent octahedral sites in pure Al for N and N_2 are 0.71 eV and 1.25 eV, respectively, and that presence of impurity elements (Mg, Mn, and Fe) will increase and decrease the diffusion energy barriers for the N and N_2 transport in the Al bulk lattice, respectively.

- The binding of a water molecule over atop position shows the highest strength on the basal (0001) Mg surface. The adsorption energy difference between the atop and other sites was calculated as ~ 0.14 eV for upright configuration and ~ 0.25 eV for tilted configuration.

- The basal (0001) plane exhibits a much lower propensity to attract a water molecule compared with other high-symmetric surface planes for a fixed composition, which is in consistent with the experimental observations for increased degradation resistance in the Mg systems with a (0001) surface orientation. On average, the adsorption energy of basal surface was ~ 0.3 eV lower than those of prism and pyramidal surfaces.

- Al increases the adsorption energy of a water molecule on the surface and slightly decreases the electrode potential difference with respect to the clean Mg surface. Therefore, adding Al on a Mg surface will reduce the degree of interaction between water molecules and the Mg surface, but it will slightly increase the dissolution tendency of Mg atoms from the surface. From this, it is inferred that the formation of a corrosion resistant β-phase would be primarily responsible for the enhanced corrosion properties of Mg-Al.

- Zn increases the adsorption energy of a water molecule on the surface and decreases the electrode potential difference with respect to the clean Mg surface. Adding Zn on a Mg surface could be beneficial as it will reduce the degree of interaction between water molecules and the surface, but it will increase the dissolution tendency of Mg atom from the surface. These results are in agreement with the previous knowledge that incorporating Zn could worsen the corrosion resistance of Mg alloys.

- Ca decreases the adsorption energy of a water molecule on the surface and decreases the electrode potential difference with respect to the clean Mg surface. Adding Ca imposes

negative effects on both the water adsorption and the electrochemical surface degradation. Corrosion improvement in Mg-Ca alloys could be, thus, attributed to the changes in the chemistries in the Mg alloys due to the existence of Ca, which may reduce the degree of the formation of other highly corrosive intermetallic compounds.

- Y decreases the adsorption energy of a water molecule on the surface and increases the electrode potential difference with respect to the clean Mg surface. Therefore, adding Y on Mg surface will enhance the degree of interaction between water molecules and the surface, but it will decrease the dissolution tendency of Mg atoms from the surface. With this, it is predicted that Y on the surface of Mg generally would not harm the corrosion properties, which is again in line with the experimental finding that Mg-Y alloy typically exhibit an improved corrosion resistance by forming well-defined passivation layers.

- During the SLM process a tear shape melt pool with wider tip and narrower tail forms as the result of particle melting. The shape and geometry of this melt pool changes depending on the laser input energy.

- A longer melt pool tail corresponds to a relatively slower solidification rate which is the result of slower laser source motion and higher laser power.

- The maximum temperature in the melt pool caused by highest laser power equals 1710K and is still very lower than the melting temperature of AlN suggesting that the reinforcement particles will not melt during the SLM Process

- The model shows that the solidification front advances with a velocity 17 to 34 times faster than the critical rate, which means that particles will encaptured by the solid/liquid interface resulting in a homogeneous distribution on the AlN particles in the matrix. This result is in agreement with the experimental results showing and even distribution of AlN particles in AlSi10Mg matrix processed with SLM technique.

- Taguchi analysis for the main factor effect shows that the laser power and speed have main effects on the geometry of melt pool while the initial temperature does not show a significant effect.

- For the maximum temperature of the melt pool only the laser power has a main effect and for velocity of the solidification front the laser velocity seems to be the only factor that has a main effect on the results.

Bibliography

[1] J-P Kruth, G Levy, F Klocke, and THC Childs. Consolidation phenomena in laser and powder-bed based layered manufacturing. *CIRP annals*, 56(2):730–759, 2007.

[2] Yali Li and Dongdong Gu. Parametric analysis of thermal behavior during selective laser melting additive manufacturing of aluminum alloy powder. *Materials & Design*, 63:856–867, 2014.

[3] Donghua Dai and Dongdong Gu. Thermal behavior and densification mechanism during selective laser melting of copper matrix composites: simulation and experiments. *Materials & Design*, 55:482–491, 2014.

[4] Wentao Yan, Wenjun Ge, Ya Qian, Stephen Lin, Bin Zhou, Wing Kam Liu, Feng Lin, and Gregory J Wagner. Multi-physics modeling of single/multiple-track defect mechanisms in electron beam selective melting. *Acta Materialia*, 134:324–333, 2017.

[5] M Tavoosi, F Karimzadeh, and MH Enayati. Fabrication of al–zn/α-al2o3 nanocomposite by mechanical alloying. *Materials Letters*, 62(2):282–285, 2008.

[6] N Al-Aqeeli, G Mendoza-Suarez, C Suryanarayana, and RAL Drew. Development of new al-based nanocomposites by mechanical alloying. *Materials Science and Engineering: A*, 480 (1-2):392–396, 2008.

[7] N Al-Aqeeli, G Mendoza-Suarez, A Labrie, and RAL Drew. Phase evolution of mg–al–zr nanophase alloys prepared by mechanical alloying. *Journal of alloys and compounds*, 400 (1-2):96–99, 2005.

[8] Khinlay Maung, James C Earthman, and Farghalli A Mohamed. Inverse hall–petch behavior in diamantane stabilized bulk nanocrystalline aluminum. *Acta Materialia*, 60(16):5850–5857, 2012.

[9] BO Han, EJ Lavernia, Z Lee, S Nutt, and D Witkin. Deformation behavior of bimodal nanostructured 5083 al alloys. *Metallurgical and Materials Transactions A*, 36(4):957–965, 2005.

[10] Lei Lu, Yongfeng Shen, Xianhua Chen, Lihua Qian, and Ke Lu. Ultrahigh strength and high electrical conductivity in copper. *Science*, 304(5669):422–426, 2004.

[11] Donghua Dai and Dongdong Gu. Tailoring surface quality through mass and momentum transfer modeling using a volume of fluid method in selective laser melting of tic/alsi10mg powder. *International Journal of Machine Tools and Manufacture*, 88:95–107, 2015.

[12] SN Ivanov, PA Popov, GV Egorov, AA Sidorov, BI Kornev, LM Zhukova, and VP Ryabov. Thermophysical properties of aluminum nitride ceramic. *Physics of the Solid State*, 39(1): 81–83, 1997.

[13] Marjan Nezafati, Anit Giri, Clara Hofmeister, Kyu Cho, Matthew M Schneider, Le Zhou, Yongho Sohn, and Chang-Soo Kim. Atomistic study on the interaction of nitrogen and mg lattice and the nitride formation in nanocrystalline mg alloys synthesized using cryomilling process. *Acta Materialia*, 115:295–307, 2016.

[14] Donghua Dai and Dongdong Gu. Influence of thermodynamics within molten pool on migration and distribution state of reinforcement during selective laser melting of aln/alsi10mg composites. *International Journal of Machine Tools and Manufacture*, 100:14–24, 2016.

[15] Yinmin Wang, Mingwei Chen, Fenghua Zhou, and En Ma. High tensile ductility in a nanostructured metal. *Nature*, 419(6910):912, 2002.

[16] Namita Rajput. Methods of preparation of nanoparticles-a review. *International Journal of Advances in Engineering & Technology*, 7(6):1806, 2015.

[17] Herbert Gleiter. Nanocrystalline materials. In *Advanced Structural and Functional Materials*, pages 1–37. Springer, 1991.

[18] Carl C Koch, Ilya A Ovid'Ko, Sudipta Seal, and Stan Veprek. *Structural nanocrystalline materials: fundamentals and applications*. Cambridge University Press, 2007.

[19] Marc A Meyers, A Mishra, and David J Benson. Mechanical properties of nanocrystalline materials. *Progress in materials science*, 51(4):427–556, 2006.

[20] CNR Rao. Chemical synthesis of solid inorganic materials. *Materials Science and Engineering: B*, 18(1):1–21, 1993.

[21] Maqsood Ahmad Malik, Mohammad Younus Wani, and Mohd Ali Hashim. Microemulsion method: a novel route to synthesize organic and inorganic nanomaterials: 1st nano update. *Arabian journal of Chemistry*, 5(4):397–417, 2012.

[22] Margarita Sanchez-Dominguez, Kelly Pemartin, and Magali Boutonnet. Preparation of inorganic nanoparticles in oil-in-water microemulsions: A soft and versatile approach. *Current Opinion in Colloid & Interface Science*, 17(5):297–305, 2012.

[23] DB Witkin and Enrique J Lavernia. Synthesis and mechanical behavior of nanostructured materials via cryomilling. *Progress in Materials Science*, 51(1):1–60, 2006.

[24] R Petkovic-Luton and J Vallone. Exxon research and engineering company. *Florham Park, NJ, United States of America US Patent*, (4619699), 1986.

[25] MJ Luton, CS Jayanth, MM Disko, S Matras, and J Vallone. Cryomilling of nano-phase dispersion strengthened aluminum. *MRS Online Proceedings Library Archive*, 132, 1988.

[26] Hanry Yang, Enrique J Lavernia, and Julie M Schoenung. Novel fabrication of bulk al with gradient grain size distributions via powder metallurgy. *Philosophical Magazine Letters*, 95 (3):177–186, 2015.

[27] Challapalli Suryanarayana. Mechanical alloying and milling. *Progress in materials science*, 46(1-2):1–184, 2001.

[28] Yaojun Lin, Bo Yao, Zhihui Zhang, Ying Li, Yongho Sohn, Julie M Schoenung, and Enrique J Lavernia. Strain energy during mechanical milling: Part i. mathematical modeling. *Metallurgical and Materials Transactions A*, 43(11):4247–4257, 2012.

[29] Randall M German. Sintering theory and practice. *Solar-Terrestrial Physics*, page 568, 1996.

[30] National council for advanced manufacturing nacfam, report on industry views towards: Categories of innovative and potentially disruptive advanced manufacturing technologies. 2005.

[31] Terry Wohlers. Us manufacturing competitiveness initiative dialogue. *Council on Competitiveness, Oak Ridge, TN*, 2013.

[32] HS Carslaw and JC Jaeger. *Conduction of heat in solids: Oxford Science Publications*. Oxford, England, 1959.

[33] Ahmed Hussein, Liang Hao, Chunze Yan, and Richard Everson. Finite element simulation of the temperature and stress fields in single layers built without-support in selective laser melting. *Materials & Design (1980-2015)*, 52:638–647, 2013.

[34] K Dai and L Shaw. Finite element analysis of the effect of volume shrinkage during laser densification. *Acta materialia*, 53(18):4743–4754, 2005.

[35] M Labudovic, D Hu, and R Kovacevic. A three dimensional model for direct laser metal powder deposition and rapid prototyping. *Journal of materials science*, 38(1):35–49, 2003.

[36] Ali Foroozmehr, Mohsen Badrossamay, Ehsan Foroozmehr, et al. Finite element simulation of selective laser melting process considering optical penetration depth of laser in powder bed. *Materials & Design*, 89:255–263, 2016.

[37] Yu-Che Wu, Cheng-Hung San, Chih-Hsiang Chang, Huey-Jiuan Lin, Raed Marwan, Shuhei Baba, and Weng-Sing Hwang. Numerical modeling of melt-pool behavior in selective laser melting with random powder distribution and experimental validation. *Journal of Materials Processing Technology*, 254:72–78, 2018.

[38] Chinnapat Panwisawas, Chunlei Qiu, Magnus J Anderson, Yogesh Sovani, Richard P Turner, Moataz M Attallah, Jeffery W Brooks, and Hector C Basoalto. Mesoscale modelling of selective laser melting: Thermal fluid dynamics and microstructural evolution. *Computational Materials Science*, 126:479–490, 2017.

[39] J Co JAEGER. Moving sources of heat and the temperature of sliding contacts. In *Proceedings of the royal society of New South Wales*, volume 76, pages 203–224, 1942.

[40] Li JunChang, C Langlade, and AB Vannes. Evaluation of the thermal field developed during pulsed laser treatments: semi analytical calculation. *Surface and Coatings Technology*, 115 (1):87–93, 1999.

[41] M Matsumoto, M Shiomi, Kozo Osakada, and Fumie Abe. Finite element analysis of single layer forming on metallic powder bed in rapid prototyping by selective laser processing. *International Journal of Machine Tools and Manufacture*, 42(1):61–67, 2002.

[42] Nikolay K Tolochko, Maxim K Arshinov, Andrey V Gusarov, Victor I Titov, Tahar Laoui, and Ludo Froyen. Mechanisms of selective laser sintering and heat transfer in ti powder. *Rapid prototyping journal*, 9(5):314–326, 2003.

[43] Gabriel Bugeda Miguel Cervera and Guillermo Lombera. Numerical prediction of temperature and density distributions in selective laser sintering processes. *Rapid Prototyping Journal*, 5 (1):21–26, 1999.

[44] Jia Yang and Fude Wang. 3d finite element temperature field modelling for direct laser fabrication. *The International Journal of Advanced Manufacturing Technology*, 43(11-12): 1060–1068, 2009.

[45] A Nisar, MJJ Schmidt, MA Sheikh, and L Li. Three-dimensional transient finite element analysis of the laser enamelling process and moving heat source and phase change considerations. *Proceedings of the Institution of Mechanical Engineers, Part B: Journal of Engineering Manufacture*, 217(6):753–764, 2003.

[46] Ibiye Aseibichin Roberts, CJ Wang, R Esterlein, M Stanford, and DJ Mynors. A three-dimensional finite element analysis of the temperature field during laser melting of metal powders in additive layer manufacturing. *International Journal of Machine Tools and Manufacture*, 49(12-13):916–923, 2009.

[47] Shiwen Liu, Haihong Zhu, Gangyong Peng, Jie Yin, and Xiaoyan Zeng. Microstructure

prediction of selective laser melting alsi10mg using finite element analysis. *Materials & Design*, 142:319–328, 2018.

[48] RS Mishra, TR Bieler, and AK Mukherjee. Superplasticity in powder metallurgy aluminum alloys and composites. *Acta metallurgica et materialia*, 43(3):877–891, 1995.

[49] G Dirras, J Gubicza, D Tingaud, and S Billard. Microstructure of al–al2o3 nanocomposite formed by in situ phase transformation during al nanopowder consolidation. *Materials Chemistry and Physics*, 129(3):846–852, 2011.

[50] M Tavoosi, MH Enayati, and F Karimzadeh. Softening behaviour of nanostructured al–14 wt% zn alloy during mechanical alloying. *Journal of alloys and compounds*, 464(1-2):107–110, 2008.

[51] MR Barnett, Zohreh Keshavarz, AG Beer, and Dale Atwell. Influence of grain size on the compressive deformation of wrought mg–3al–1zn. *Acta materialia*, 52(17):5093–5103, 2004.

[52] E Mora, Gerardo Garcés, Elvira Oñorbe, P Pérez, and Paloma Adeva. High-strength mg–zn–y alloys produced by powder metallurgy. *Scripta Materialia*, 60(9):776–779, 2009.

[53] EO Hall. The deformation and ageing of mild steel: Iii discussion of results. *Proceedings of the Physical Society. Section B*, 64(9):747, 1951.

[54] NJ Petch. The cleavage strength of polycrystals. *Journal of the Iron and Steel Institute*, 174: 25–28, 1953.

[55] Chang-Soo Kim, Il Sohn, Marjan Nezafati, JB Ferguson, Benjamin F Schultz, Zahra Bajestani-Gohari, Pradeep K Rohatgi, and Kyu Cho. Prediction models for the yield strength of particle-reinforced unimodal pure magnesium (mg) metal matrix nanocomposites (mmncs). *Journal of Materials Science*, 48(12):4191–4204, 2013.

[56] CS Zener. Grains, phases and interfaces: an interpretation of microstructure. *Trans. AIME*, 175:15–51, 1948.

[57] T Gladman. On the theory of the effect of precipitate particles on grain growth in metals.

Proceedings of the Royal Society of London. Series A, Mathematical and Physical Sciences, pages 298–309, 1966.

[58] MF Ashby, J Harper, and J Lewis. The interaction of crystal boundaries with second-phase particles. *Trans Met Soc AIME*, 245(2):413–420, 1969.

[59] RL Fullman. Metal interfaces. *American Society for Metals, Metals Park, OH*, 1952.

[60] O Hunder and N Ryum. The interaction between spherical particles and triple lines and quadruple points. *Acta metallurgica et materialia*, 40(3):543–549, 1992.

[61] N Ryum, O Hunderi, and E Nes. On grain boundary drag from second phase particles. *Scripta metallurgica*, 17(11):1281–1283, 1983.

[62] AH Chokshi, A Rosen, J Karch, and H Gleiter. On the validity of the hall-petch relationship in nanocrystalline materials. *Scripta Metallurgica*, 23(10):1679–1683, 1989.

[63] RL Coble. A model for boundary diffusion controlled creep in polycrystalline materials. *Journal of applied physics*, 34(6):1679–1682, 1963.

[64] TG Nieh and J Wadsworth. Hall-petch relation in nanocrystalline solids. *Scripta Metallurgica et Materialia*, 25(4):955–958, 1991.

[65] RA Masumura, PM Hazzledine, and CS Pande. Yield stress of fine grained materials. *Acta Materialia*, 46(13):4527–4534, 1998.

[66] Hans Conrad and Jagdish Narayan. On the grain size softening in nanocrystalline materials. *Scripta materialia*, 11(42):1025–1030, 2000.

[67] GJ Fan, H Choo, and PK Liaw. Embrittlement in a bulk nanocrystalline alloy induced by room-temperature aging. *Applied physics letters*, 89(6):061919, 2006.

[68] Farghalli A Mohamed and Manish Chauhan. Interpretation of the creep behavior of nanocrystalline ni in terms of dislocation accommodated boundary sliding. *Metallurgical and materials transactions A*, 37(12):3555–3567, 2006.

[69] Farghalli A Mohamed. Interpretation of nanoscale softening in terms of dislocation-accommodated boundary sliding. *Metallurgical and materials transactions A*, 38(2):340–347, 2007.

[70] Farghalli A Mohamed and Terence G Langdon. Deformation mechanism maps based on grain size. *Metallurgical transactions*, 5(11):2339–2345, 1974.

[71] Z Szaraz, Z Trojanova, M Cabbibo, and E Evangelista. Strengthening in a we54 magnesium alloy containing sic particles. *Materials Science and Engineering: A*, 462(1-2):225–229, 2007.

[72] M Habibnejad-Korayem, R Mahmudi, and WJ Poole. Enhanced properties of mg-based nano-composites reinforced with al2o3 nano-particles. *Materials Science and Engineering: A*, 519 (1-2):198–203, 2009.

[73] Zhenya Zhang, Huashun Yu, Shaoqing Wang, Haitao Wang, and Guanghui Min. Microstructure and tensile properties of zk60 alloy fabricated by simplified rapid solidification powder metallurgy (s-rs p/m) process. *Journal of Materials Science & Technology*, 26(2):151–155, 2010.

[74] QB Nguyen and M Gupta. Enhancing compressive response of az31b magnesium alloy using alumina nanoparticulates. *Composites Science and Technology*, 68(10-11):2185–2192, 2008.

[75] WS Miller and FJ Humphreys. Strengthening mechanisms in particulate metal matrix composites. *Scripta metallurgica et materialia*, 25(1):33–38, 1991.

[76] E Ma. Eight routes to improve the tensile ductility of bulk nanostructured metals and alloys. *Jom*, 58(4):49–53, 2006.

[77] E Ma. Instabilities and ductility of nanocrystalline and ultrafine-grained metals. *Scripta Materialia*, 49(7):663–668, 2003.

[78] QL Dai, BB Sun, ML Sui, G He, Y Li, J Eckert, WK Luo, and E Ma. High-performance bulk ti-cu-ni-sn-ta nanocomposites based on a dendrite-eutectic microstructure. *Journal of materials research*, 19(9):2557–2566, 2004.

[79] BB Sun, ML Sui, YM Wang, G He, J Eckert, and E Ma. Ultrafine composite microstructure in a bulk ti alloy for high strength, strain hardening and tensile ductility. *Acta materialia*, 54(5):1349–1357, 2006.

[80] E Ma, YM Wang, QH Lu, ML Sui, L Lu, and K Lu. Strain hardening and large tensile elongation in ultrahigh-strength nano-twinned copper. *Applied physics letters*, 85(21):4932–4934, 2004.

[81] CC Koch. Optimization of strength and ductility in nanocrystalline and ultrafine grained metals. *Scripta Materialia*, 49(7):657–662, 2003.

[82] Q Wei, T Jiao, KT Ramesh, and E Ma. Nano-structured vanadium: processing and mechanical properties under quasi-static and dynamic compression. *Scripta materialia*, 50(3): 359–364, 2004.

[83] Q Wei, D Jia, KT Ramesh, and E Ma. Evolution and microstructure of shear bands in nanostructured fe. *Applied physics letters*, 81(7):1240–1242, 2002.

[84] Khaled M Youssef, Ronald O Scattergood, K Linga Murty, and Carl C Koch. Ultratough nanocrystalline copper with a narrow grain size distribution. *Applied physics letters*, 85(6): 929–931, 2004.

[85] Bahman Homayun and Abdollah Afshar. Microstructure, mechanical properties, corrosion behavior and cytotoxicity of mg–zn–al–ca alloys as biodegradable materials. *Journal of Alloys and Compounds*, 607:1–10, 2014.

[86] Guang-Ling Song, Raja Mishra, and ZhenQing Xu. Crystallographic orientation and electrochemical activity of az31 mg alloy. *Electrochemistry Communications*, 12(8):1009–1012, 2010.

[87] Renlong Xin, Yuanming Luo, Ailing Zuo, Jiacheng Gao, and Qing Liu. Texture effect on corrosion behavior of az31 mg alloy in simulated physiological environment. *Materials letters*, 72:1–4, 2012.

[88] Jan-Marten Seitz, Kelly Collier, Eric Wulf, Dirk Bormann, and Friedrich-Wilhelm Bach. Comparison of the corrosion behavior of coated and uncoated magnesium alloys in an in vitro corrosion environment. *Advanced Engineering Materials*, 13(9):B313–B323, 2011.

[89] Yu Sun, Baoping Zhang, Yin Wang, Lin Geng, and Xiaohui Jiao. Preparation and characterization of a new biomedical mg–zn–ca alloy. *Materials & Design*, 34:58–64, 2012.

[90] S González, Eva Pellicer, Jordina Fornell, Andreu Blanquer, Lleonard Barrios, Elena Ibáñez, P Solsona, Santiago Suriñach, MD Baró, Carme Nogués, et al. Improved mechanical performance and delayed corrosion phenomena in biodegradable mg–zn–ca alloys through pd-alloying. *Journal of the mechanical behavior of biomedical materials*, 6:53–62, 2012.

[91] R Walter and M Bobby Kannan. In-vitro degradation behaviour of we54 magnesium alloy in simulated body fluid. *Materials Letters*, 65(4):748–750, 2011.

[92] Frank Witte, Norbert Hort, Carla Vogt, Smadar Cohen, Karl Ulrich Kainer, Regine Willumeit, and Frank Feyerabend. Degradable biomaterials based on magnesium corrosion. *Current opinion in solid state and materials science*, 12(5-6):63–72, 2008.

[93] Frank Witte, V Kaese, H Haferkamp, E Switzer, A Meyer-Lindenberg, CJ Wirth, and H Windhagen. In vivo corrosion of four magnesium alloys and the associated bone response. *Biomaterials*, 26(17):3557–3563, 2005.

[94] Ming Liu, Peter J Uggowitzer, AV Nagasekhar, Patrik Schmutz, Mark Easton, Guang-Ling Song, and Andrej Atrens. Calculated phase diagrams and the corrosion of die-cast mg–al alloys. *Corrosion Science*, 51(3):602–619, 2009.

[95] Guan Ling Song and Andrej Atrens. Corrosion mechanisms of magnesium alloys. *Advanced engineering materials*, 1(1):11–33, 1999.

[96] Michael M Avedesian, Hugh Baker, et al. *ASM specialty handbook: magnesium and magnesium alloys*. ASM international, 1999.

[97] Keon Ha Kim, Nguyen Dang Nam, Jung Gu Kim, Kwang Seon Shin, and Hwa Chul Jung. Effect of calcium addition on the corrosion behavior of mg–5al alloy. *Intermetallics*, 19(12): 1831–1838, 2011.

[98] Y-Q Wang, M-Z Li, C Li, X-Y Li, L-Q Fan, and T Jia. The effect of ca on corrosion behavior of heat-treated mg–al–zn alloy. *Materials and Corrosion*, 63(6):497–504, 2012.

[99] Erlin Zhang, Dongsong Yin, Liping Xu, Lei Yang, and Ke Yang. Microstructure, mechanical and corrosion properties and biocompatibility of mg–zn–mn alloys for biomedical application. *Materials Science and Engineering: C*, 29(3):987–993, 2009.

[100] Ming Liu, Patrik Schmutz, Peter J Uggowitzer, Guangling Song, and Andrej Atrens. The influence of yttrium (y) on the corrosion of mg–y binary alloys. *Corrosion Science*, 52(11): 3687–3701, 2010.

[101] Guangling Song. Control of biodegradation of biocompatable magnesium alloys. *Corrosion science*, 49(4):1696–1701, 2007.

[102] Seong Jong Kim, Seok Ki Jang, and Jeong Il Kim. Effects of the duration of potentiostatic anodizing on the corrosion resistance and surface morphology of films formed on mg-al alloys. In *Materials Science Forum*, volume 486, pages 125–128. Trans Tech Publ, 2005.

[103] C Blawert, D Manova, M Störmer, JW Gerlach, W Dietzel, and S Mändl. Correlation between texture and corrosion properties of magnesium coatings produced by pvd. *Surface and Coatings Technology*, 202(11):2236–2240, 2008.

[104] Andrej Atrens, Ming Liu, and Nor Ishida Zainal Abidin. Corrosion mechanism applicable to biodegradable magnesium implants. *Materials Science and Engineering: B*, 176(20):1609–1636, 2011.

[105] Ming-Chun Zhao, Ming Liu, Guangling Song, and Andrej Atrens. Influence of the β-phase morphology on the corrosion of the mg alloy az91. *Corrosion Science*, 50(7):1939–1953, 2008.

[106] Guangling Song and Andrej Atrens. Understanding magnesium corrosion?a framework for improved alloy performance. *Advanced engineering materials*, 5(12):837–858, 2003.

[107] LJ Liu and M Schlesinger. Corrosion of magnesium and its alloys. *Corrosion Science*, 51(8): 1733–1737, 2009.

[108] Sebastian Schnur and Axel Groß. Properties of metal–water interfaces studied from first principles. *New Journal of Physics*, 11(12):125003, 2009.

[109] Javier Carrasco, Andrew Hodgson, and Angelos Michaelides. A molecular perspective of water at metal interfaces. *Nature materials*, 11(8):667, 2012.

[110] Ji Chen, Georg Schusteritsch, Chris J Pickard, Christoph G Salzmann, and Angelos Michaelides. Two dimensional ice from first principles: Structures and phase transitions. *Physical review letters*, 116(2):025501, 2016.

[111] Federico Calle-Vallejo, José I Martínez, Juan M García-Lastra, Philippe Sautet, and David Loffreda. Fast prediction of adsorption properties for platinum nanocatalysts with generalized coordination numbers. *Angewandte Chemie International Edition*, 53(32):8316–8319, 2014.

[112] Rengin Pekz, Svenja Wrner, Luca M Ghiringhelli, and Davide Donadio. Trends in the adsorption and dissociation of water clusters on flat and stepped metallic surfaces. *The Journal of Physical Chemistry C*, 118(51):29990–29998, 2014.

[113] Peter Strasser, Shirlaine Koh, and Jeff Greeley. Voltammetric surface dealloying of pt bimetallic nanoparticles: an experimental and dft computational analysis. *Physical Chemistry Chemical Physics*, 10(25):3670–3683, 2008.

[114] Oleg I Velikokhatnyi and Prashant N Kumta. First-principles studies on alloying and simplified thermodynamic aqueous chemical stability of calcium-, zinc-, aluminum-, yttrium-and iron-doped magnesium alloys. *Acta Biomaterialia*, 6(5):1698–1704, 2010.

[115] Ming Liu, Dong Qiu, Ming-Chun Zhao, Guangling Song, and Andrej Atrens. The effect of crystallographic orientation on the active corrosion of pure magnesium. *Scripta Materialia*, 58(5):421–424, 2008.

[116] Levente Vitos, AV Ruban, Hans Lomholt Skriver, and J Kollar. The surface energy of metals. *Surface science*, 411(1-2):186–202, 1998.

[117] Ulf von Barth. Basic density-functional theory?an overview. *Physica Scripta*, 2004(T109):9, 2004.

[118] Erwin Schrödinger. An undulatory theory of the mechanics of atoms and molecules. *Physical review*, 28(6):1049, 1926.

[119] SM Blinder. Basic concepts of self-consistent-field theory. *American Journal of Physics*, 33 (6):431–443, 1965.

[120] Walter Kohn and Lu Jeu Sham. Self-consistent equations including exchange and correlation effects. *Physical review*, 140(4A):A1133, 1965.

[121] John P Perdew and Wang Yue. Accurate and simple density functional for the electronic exchange energy: Generalized gradient approximation. *Physical review B*, 33(12):8800, 1986.

[122] David M Ceperley and BJ Alder. Ground state of the electron gas by a stochastic method. *Physical Review Letters*, 45(7):566, 1980.

[123] John P Perdew, JA Chevary, SH Vosko, Koblar A Jackson, Mark R Pederson, DJ Singh, and Carlos Fiolhais. Erratum: Atoms, molecules, solids, and surfaces: Applications of the generalized gradient approximation for exchange and correlation. *Physical Review B*, 48(7): 4978, 1993.

[124] Robert G Parr and Weitao Yang. Density-functional theory of atoms and molecules, vol. 16 of international series of monographs on chemistry, 1989.

[125] Manuel J Kolb, Jasper Wermink, Federico Calle-Vallejo, Ludo BF Juurlink, and Marc TM Koper. Initial stages of water solvation of stepped platinum surfaces. *Physical Chemistry Chemical Physics*, 18(5):3416–3422, 2016.

[126] Patricia A Thiel and Theodore E Madey. The interaction of water with solid surfaces: fundamental aspects. *Surface Science Reports*, 7(6-8):211–385, 1987.

[127] Marjan Nezafati, Il Sohn, JB Ferguson, Joon-Sang Park, Kyu Cho, and Chang-Soo Kim. Dft study on the adsorption and absorption behaviors of liquid nitrogen in the mg nano alloys synthesized from powder metallurgy. *Computational Materials Science*, 105:18–26, 2015.

[128] Bao-Qin Fu, Wei Liu, and Zhi-Lin Li. Calculation of the surface energy of hcp-metals with the empirical electron theory. *Applied Surface Science*, 255(23):9348–9357, 2009.

[129] U König and B Davepon. Microstructure of polycrystalline ti and its microelectrochemical properties by means of electron-backscattering diffraction (ebsd). *Electrochimica Acta*, 47 (1-2):149–160, 2001.

[130] RICHARD F ASHTON and MALCOLM T HEPWORTH. Effect of crystal orientation on the anodic polarization and passivity of zinc. *Corrosion*, 24(2):50–53, 1968.

[131] Jiancai Liu, Xinming Zhang, Mingan Chen, Li Li, Bing Zhu, Jianguo Tang, and Shengdan Liu. Dft study on surface properties and dissolution trends of al (1 0 0) surfaces doped with zn, ga, in, sn and pb. *Applied Surface Science*, 257(9):4004–4009, 2011.

[132] Bernard Delley. An all-electron numerical method for solving the local density functional for polyatomic molecules. *The Journal of chemical physics*, 92(1):508–517, 1990.

[133] Bernard Delley. From molecules to solids with the dmol 3 approach. *The Journal of chemical physics*, 113(18):7756–7764, 2000.

[134] C Stampfl, W Mannstadt, R Asahi, and AJ Freeman. Electronic structure and physical properties of early transition metal mononitrides: Density-functional theory lda, gga, and screened-exchange lda flapw calculations. *Physical Review B*, 63(15):155106, 2001.

[135] Agostino Zoroddu, Fabio Bernardini, Paolo Ruggerone, and Vincenzo Fiorentini. First-principles prediction of structure, energetics, formation enthalpy, elastic constants, polarization, and piezoelectric constants of aln, gan, and inn: Comparison of local and gradient-corrected density-functional theory. *Physical Review B*, 64(4):045208, 2001.

[136] Chunyang Peng and H Bernhard Schlegel. Combining synchronous transit and quasi-newton methods to find transition states. *Israel Journal of Chemistry*, 33(4):449–454, 1993.

[137] Thomas A Halgren and William N Lipscomb. The synchronous-transit method for determining reaction pathways and locating molecular transition states. *Chemical Physics Letters*, 49 (2):225–232, 1977.

[138] David Yarkony. *Modern electronic structure theory*, volume 2. World Scientific, 1995.

[139] Graeme Henkelman and Hannes Jónsson. Improved tangent estimate in the nudged elastic band method for finding minimum energy paths and saddle points. *The Journal of chemical physics*, 113(22):9978–9985, 2000.

[140] Jian Hao, Yinwei Li, Qiang Zhou, Dan Liu, Min Li, Fangfei Li, Weiwei Lei, Xiaohui Chen, Yanming Ma, Qiliang Cui, et al. Structural phase transformations of mg3n2 at high pressure: experimental and theoretical studies. *Inorganic chemistry*, 48(20):9737–9741, 2009.

[141] Eleftherios Louvis, Peter Fox, and Christopher J Sutcliffe. Selective laser melting of aluminium components. *Journal of Materials Processing Technology*, 211(2):275–284, 2011.

[142] Ming Tang, P Chris Pistorius, Sneha Narra, and Jack L Beuth. Rapid solidification: selective laser melting of alsi10mg. *JOM*, 68(3):960–966, 2016.

[143] PK Rohatgi, K Pasciak, CS Narendranath, S Ray, and A Sachdev. Evolution of microstructure and local thermal conditions during directional solidification of a356-sic particle composites. *Journal of materials science*, 29(20):5357–5366, 1994.

[144] Yali Li and Dongdong Gu. Parametric analysis of thermal behavior during selective laser melting additive manufacturing of aluminum alloy powder. *Materials & Design*, 63:856–867, 2014.

[145] EA Brandes. Smithells metals reference book, 1983. *London, Butter worth*, 2000.

[146] Jie Yin, Haihong Zhu, Linda Ke, Wenjuan Lei, Cheng Dai, and Duluo Zuo. Simulation of temperature distribution in single metallic powder layer for laser micro-sintering. *Computational Materials Science*, 53(1):333–339, 2012.

[147] Genichi Taguchi. Introduction to quality engineering, asian productivity organization, tokyo, 1990. *Google Scholar*, 2006.

[148] Glen Stuart Peace and Glen Stuart Peace. *Taguchi methods: a hands-on approach*. Addison-Wesley Reading, MA, 1993.

[149] L Lu, KK Thong, and M Gupta. Mg-based composite reinforced by mg2si. *Composites Science and Technology*, 63(5):627–632, 2003.

[150] Tatsuhiko Aizawa, Hideyuki Kuwahara, and Luangvaranunt Tachai. Surface modification of magnesium base alloys by gas/plasma nitridation. In *Materials science forum*, volume 350, pages 247–252. Trans Tech Publ, 2000.

[151] C Hofmeister, B Yao, YH Sohn, T Delahanty, M Van den Bergh, and K Cho. Composition and structure of nitrogen-containing dispersoids in trimodal aluminum metal–matrix composites. *Journal of materials science*, 45(17):4871–4876, 2010.

[152] Clara Hofmeister, Mikhail Klimov, Tim Deleghanty, Kyu Cho, and Yongho Sohn. Quantification of nitrogen impurity and estimated orowan strengthening through secondary ion mass spectroscopy in aluminum cryomilled for extended durations. *Materials Science and Engineering: A*, 648:412–417, 2015.

[153] Yuan Chunmiao, Yu Lifu, Li Chang, Li Gang, and Zhong Shengjun. Thermal analysis of magnesium reactions with nitrogen/oxygen gas mixtures. *Journal of hazardous materials*, 260:707–714, 2013.

[154] John Aurie Dean. *Lange's handbook of chemistry*. New york; London: McGraw-Hill, Inc., 1999.

[155] Marta Pozuelo, Christopher Melnyk, Wei H Kao, and Jenn-Ming Yang. Cryomilling and spark plasma sintering of nanocrystalline magnesium-based alloy. *Journal of Materials Research*, 26(7):904–911, 2011.

[156] M Pozuelo, YW Chang, and J-M Yang. Enhanced compressive strength of an extruded nanostructured mg–10al alloy. *Materials Science and Engineering: A*, 594:203–211, 2014.

[157] M Pozuelo, YW Chang, and JM Yang. Effect of diamondoids on the microstructure and mechanical behavior of nanostructured mg-matrix nanocomposites. *Materials Science and Engineering: A*, 633:200–208, 2015.

[158] VL Tellkamp, EJ Lavernia, and A Melmed. Mechanical behavior and microstructure of a thermally stable bulk nanostructured al alloy. *Metallurgical and Materials Transactions A*, 32(9):2335–2343, 2001.

[159] B deB Darwent. Bond dissociation energies in simple molecules. *NSRDS-NBS 31*, 1970.

[160] Kaka Ma, Enrique J Lavernia, and Julie M Schoenung. Absorption of nitrogen at al/al2o3 interfaces in al nanocomposites: a computational analysis. *Advanced Engineering Materials*, 14(1-2):77–84, 2012.

[161] MJ Gillan. Calculation of the vacancy formation energy in aluminium. *Journal of Physics: Condensed Matter*, 1(4):689, 1989.

[162] A Vehanen and K Rytsölä. Proceedings of the international school of physics, 1981.

[163] Chen Huang and Emily A Carter. Transferable local pseudopotentials for magnesium, aluminum and silicon. *Physical Chemistry Chemical Physics*, 10(47):7109–7120, 2008.

[164] J Chatt. Molecular nitrogen as a ligand. *Pure and Applied Chemistry*, 24(2):425–442, 1970.

[165] Frank H Allen, Olga Kennard, David G Watson, Lee Brammer, A Guy Orpen, and Robin Taylor. Tables of bond lengths determined by x-ray and neutron diffraction. part 1. bond lengths in organic compounds. *Journal of the Chemical Society, Perkin Transactions 2*, (12): S1–S19, 1987.

[166] Bo Yao, Clara Hofmeister, Travis Patterson, Yong-ho Sohn, Mark van den Bergh, Tim Delahanty, and Kyu Cho. Microstructural features influencing the strength of trimodal aluminum metal-matrix-composites. *Composites Part A: Applied Science and Manufacturing*, 41(8): 933–941, 2010.

[167] Björn Lange, Christoph Freysoldt, and Jörg Neugebauer. Native and hydrogen-containing point defects in mg 3 n 2: A density functional theory study. *Physical Review B*, 81(22): 224109, 2010.

[168] Frederick Dominic Rossini and Frederick Dominic Rossini. *Selected values of chemical thermodynamic properties*, volume 500. US Government Printing Office Washington, DC, 1952.

[169] B.(Author) Predel and O Madelung. *Landolt-Bornstein, Group IV Physical Chemistry-Phase Equilibria, Crystallographic and Thermodynamic Data of Binary Alloys, Volume 5-Electronic Materials and Semiconductors*. Springer-Verlag, 1991.

[170] W Klemm and G Winkelmann. Zur kenntnis der nitride der seltenen erdmetalle. *Zeitschrift für anorganische und allgemeine Chemie*, 288(1-2):87–90, 1956.

[171] Jichun Ye, Bing Q Han, Zonghoon Lee, Byungmin Ahn, Steve R Nutt, and Julie M Schoenung. A tri-modal aluminum based composite with super-high strength. *Scripta Materialia*, 53(5): 481–486, 2005.

[172] Jatinkumar Kumar Rana, D Sivaprahasam, K Seetharama Raju, and V Subramanya Sarma. Microstructure and mechanical properties of nanocrystalline high strength al–mg–si (aa6061) alloy by high energy ball milling and spark plasma sintering. *Materials Science and Engineering: A*, 527(1-2):292–296, 2009.

[173] Indranil Roy, Manish Chauhan, Farghalli A Mohamed, and Enrique J Lavernia. Thermal stability in bulk cryomilled ultrafine-grained 5083 al alloy. *Metallurgical and Materials Transactions A*, 37(3):721–730, 2006.

[174] Y Li, W Liu, V Ortalan, WF Li, Z Zhang, R Vogt, ND Browning, EJ Lavernia, and JM Schoenung. Hrtem and eels study of aluminum nitride in nanostructured al 5083/b4c processed via cryomilling. *Acta Materialia*, 58(5):1732–1740, 2010.

[175] RF Singer, WC Oliver, and WD Nix. Identification of dispersoid phases created in aluminum during mechanical alloying. *Metallurgical Transactions A*, 11(11):1895–1901, 1980.

[176] Feng Tang, Masuo Hagiwara, and Julie M Schoenung. Microstructure and tensile properties of bulk nanostructured al-5083/sicp composites prepared by cryomilling. *Materials Science and Engineering: A*, 407(1-2):306–314, 2005.

[177] EJ Lavernia, BQ Han, and JM Schoenung. Cryomilled nanostructured materials: Processing and properties. *Materials Science and Engineering: A*, 493(1-2):207–214, 2008.

[178] BQ Han, JY Huang, YT Zhu, and EJ Lavernia. Strain rate dependence of properties of cryomilled bimodal 5083 al alloys. *Acta materialia*, 54(11):3015–3024, 2006.

[179] JM Shoenung, J Ye, J He, F Tang, and D Witkin. B4c reinforced nanocrystalline aluminum composites: Synthesis, characterization, and cost analysis. In *Materials Forum*, volume 29, pages 123–128, 2005.

[180] Young S Park, Kyung H Chung, Nack J Kim, and Enrique J Lavernia. Microstructural investigation of nanocrystalline bulk al–mg alloy fabricated by cryomilling and extrusion. *Materials Science and Engineering: A*, 374(1-2):211–216, 2004.

[181] MH Stans. Bond dissociation energies in simple molecules, nist. In *Library of Congress*, 1970.

[182] Manos Mavrikakis, Jane Rempel, J Greeley, Lars Bruno Hansen, and Jens Kehlet Nørskov. Atomic and molecular adsorption on rh (111). *The Journal of chemical physics*, 117(14): 6737–6744, 2002.

[183] Jeffrey A Herron, Scott Tonelli, and Manos Mavrikakis. Atomic and molecular adsorption on pd (111). *Surface Science*, 606(21-22):1670–1679, 2012.

[184] Anders Hellman, Behrooz Razaznejad, and Bengt I Lundqvist. Trends in sticking and adsorption of diatomic molecules on the al (111) surface. *Physical Review B*, 71(20):205424, 2005.

[185] K Jacobi, C Astaldi, P Geng, and M Bertolo. Physisorption of n2 and co on al (111): a combined hreels-ups investigation. *Surface Science*, 223(3):569–577, 1989.

[186] Jerry A Boatz and Dan Sorescu. Polynitrogen/nanoaluminum surface interactions. In *DoD HPCMP Users Group Conference, 2008. DOD HPCMP UGC*, pages 247–251. IEEE, 2008.

[187] Bjørk Hammer and Jens Kehlet Nørskov. Theoretical surface science and catalysis?calculations and concepts. In *Advances in catalysis*, volume 45, pages 71–129. Elsevier, 2000.

[188] Anders Nilsson, Lars GM Pettersson, and Jens Norskov. *Chemical bonding at surfaces and interfaces*. Elsevier, 2011.

[189] Marjan Nezafati, Kyu Cho, Anit Giri, and Chang-Soo Kim. Dft study on the water molecule adsorption and the surface dissolution behavior of mg alloys. *Materials Chemistry and Physics*, 182:347–358, 2016.

[190] GE Laramore, CB Duke, A Bagchi, and AB Kunz. Low-energy-electron diffraction from al (100), al (110), al (111), and cu (100). *Physical Review B*, 4(6):2058, 1971.

[191] DW Jepsen, PM Marcus, and F Jona. Low-energy-electron diffraction from several surfaces of aluminum. *Physical Review B*, 6(10):3684, 1972.

[192] MR Martin and GA Somorjai. Determination of the surface geometry for the aluminum (110) and (111) surfaces by comparison of low-energy-electron-diffraction calculations with experiment. *Physical Review B*, 7(8):3607, 1973.

[193] Roman Smoluchowski. Anisotropy of the electronic work function of metals. *Physical Review*, 60(9):661, 1941.

[194] MD Starostenkov and R Yu Rakitin. Atomic configurations and diffusion mechanisms near the asymmetric grain boundaries in tetragonal cuau i alloy with¡ 100¿ and¡ 001¿ tilt axes. *Russian Physics Journal*, 54(9):994–1005, 2012.

[195] Alan F Wright, Peter J Feibelman, and Susan R Atlas. First-principles calculation of the mg (0001) surface relaxation. *Surface science*, 302(1-2):215–222, 1994.

[196] Frank R De Boer, WCM Mattens, R Boom, AR Miedema, and AK Niessen. Cohesion in metals. 1988.

[197] A Michaelides, VA Ranea, PL De Andres, and DA King. General model for water monomer adsorption on close-packed transition and noble metal surfaces. *Physical review letters*, 90 (21):216102, 2003.

[198] Allen J Bard, Larry R Faulkner, Johna Leddy, and Cynthia G Zoski. *Electrochemical methods: fundamentals and applications*, volume 2. wiley New York, 1980.

[199] J Greeley and Jens Kehlet Nørskov. Electrochemical dissolution of surface alloys in acids: Thermodynamic trends from first-principles calculations. *Electrochimica Acta*, 52(19):5829–5836, 2007.

[200] Yuguang Ma and Perla B Balbuena. Surface properties and dissolution trends of pt3m alloys in the presence of adsorbates. *The Journal of Physical Chemistry C*, 112(37):14520–14528, 2008.

[201] F Gao, DJ Bacon, and GJ Ackland. Point-defect and threshold displacement energies in ni3al i. point-defect properties. *Philosophical Magazine A*, 67(2):275–288, 1993.

[202] O Madelung, U Rössler, and M Schulz. Landolt and bornstein-group iii condensed matter: Group iv elements,(iv-iv) and (iii-v) compounds. part b-electronic, transport, optical and other properties, 2006.

[203] Donald Robert Uhlmann, B Chalmers, and KA Jackson. Interaction between particles and a solid-liquid interface. *Journal of Applied Physics*, 35(10):2986–2993, 1964.

[204] AA Chernov, DE Temkin, and AM Mel?Nikova. Theory of the capture of solid inclusions during the growth of crystals from the melt. *Sov. Phys. Crystallogr*, 21(4):369–373, 1976.

[205] D Shangguan, S Ahuja, and DM Stefanescu. An analytical model for the interaction between an insoluble particle and an advancing solid/liquid interface. *Metallurgical Transactions A*, 23(2):669–680, 1992.

[206] Doru M Stefanescu, Frank R Juretzko, A Catalina, BK Dhindaw, Subhayu Sen, and Peter A Curreri. Particle engulfment and pushing by solidifying interfaces: Part ii. microgravity experiments and theoretical analysis. *Metallurgical and Materials Transactions A*, 29(6): 1697–1706, 1998.

[207] JK Kim and PK Rohatgi. An analytical solution of the critical interface velocity for the encapturing of insoluble particles by a moving solid/liquid interface. *Metallurgical and Materials Transactions A*, 29(1):351–358, 1998.

[208] G Kaptay. Interfacial criterion of spontaneous and forced engulfment of reinforcing particles by an advancing solid/liquid interface. *Metallurgical and Materials Transactions A*, 32(4): 993–1005, 2001.

[209] Xie-Min Mao and Hong-Quan Wen. Study on particle pushing in front of growing interface during soldification. *Journal of Shanghai University (English Edition)*, 6(3):233–235, 2002.

[210] Yutao Tao, Andrew Yeckel, and Jeffrey J Derby. Steady-state and dynamic models for particle engulfment during solidification. *Journal of Computational Physics*, 315:238–263, 2016.

[211] D Shangguan, S Ahuja, and DM Stefanescu. An analytical model for the interaction between an insoluble particle and an advancing solid/liquid interface. *Metallurgical Transactions A*, 23(2):669–680, 1992.

MARJAN NEZAFATI

Nezafati@uwm.edu

EDUCATION

University of Wisconsin-Milwaukee, Milwaukee, Wisconsin
PhD: Materials Science and Engineering, (September 2013-Present)
Thesis: *In silico analysis of advanced processing methods for lightweight alloys powders*
CEAS Dean's Scholarship, Spring 2014

University of Wisconsin-Milwaukee, Milwaukee, Wisconsin
MS: Materials Science and Engineering, August 2013
Thesis: *Density Functional Theory (DFT) Studies on the Hydrolysis Behavior of Degradable Mg/Mg Alloys for Biomedical Applications*
Chancellor's Graduate Student Award for 4 consecutive semesters.

Iran University of Science and Technology, Tehran
BS: Material Science and Engineering, April 2011
Thesis: *Effect of Heat Treatment on Charpy Impact Energy of Cr-W-V Steel*
Awarded full academic scholarship

RESEARCH EXPERIENCE

Intern - Advanced Analysis Facility Lab - University of Wisconsin-Milwaukee, Wisconsin, June 2016-Present
- Building Efficiency Facility, Refrigeration Lab - Johnson Controls Inc., Wisconsin, April 2017
Research Assistant - University of Wisconsin-Milwaukee, Wisconsin, 2013-2017
Project Assistant - University of Wisconsin-Milwaukee, Milwaukee, Wisconsin, 2011-2013
Undergraduate Researcher - Iran University of Science and Technology, 2010-2011

Nano Materials and Composites

- Developed several atomistic models to describe the adsorption and absorption and diffusion behaviors of nitrogen in Al and Mg Nano alloys synthesized from powder metallurgy *(Materials Studio)*
- Completed courses: Composites and Powder Metallurgy

Electrochemistry

- Enhanced the performance of Na-ion batteries by proposing an atomistic model for the diffusion process in beta-alumina and Nasicon *(Materials Studio)*
- Simulated the corrosion process to determine the ideal composition of magnesium alloys for optimum corrosion rate in biodegradable implants *(Materials Studio)*
- Completed courses: Corrosion, Surface Engineering, Electronic Materials and Nondestructive Testing

Materials Characterization and Developments

- Provided failure analysis consultancy to manufacturing companies.
- Optimized and calibrated EDX and SEM for Advanced Analysis Facility Lab
- Prepared analytical instructions and provided assistance to BET users to analyze their results
- Completed courses: Advanced Materials Characterization, Heat Treatment of Metals, Transport Phenomena, Advanced Thermodynamics of Materials, Casting and Solidification

SOFTWARE PROFICIENCIES

Atomistic Modeling (Density Functional Theory/Molecular Dynamics): Materials Studio, LAMMPS, ABINIT
Finite Element Methods: ANSYS (fluent and APDL), COMSOL, ABAQUS
General Programing: MATLAB/Octave
Design of Experiments: Minitab

MATERIALS ANALYSIS SKILLS

Microscopy: SEM, AFM, and Confocal microscopy
Characterization: BET, EDS, XRD and FTIR

MARJAN NEZAFATI

TEACHING EXPERIENCE

Teaching Assistant - University of Wisconsin-Milwaukee, Milwaukee, Wisconsin, 2012-2013
Teaching Assistant and Lab Manager - University of Wisconsin-Milwaukee, Milwaukee, Wisconsin, 2017-Present

- Instructed materials testing and characterization, mechanical testing and microscopy including SEM and OM
- Received highest student course evaluations in the department

Volunteer Instructor - ASM Materials Camp, Milwaukee, Wisconsin, Summers 2012-2014

- Facilitated hands-on experiential learning opportunities for high school students

PUBLICATIONS

M Nezafati, K Cho, A Giri, C-S Kim, "DFT study on the adsorption, dissociation, and diffusion of liquid nitrogen in the Al alloys during cryomilling process", Journal of Alloys and Compounds (submitted)

C-S Kim, K Cho, M H Manjili, **M Nezafati**, "Mechanical Performance of Particulate-reinforced Al Metal-matrix Composites (MMCs) and Al Metal-Matrix Nanocomposites (MMNCs)", Journal of Materials Science, December 2017, Volume 52, pp. 13319-13349.

M Nezafati, K Cho, A Giri, CS Kim, "DFT study on the water molecule adsorption and the surface dissolution behavior of Mg alloys" Materials Chemistry and Physics, October 2016, Volume 182, pp 347-358.

H Park, K Jung, **M Nezafati**, CS Kim, B Kang, "Sodium ion diffusion in Nasicon (Na3Zr2Si2PO12) solid electrolytes: Effects of excess sodium" ACS Applied Materials & Interfaces, October 2016, Volume 8, Issue 41, pp 27814-27824.

M Nezafati, A Giri, C Hofmeister, K Cho, L Zhou, Y Sohn, C Kim, "Atomistic study on the interaction of nitrogen and Mg lattice and the nitride formation in nanocrystalline Mg alloys synthesized using cryomilling process" Acta Materialia, August 2016, Volume 115, pp 295-307.

M Nezafati, I Sohn, JB Ferguson, K Cho, CS Kim, "DFT study on the adsorption and absorption behaviors of liquid nitrogen in the magnesium nano alloys synthesized from powder metallurgy" Computational Materials Science, July 2015, Volume 105, pp 18-26.

CS Kim, I Sohn, **M Nezafati**, JB Ferguson, BF Schultz, Z Bajestani-Gohari, PK Rohatgi, K Cho, "Prediction models for the yield strength of particle-reinforced unimodal pure magnesium (Mg) metal matrix nanocomposites (MMNCs)" Journal of Material Science, June 2013, Volume 48, Issue 12, pp 4191-4204.

CONFERENCE PAPERS AND BOOK CHAPTERS

M Nezafati, A Bakhshinejad, P Rohatgi, B Church "Finite element analysis of particle pushing during selective laser melting of AlSi10Mg/AlN composites", 2019 TMS Annual Meeting & Exhibition, TX, San Antonio

A Bakhshinejad, **M Nezafati**, C-S Kim, R M D'Souza, "Molecular Dynamics Simulation of Friction in Self-Lubricating Materials; An Overview of theories and available models", Advances in Self-Lubricating composites, Springer,2018

MEMBERSHIPS & AFFILIATIONS

Materials Advantage, ASM - American Society of Materials, SWE - Society of Women Engineers, AFS – American Foundry Society

LANGUAGES

English (Professional working proficiency), French (Limited working proficiency), Persian (Native)